Carnegie Mellon University
MELLON COLLEGE OF SCIENCE

THESIS

SUBMITTED IN PARTIAL FULFILLMENT OF THE REQUIREMENTS
FOR THE DEGREE OF

DOCTOR OF PHILOSOPHY IN THE FIELD OF PHYSICS

TITLE: **"**A New Method for Fracture Surface Studies: Combined HEDM Orientation Mapping and Absorption Tomography Applied to a Nickel Superalloy."

PRESENTED BY: Xi Tan

ACCEPTED BY THE DEPARTMENT OF PHYSICS

Robert Suter	2/26/14
ROBERT SUTER, CHAIR PROFESSOR	DATE
Stephen Garoff	2/26/14
STEPHEN GAROFF, DEPT HEAD	DATE

APPROVED BY THE COLLEGE COUNCIL

Fred Gilman	2/26/14
FRED GILMAN, DEAN	DATE

A New Method for Fracture Surface Studies: Combined HEDM Orientation Mapping and Absorption Tomography Applied to a Nickel Superalloy

by

Xi Tan

Submitted in partial fulfillment of the
requirements for the degree of
Doctor of Philosophy
at
Carnegie Mellon University
Department of Physics
Pittsburgh, Pennsylvania

Advised by Professor Robert M. Suter and Professor Anthony D. Rollett

February 26, 2014

Abstract

Crystallographic directions normal to the fracture surface and orientation distributions are important statistics that give valuable insights into the phenomenon of crack initiation and propagation in metallic polycrystalline materials. In this thesis, we present a new method to extract crystallographic direction information at and around fracture surfaces. This method combines near field High Energy X-ray Diffraction Microscopy (HEDM) and high energy X-ray tomography. This new method gives much better accuracy than the current state-of-the-art techniques based on scanning electron microscopy because it is inherently three-dimensional.

In this thesis, not only the new method is presented, but it is also applied to the study of two halves of a sample of Rene88DT that was tested in fatigue to complete fracture. A pin suitable for HEDM was cut from each half so as to surround the initiation point. Volumetric data is collected at beamline 1-ID at the Advanced Photon Source (APS). A volumetric registration scheme is developed to align the data from the two pins so as to reconstruct the crystallography across the fracture. The fracture surface is characterized and the distribution of crystallographic directions normal to the fracture surface is studied in detail. Finally, the initiation site of the fracture is located and compared with a prediction from a simulation based on a viscoplastic deformation model, and qualitative agreement is found.

Acknowledgments

First, I would like to acknowledge my advisors, Professor Robert M. Suter and Professor Anthony D. Rollett for their patient mentoring, insightful discussion and continuous support throughout my research project. I am also grateful to my thesis committee members, Professor Stephen Garoff and Professor Randall Feenstra for their valuable insights and critical reviews.

I also would like to thank my past and current colleagues in Suter and Rollett groups, Dr. Shui Fai Li, Dr. Chris Hefferan, Dr. Jonathan Lind, Dr. Reeju Pokharel, Siddharth Maddali, David Menasche, Benjamin Anglin, Clayton Stein for their assistance and help to this thesis work. I also would like to thank Dr. Ulrich Lienert, Dr. Peter Kenesei, Dr. Sarvjit Shastri, Dr. Ali Mashayekhi, Dr. Brian Tieman and Dr. Jonathan Almer at the APS for their generous support at the beam line.

I would also like to extend my sincere gratitude to research scientists at GE™Global Research. This includes Dr. Yan Gao, Dr. Andrew Deal and Dr. Timothy Hanlon. Special thanks to Dr. Yan Gao for his excellent coordination and collaboration.

Last but not the least, I would like to express my deepest gratitude to my parents Lin Liu and Junjie Tan for their understanding, love and support, while I am on the other side of the earth for quite a long time.

Contents

List of Tables

List of Figures

Chapter 1

Introduction

1.1 Motivation

From the engineering perspective, the resistance to fracture and fatigue is one of the most important properties for materials, especially for those industrial materials working under extreme environments. For example, a jet's turbine blades are typically working under elevated temperature over $1000°C$ and enduring high stress levels. In such an environment, materials are susceptible to cracking which imposes potential danger to the safety of the flight. Thus for the purpose of upgrading current industrial materials or developing new materials, designers are constantly looking for substitutes with equivalent functionalities but better fracture resistance behaviors to elongate service life. Two groups of factors heavily influence the service life. One is the external environmental conditions, like gas atmosphere, temperature, stress loading pattern and stressing frequency, which are typically not adjustable, however, the other is the material's intrinsic fracture mechanism, depending on various factors like orientation distribution, grain boundary distribution, grain size distribution and secondary particle property, which can be typically controlled and manipulated by the designers. Thus, in order to develop a robust material with elongated service life, the understanding of the fracture mechanism is a prerequisite.

To understand the fracture mechanism, previous practices based on theoretical modelling and statistical inference on single crystal samples are known to be insufficient to uncover all the mysteries. Theories have been established by various authors[1, 2, 3, 4, 5, 6, 7, 8, 9] but validating experimental data is limited.

Recent advances in experimental technologies give birth to a set of new techniques to extract important microstructure statistics. Among all the important statistics, the crystallographic direction normal to the fracture surface[1], which is defined as the normal direction of the crystal lattice plane on the fracture surface, opens up a new horizon for the fracture mechanism study. Considerable efforts[5, 6, 7, 8, 9, 10, 11]

[1]Some literature refers this as crystallographic orientation, but we reserve this term for a voxel's orientation.

have been made to study the crystallographic directions normal to the fracture surface on different samples for characterizing fracture surfaces as well as understanding various aspects of the fracture mechanism. For example, Gangloff[12] studied the hydrogen assisted cracking of high strength alloys. Liu et al.[13] discovered that fracture facets produced by stress corrosion cracking are large and flat and the distribution is close to [100]. Park[14] reveals that the distributions of crystallographic normals strongly influences the tensile properties of the weld of Magnesium alloy AZ61. [15] studied the orientation dependent anisotropy in toughness which is primarily originated from crack bridging. Bowen[16] relates fracture toughness values for six test orientations in a strongly textured Ti-6A1-4V bar to their crystallographic directions normal to the fracture surface. Other areas include, though are not limited to, fatigue crack growth[17], crack initiation site[18, 19] and tensile testing[20].

1.2 Literature Review

With such a wide range of studies relying on knowledge of the crystallographic normals, accurate experimental measurements to extract such information from fracture surfaces is needed. In this section, we review literatures regarding current state-of-the-art techniques to extract the crystallographic directions normal to the fracture surface.

To obtain the crystallographic normals, two independent pieces of information are is typically required, as Randle et al. suggested in [21],

> "There are two primary and separate requirements for the experimental measurements of facet crystallography on the fracture surface of polycrystalline materials
>
> - the positional coordinate of a fracture facet in space
> - the crystallographic orientation of the facet"

To obtain the above knowledge, the current state-of-the-art techniques are mainly based on the combination of the electron backscatter diffraction (EBSD) and the photogrammetry both using the scanning electron microscope (SEM). It is well known that EBSD is surface technique that is designed to examine crystal orientations at surfaces of polycrystalline materials, thus in theory the orientation information of the fracture can be retrieved. For determination of the positional coordinate of the facets, typically an elegant method known as the photogrammetry is widely used[22, 23, 24]. Essentially, photogrammetry takes 2D high resolution photographs from different camera views and reconstructs accurate 3D volumetric information of the fracture surface from those 2D images[25].

These state-of-the-art techniques are generally referred to as the SEM-based technique, because they rely heavily on SEM. Depending on the way EBSD measurement

is performed, they can be further categorized into two sub-groups, one is known as the *direct approach* and the other is known as the *indirect approach*. These two variants differ from each other in terms of the measurement of orientations on the fracture surface. However, the invention of one was originally intended to overcome the drawbacks of the other but both face to challenges, as we describe in the following paragraphs.

Direct Approach

The direct approach performs normal EBSD measurements *directly* on top of the fracture surface. Though it sounds straightforward, it suffers from serious errors in terms of the determination of the orientation, as stated by[26]

> "The exact crystallographic orientation of each cleavage facet deviates within a finite azimuthal range from the sample normal direction, which was not restricted to 5° as in the case of the investigation by Field (1997)[27]"

The error bar, as large as 5° in one component of the Euler angle as mentioned above, is inherent with the way EBSD is performed in this approach, while comparing with the typical EBSD measurement, where the orientation information is indexed from the electron backscatter diffraction pattern (EBSP), the typical error is around 1°. The five-fold error increase in the direct approach comes from the experimental scheme developed by Field[27] based on the following observation. The direct measurement of EBSD at the optimal angle provides a good EBSP, with a apparent intensity gradient between the background image and the correct image. However, at 1°, 2° and 3° and 4° deviations of the SEM header from the optimal position, this intensity gradient deteriorates but is still observable but at a 5° difference, the gradient overwhelms any diffraction patterns, and this is where the 5° error bar comes from experimentally. The deterioration of EBSP at off-optimal angle probably results from uneven surfaces while a typical EBSD measurement requires a polished sample surface to work on while this direct approach does not have such luxury, otherwise it needs to destroy the sample. So with unknown topology of the fracture surface, it is quite possible that the EBSPs can be distorted within that 5° range.

Besides the 5° error bar approach, the direct problem also suffers another problem which requires intensive experimentation. As mentioned above, the SEM head must be placed at the optimal angle, typically around 70°, to create good EBSP features. However, considering the range of local normal orientations, it is not straightforward to do the correct placing quickly, which leads to a possible exhaustive search that is usually not doable. A typical workaround is proposed and implemented in Davies' paper[26], where an electron beam with a fixed angle is chosen and scans over the whole surface. Local regions not in the right angle are ignored while EBSPs in the right angle are recorded and analyzed. Using this approach, Davies collects the data for only 95 facets, which is possibly not a statistically significant data set for one to draw any conclusion.

A further problem with this approach is that it requires the region of interest to be larger than the size of the electron beam, otherwise this approach would give some averaged orientation across different grains under electron beam or producing contradicting EBSPs which confuses the indexing software during the reconstruction process.

Indirect Approach

In observing the drawbacks of the direct approach, especially the problem of the orientation error bar being as large as 5°, an indirect approach has been developed[28]. Unlike the direct measurement of the orientation on top of the fracture surface, the indirect approach measures the orientations on two polished surfaces perpendicular to each other. These two surfaces are usually vertical to the fracture surface under investigation and are polished by focused ion milling (FIB). Since the two surfaces are polished, the EBSPs are apparent and the normal EBSD measurement can be applied with high accuracy. The design of two surfaces instead of one is to remove the ambiguity because one surface would lead to ambiguous orientations which differ by a rotation around the normal of the polished surface. Nonetheless, with the extra surface, this degree of freedom is removed so the orientation on the fracture surface can be uniquely determined. Though this indirect approach solves the problem of inaccurate determination of the orientations of the direct approach, two new problems emerge. First, it is a destructive technique, because creating the two polished surface requires the destructively removing the materials using FIB, which means after the measurement, the sample is gone, and no further characterization is possible. The second and more serious problem is that this approach assumes the orientation on the fracture surface shares the same orientation as the two polished surfaces, which actually may or may not be true. The worst scenario is that the grain on the fracture surface is small compared to the spatial resolution available with EBSD and the measurements on the two polished surfaces actually measure the orientations of two totally different grains. Therefore, the indirect approach is usually applied to large grained materials.[26].

Conclusion Drawn from the SEM-based techniques

As mentioned earlier, the study of the distribution of the crystallographic directions normal to the fracture surface provides insights in understanding the fracture mechanism. Considerable efforts[19, 25, 26, 27] have been made to study the cause of the deformation by using the SEM-based techniques. Among all materials, Nickel-base superalloys have gained much interest[29, 30, 31, 32, 33, 34] due to it exceptional mechanical and chemical properties. Particularly, Miao[35] studies the fatigue crack initiation and propagation of Rene88DT at $593°C$ by a combination of serial sectioning orientation imaging and quantitative fractographic analysis and the statistics of 20 large facets show that the crystal planes are of $\{111\}$ type. And it is generally

believed that the deformation mode for Nickel-based superalloys is mostly associated with dislocations resulted from the {111} slip plane, however, a few exceptions like crack propagation along {001} are also observed[32, 33, 34].

Furthermore, due to the considerable experimental effort required by these SEM-based techniques, researchers are limited to study only crystallographic normals of facets (a microscopically large area for a fracture surface) while ignoring other potentially important areas. Typically, a study of tens of facets is quite common but not statistically significant in a strict sense.

Summary of Literature Review

Up to this point, we have seen the advantages and disadvantages of both approaches of SEM-based techniques. The disadvantages, especially, reveal the two distinctive aspects of the EBSD measurement. One is being a non-destructive technique while the other needs a polished surface. These two aspects are in conflict with each other and a single EBSD measurement cannot provide both simultaneously. This is reflected in the extreme choices of the two approaches' EBSD measurements. The direct approach keeps being a non-destructive method but ignores the requirement of a polished surface while the indirect surface keeps the requirement of a polished surface but has to be destructive. However, reconciling and unifying these two approaches is intrinsically impossible, thus we need a new technique to replace EBSD.

1.3 Objective

Now we know that the current state-of-the-art techniques fail to provide accurate measurements or impose restrictive requirements on the samples. Thus, a new technique with the capability of precisely measuring the crystallographic normals and the surface orientation is demanded.

With the advent of the third generation of synchrotron x-ray sources, a unique x-ray diffraction technique known as High Energy X-ray Diffraction Microscopy (HEDM) developed by Prof. Robert Suter's group in collaboration with Ulrich Lienert at the APS [36] and has been improved progressively with combined efforts [37, 38, 39, 40, 41, 42, 43] ever since. Designed to supersede EBSD, HEDM bears strengths in various aspects, like the high orientation resolution and more importantly the ability of interrogating orientations in a non-destructive fashion, which provides unprecedented perspectives to the new physical world. For example the observations of time evolution during grain growth [40] and stress process [42].

Furthermore, HEDM is an ideal candidate to extract crystallographic directions normal to the fracture surface because its greatest strength is being a non-destructive technique. Besides, it does not require a polished surface as EBSD does. Thus the two conflicting aspects of EBSD measurements dissolves are immediately removed. Additionally, HEDM has an orientation resolution of around 0.1° which is a big

advantage compared with the normal EBSD measurement, let alone the 5° error bar of the direct approach.

The main objective of this research is to develop a new technique to extract crystallographic characterization at the fracture surface. This new technique combines HEDM which performs orientation measurements non-destructively on a fracture surface, with high energy x-ray tomography to extract the 3D geometry of the fracture surface. The combination of these two experimental methods, together with further data analysis techniques, like volumetric registration and local normal estimation, allows us to create a new technique with much better accuracy than the SEM-based techniques, as will be illustrated in later chapters.

The second objective is to apply our new technique to investigate a particular fracture surface of interest. Not only the explanation of our new technique is furnished by the concrete experimental data, but also the crystallographic directions normal to the fracture surface is obtained as an output, and the distribution of the crystallographic normals is further analyzed to enrich our understanding of the fracture mechanism.

1.4 Outline

The rest of this thesis is organized as follows. Chapter 2 discusses the general processes of HEDM measurement regarding the experiment setup and the reconstruction procedure. Chapter 3 presents the specific experimental measurements of our new technique, where the general procedure is illustrated together with a measurement of a nickel superalloy sample and a quick data analysis is performed on the reconstructed volumes with some immediate results. Chapter 4 develops a robust registration framework for our technique, the main object of which is to align and merge HEDM and tomography volumes for later investigation and the goodness of registration is characterized and quantified. Chapter 5 presents the distinctive way that crystallographic normals to the fracture surface is extracted by using Principle Component Analysis (PCA) to estimate the local normal field and the distribution of the crystallographic directions normal to the fracture surface is studied to infer interesting results with respect to the fracture mechanism of the particular fracture surface of interest. Chapter 6 studies the fracture mechanism regarding the crack initiation by performing a deformation simulation on the aligned volume to predict the initiation site and compare the prediction with the experimentally determined location of the initiation site. Chapter 7 summarizes current research and proposes future directions, where the proposal using far field HEDM is emphasized.

Chapter 2

High Energy X-ray Diffraction Microscopy

HEDM is a unique synchrotron based technique, implemented at the beamline 1-ID at the APS in Argonne National Lab. The advent of the third generation of synchrotron x-ray sources, which facilitates the generation of high energy, high brilliance and monochromatic x-ray radiation, opens a bright door to the development of HEDM, as well as other synchrotron based techniques, like 3D X-Ray Diffraction Microscopy (3DXRD)[44, 45, 46] and Diffraction Contrast Tomography (DCT)[47, 48]. Among all these synchrotron based techniques, one unique feature of HEDM is the ability to probe defected polycrystalline materials so that direct measurements can be made on fatigued states. This unique technique provides unprecedented views in the studies of grain growth[40] evolution and plastic deformation processes[42], as well as bringing up the new technique to study the crystallographic directions normal to the fracture surface as we present in this thesis.

This chapter is going to cover the theoretical, experimental and reconstruction aspects of HEDM. We first present the motivation to develop such technique. Then we review some key theoretical results from the scattering physics, where we start with the scattering model in quantum mechanics under Born approximation and then discuss the scattering in the particular lattice context for both well-ordered samples and deformed samples. Equipped with theoretical knowledge of x-ray diffraction from a lattice, we then discuss the detailed implementation of the experimental setup at the APS. Afterwards, the general reconstruction procedure, how the diffraction images are reconstructed into the orientation maps using the forward modeling method, is explained.

2.1 Motivation

Throughout human history, people have been looking for new materials with new functionalities to make tools, such as a flint axe in the Stone Age, a sword in the

Bronze Age, a porcelain bowl in the Middle Ages, an aluminum bottle in the early modern period and an airplane in the last century. Although all these tools are essentially building blocks of our civilization, the discovery of such materials with new properties in the old days is typically a trial-and-error process. Not until the advent of solid state physics, did people start to gain new insights in making new materials guided by the knowledge of the material properties from the atomic level. But the theoretical study of solid state physics often assumes a perfect material, i.e. a single crystal. However, in reality, most materials in nature are polycrystalline, i.e. contain many single crystal grains. And people soon realized that the overall material properties for one sample is not just a simple summation of material property of each grain, but depends on the distributions of microstructures, like grain size, orientation and grain boundary. Thus for better understanding of the material properties and to make more sophisticated material, a 3D technique to map microstructures is badly needed.

Electron Backscatter Diffraction (EBSD) is a predecessor microstructure characterization technique which was invented around fifty years ago and was developed into an automated tool at Carnegie Mellon University (CMU). A typical measurement involves using a Scanning Electron Microscope (SEM) to generate Electron Backscatter Diffraction Patterns (EBSPs) and using an EBSD detector to record such diffraction pattern. Then crystallographic orientations are extracted by indexing and matching. One limitation of EBSD is because of the electron's small penetration depth on the order of $10 \sim 100nm$, which makes EBSD essentially a surface technique. Thus, in order to obtain the 3D microstructure information, ion milling must be performed to remove the surface that has been measured, to expose the underlying surface to be measured. So EBSD is forced to be a destructive technique which forbids the studies of time evolution mechanisms, like grain growth and strain response. And another drawback is that the sample must be polished to make the surface flat enough for observation, thus it causes some problems for studying the crystallographic directions normal to the fracture surface, as we will discuss later.

With the advent of the third generation of synchrotron radiation sources, HEDM was invented and implemented to overcome almost all EBSD's drawbacks. The introduction of high energy x-rays, which can easily penetrate samples of millimeters size for nearly all materials across the periodic table , makes HEDM a unique non-destructive technique, as well as other features like high orientation which will be discussed later. However, typical EBSD has spatial resolution in the submicron scale, which is better than the one of current HEDM. The spatial resolution of HEDM is limited mainly by the pixel size of the detector, which can be improved with the advancement of the semiconductor technology in building the detector.

2.2 Review of Scattering Physics

Scattering physics is the theoretical cornerstone of HEDM technique, and it explains some interesting phenomena during the HEDM experiment. So in this section we review the scattering physics, starting with the simple scattering model in quantum mechanics, followed by Born approximation and application to the diffraction from crystals model, which mimics the experiment for HEDM.

2.2.1 Scattering model in quantum mechanics

Let us consider an incoming X-ray wave function $|\phi\rangle$, interacts with scatters at position $\mathbf{x}'$ of potential V, and then the scattered wave function is denoted as $|\psi\rangle$. It can be shown that the relation between incoming wave function $|\phi\rangle$ and scattered wave function $|\psi\rangle$ is (similar to Equation 7.1.19 in J.J. Sakurai[49])

$$\langle \mathbf{x} \,|\, \psi \rangle = \langle \mathbf{x} \,|\, \phi \rangle - \frac{1}{\hbar} \int \frac{e^{\pm ik|\mathbf{x}-\mathbf{x}'|}}{4\pi|\mathbf{x}-\mathbf{x}'|} \langle \mathbf{x}' \,|\, V \,|\, \psi \rangle \, d^3\mathbf{x}' \tag{2.1}$$

where $\mathbf{x}$ denotes the location of observation, $\mathbf{x}'$ denotes the location of scatterer, k is the amplitude of the wave vector of the incoming wave function. Equation 2.1 says the scattered wave function $\langle \mathbf{x} \,|\, \psi \rangle$ is related to the incoming wave function $\langle \mathbf{x} \,|\, \phi \rangle$ with a correction term which accounts for the interaction of the between scattered wave function with the scatterer.

2.2.2 Born approximation

Note Equation 2.1 is hard to solve because scattered wave function $|\psi\rangle$ appears on both ends of the equation and further complicated by the interaction term with V. Here we introduce a simplification known as the Born approximation, which assumes the effect of the scatterer is weak. That is there is not much difference between incoming wave function $|\phi\rangle$ and $|\psi\rangle$, so it is plausible to replace $\langle \mathbf{x}' \,|\, \psi \rangle$ by $\langle \mathbf{x}' \,|\, \phi \rangle$

$$\langle \mathbf{x}' \,|\, \psi \rangle \approx \langle \mathbf{x}' \,|\, \phi \rangle = \frac{e^{i\mathbf{k}\cdot\mathbf{x}'}}{(2\pi)^{3/2}} \tag{2.2}$$

where $\mathbf{k}$ denotes the wave vector for the incoming wave function. And further assume the observation point is very far, i.e. r is large, then Equation 2.1 can be rewritten as

$$\langle \mathbf{x} \,|\, \psi \rangle = \frac{1}{(2\pi)^{3/2}} \left[e^{i\mathbf{k}\cdot\mathbf{x}} - \frac{e^{ikr}}{r} \frac{1}{4\pi} \frac{1}{\hbar} \int e^{i(\mathbf{k}-\mathbf{k}')\cdot\mathbf{x}'} V(\mathbf{x}') d^3x' \right] \tag{2.3}$$

The first term in the square bracket is the incoming wave function, as expected in the weak interaction, while the second term is the scattered wave function, where the exponent term $(\mathbf{k} - \mathbf{k}') \cdot \mathbf{x}'$ can be recognized as the phase difference between

the scatter at $\mathbf{x}'$ and the origin O. Besides the constants and the e^{ikr}/r term in the second term, the most interesting term is the scattering amplitude, which is defined as follows

$$A(\Delta\mathbf{k}) \equiv \int e^{i\Delta\mathbf{k}\cdot\mathbf{x}'} V(x') d^3x' \tag{2.4}$$

where $\Delta\mathbf{k} = \mathbf{k} - \mathbf{k}'$ and it says that the scattering amplitude is just a Fourier transformation of the potential distribution of the scatterers.

2.2.3 Diffraction condition for a lattice

For a perfect lattice, translational invariance is preserved for an arbitrary linear combination of translations along the crystal axes, $\mathbf{a}_1$, $\mathbf{a}_2$ and $\mathbf{a}_3$ for any discrete increments u_1, u_2 and u_3

$$V(x' + T) = V(x')$$

where $T = u_1\mathbf{a}_1 + u_2\mathbf{a}_2 + u_3\mathbf{a}_3$. It is well known that $V(x')$ can be Fourier transformed into reciprocal lattice space as

$$V(x') = \frac{1}{(2\pi)^3} \int e^{-i\mathbf{G}\cdot\mathbf{x}'} V(\mathbf{G}) d^3G \tag{2.5}$$

where $\mathbf{G}$ is the reciprocal lattice vector. Now within the context of a perfect lattice, Equation 2.4 can be rewritten as

$$A(\Delta\mathbf{k}) = \int e^{i(\Delta\mathbf{k}-\mathbf{G})\cdot x'} V(\mathbf{G}) d^3x' d^3G$$

If we assume all atoms in this lattice is identical, $V(\mathbf{G})$ is a constant and the scattering amplitude is nonzero when the diffraction condition satisfies the following criterion

$$\Delta\mathbf{k} = \mathbf{G} \tag{2.6}$$

This result can easily be extended to obtain the Bragg Law and Laue Equation.

2.2.4 Form factor and structure factor

A perfect lattice can be divided into basis cells and each basis cell shares the same atom configuration. Thus any atom at location $\mathbf{x}'$ can be represented as the n-th atom in the m-th basis cell

$$\mathbf{x}' = \mathbf{R}_m + \mathbf{r}_n \tag{2.7}$$

where $\mathbf{R}_m$ denotes the location of m-th basis cell as the center of mass position, and $\mathbf{r}_n$ denotes the location of the n-th atom in a basis cell. We assume each atom in the

lattice as a delta function in potential, so the integration becomes two summations with respect to m and n in Equation 2.4, which can be rewritten as

$$\begin{aligned} A(\Delta\mathbf{k}) &= \sum_m e^{i\Delta\mathbf{k}\mathbf{R}_m} \sum_n e^{i\Delta\mathbf{k}\cdot\mathbf{r}_n} f_j(\mathbf{G}) \\ &\equiv S(\Delta\mathbf{k})F(\Delta\mathbf{k}) \end{aligned} \tag{2.8}$$

where the first term $S(\Delta\mathbf{k})$ is known as the structure factor which is the summation of $\exp(i\Delta\mathbf{k}\cdot\mathbf{R}_m)$ over all lattice basis cells, while the second term $F(\Delta\mathbf{k})$ is known as the form factor which is the summation over all atoms inside basis cell. f_j is the coefficient of form factor for j-th atom, which is essentially the Fourier transformation of electron density over j-th atom.

2.2.5 Diffraction on deformed material

This section is expanded on Prof. Robert Suter's note [50] and the interested reader is referred to [51, 52] for further information. Let us start with revisiting Equation 2.4. An interesting observation is that the exponent term $\Delta\mathbf{k}\cdot\mathbf{x}'$ is only determined by the component parallel to $\Delta\mathbf{k}$. Thus, if we separate the variable $\mathbf{x}'$ into $\mathbf{x}'_\perp$ and $\mathbf{x}'_\parallel$, Equation 2.4 can be rewritten as

$$A(\Delta\mathbf{k}) \propto a_\perp \int_{L_\parallel} dx'_\parallel \bar{\rho}(x'_\parallel) e^{ikx'_\parallel} \tag{2.9}$$

where $\bar{\rho}$ is the laterally averaged density over planes perpendicular to $\Delta\mathbf{k}$ while $L_\parallel$ and $a_\perp$ are dimensions of the coherence volume. As Prof. Robert Suter mentioned in the note[50], the function $\bar{\rho}$ will contain periodic delta functions only in a perfect crystal at absolute zero temperature, while from thermal vibrations in crystals, one gets the Deby-Waller factor $\sim e^{-\frac{1}{3}\langle u^2\rangle k^2}$, where $\langle u^2\rangle$ is the mean square deviation from the lattice position and this Deby-Waller factor directly influences the intensities of the peaks. In the case of deformation, the intensity of the diffraction is further attenuated by the worsening of the atomic displacements farther from the periodic delta functions, which acts like an increased Deby-Waller factor and the smoother $\bar{\rho}$ yields diffuse scattering as well as reducing the high order Fourier components.

Besides intensity drop, other observations, like peak shift and peak broadening, often occur in x-ray diffraction experiments. Peak shift is typically caused by the lattice spacing (d-spacing) variations due to sample deformation. Due to the Bragg law $2d\sin\theta = n\lambda$, any change in d would lead to a variation in θ which is usually observed as the diffraction peak being shifted. Another possible reason for peak shifts is stacking faults, which describes the probability of faulted slip planes that are introduced during the deformation process. This effect was first report by Warren [53, 54], and later has been studied in various works[55, 56, 57, 58].

As for peak broadening, it can be attributed to many different reasons, like existence of lattice defects[59], dislocations[60, 61], stacking faults[54] and twinning[62, 63]. Due to this wide range of possibilities, the modelling of x-ray diffraction peaks under deformation is generally difficult to account for all effects, however, on the bright side, the experimental broadening peaks due to deformation, do contain valuable information regarding crystallite size distribution[59, 60], dislocation structure[60, 61, 64, 65], local strain state[66, 67] and lattice defects[68], which are otherwise hard to extract. The field, known as the *x-ray peak profile analysis*, has been an active researching field[59, 69, 70, 71, 72] in studying such peak broadening to extract useful information.

2.3 Experiment Setup

With the understanding of physics of the x-ray diffraction on a single crystal, we are now ready to present the experiment setup of HEDM. The essence is to apply x-ray diffraction on multiple grains simultaneously to infer the orientation, so the experiment setup bears resemblance to other x-ray diffraction based techniques, like Small-angle X-ray scattering (SAXS) and Wide-angle X-ray scattering (WAXS), but a distinctive difference in that HEDM uses a near field detector while both SAXS and WAXS use a far field detector.

Nonetheless, the idea of using far field detectors for HEDM has been formulated and effort has been made to build a dedicated experimental setup in Hutch C and E of the beamline 1-ID at the APS. In this sense, HEDM is further categorized as ff-HEDM for far field HEDM and nf-HEDM for near field HEDM. However, the experiments performed in this thesis are completely in the near field context. So every occurrence of HEDM in this thesis refers to near field HEDM unless otherwise specified.

The structure of this section is designed as follows. First an overview is discussed briefly to describe the big picture of the experimental setup, and then detailed information on each small component is presented. The order of each component is based on its position on the beamline, starting from upstream and progressing downstream.

2.3.1 Overview of Experiment Setup

Fig. 2.1 shows the schematic plot of the experimental setup for the HEDM measurement. A incident x-ray beam, typically plane focused to $1.3mm$ wide and a few microns high, illuminates a polycrystalline sample. Any grain, which satisfies the Bragg condition, diffracts the incident beam with certain 2θ angle. A charge-coupled device (CCD) camera is placed downstream, recording the locations and shapes of diffracted beams on the camera for all diffracting grains (schematically only one peak is shown here). This measurement is performed two or three times with the camera moving downstream to different x_d positions, namely L_1, L_2 and L_3. This potentially allows for the determination of the scatter vectors and back-tracking the origins of

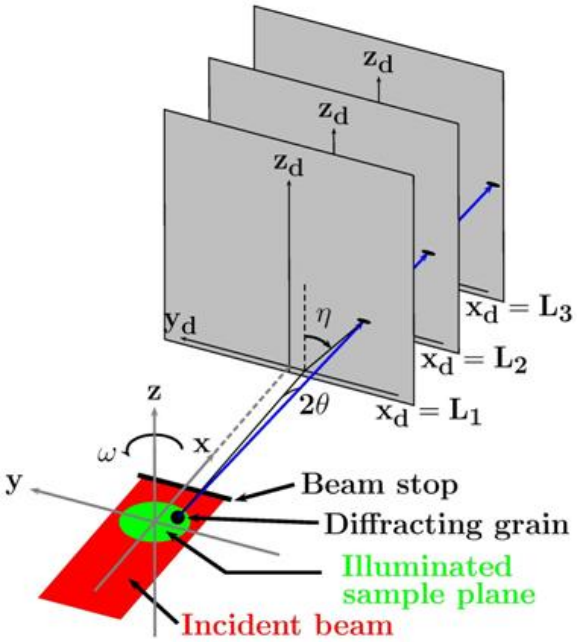

Figure 2.1: Schematic plot of experimental setup for HEDM measurement. A incident beam (in red), typically plane focused and illuminates the sample (in green). A grain (in black), which satisfies the Bragg condition, diffracts the incident beam with certain 2θ angle. A CCD camera is placed downstream to record the diffraction image. This image recording is repeated for different sample rotation ω and different x_d positions, namely L_1, L_2 and L_3.

the diffracting grains. For reconstruction algorithm, this places constraints on the possible simulated x-rays and provide the spatially resolved orientations. Also the sample is rotated to allow more grains being able to diffract x-ray beam so that its orientation information can be extracted from the diffraction images.

2.3.2 X-ray Beam

The reason that HEDM is performed at the APS is that HEDM has very special needs for the x-ray beam with the following characteristics

- High energy
- High brilliance
- Monochromatic

High energy is needed to allow the incident x-ray beam to penetrate the sample. Otherwise small penetration depth would not allow grains from locations inside the sample to be able to diffract the x-ray beam and be observed on the detector.

Brilliance is defined as the number of photons per second passing through a radial cross-sectional area for a certain energy. High brilliance is preferred since the x-ray diffraction is usually a small effect, because roughly on the order of 0.1% of the incident photons finally participates in the diffraction process, leaving the majority of the photons passing through the sample. If high brilliance is not guaranteed, counting time must be extended accordingly to ensure sufficient photons to be recorded for good signal to noise ratio.

Monochromatic x-ray beam is required to ensure the perfect x-ray diffraction since the above theoretical result on x-ray diffraction is based on the assumption of a monochromatic x-ray beam. If the x-ray beam is not monochromatic, i.e. it has a finite width $\Delta\mathbf{k}$ in $\mathbf{k}$ space. This would result in a finite width in the θ angle, as calculated in Dr. Daniel Hennessy[73]'s and Dr. Christopher Hefferan[74]'s theses. Typically, the energy spread of the x-ray beam at the beamline 1-ID is about 10^{-3} ($\Delta E/E = 10^{-3}$), which causes some problem studying the strain mechanism inside the sample, because the strain effect is roughly on the order of 10^{-4}. With the use of a second high energy resolution monochromator, we are expecting to have 10^{-5} energy dispersion, which should make a huge difference in strain/stress investigations.

2.3.3 Saw-tooth Lenses and Slits

After the x-rays are generated and pass through Hutch A for alignment and pre-focusing, two saw-tooth lenses and the monochromator are used to further focus the incoming x-ray beam in the vertical direction while leaving the size in the horizontal direction intact, i.e. to make the beam planar. The vertical size of the incoming x-ray beam for the measurements described here was $\approx 4\mu m$ but recent development by

beamline staff has brought down this size below $2\mu m$. After the saw-tooth lenses, a set of slits made of Tungsten carbide, known as `JJ` slits, are further used to define mainly the horizontal size of the focused beam. Four blades `JJtop`, `JJbot`, `JJleft` and `JJright` can be moved by motors controlled by the computer. Usually `JJleft` and `JJright` are adjusted to control the horizontal size while `JJbot` and `JJtop` are closed to reduce x-ray background.

2.3.4 Sample Stage

The sample stage is the stage where the sample is located. At its bottom, three motors control the location of its foundation, which are known as `StageX`, `StageY` and `StageZ`, with ability of translation in x, y and z directions. Then an air-bearing rotation stage `preciH` with ultrahigh precision rotation axis is mounted, and on top of the rotation stage, there are three stages controlled by three motors, `SampX`, `SampY` and `SampZ`. And finally on top of everything is the mounting position for the sample holder.

Since the sample is rotated during the HEDM measurement, it is imperative to ensure that the rotation axis is perpendicular to the beam and the rotation axis should be fixed during the rotation, i.e. any procession is not allowed. A precise centering scheme is developed using a $\sim 30\mu m$ gold wire as a calibration sample. First the gold wire is positioned on the sample holder with only its tip visible in the beam. Secondly, `SamX` is adjusted to the middle point of the locations of the tip at $\omega = 0$ and $\omega = 180°$. Similarly `SamZ` is adjusted at $\omega = 90°$. Finally, `StageX` is adjusted to bring the rotation axis to the center of the line-focused x-ray beam.

2.3.5 Beam Block

As mentioned earlier, the majority of the x-ray photons penetrate the sample without interacting because of the large penetration length of the high energy x-ray beam. Thus in the direction of the incoming x-ray beam, the intense transmitted beam will quickly saturate a large region of the detector and will obscure the much weaker diffraction signal of interest, as well as reduces the lifetime of the detector. To protect the CCD camera from direct exposure to the x-ray beam, a tungsten beam block is usually placed between the sample and the CCD camera to absorb. Sometimes, the beam on the tungsten beam block results in some diffraction patterns on the detector. Though the diffraction patterns usually are faint, they typically cover a lot of area on the CCD camera, which leads to some problems in the image reduction process, especially for those high q peaks which are relatively weak. Thus, typically, the beam block is rotated to minimize the effect of diffraction on the CCD camera.

2.3.6 Imaging System

The imaging system of the HEDM measurement is composed of three components: (a) a CCD camera with a $5X$ objective lens, (b) a 45° mirror, and (c) a scintillator screen. The scintillation screen converts the x-ray photons to visible light photons, so that they can be captured by the normal CCD camera. The CCD camera has an effective pixel size of $1.47\mu m$, after magnification by the objective lens, covers a pixel matrix of size 2048 by 2048, and with a depth of 12-bits for each pixel, i.e. with a dynamic range from 0 to 4095.

The CCD camera has a field of view of 3×3 millimeters and is usually placed in the near field region, a few millimeters from the sample. This near field configuration of the CCD camera ensures the high order scattering of photons being captured inside the camera's field of view, otherwise in the far field, only low order scattering is capture given the camera's field of view is fixed. The high order scattering is important in HEDM because it provides much more accurate information regarding to the shape of the grain in diffraction, compared with the low order scattering, where the peak shape of the grain is compressed in the vertical direction due to the projection geometry.

Before each HEDM measurement, the camera is calibrated to be placed into an optimal position to minimize the non-linear optical aberrations. A calibration procedure, known as the raster scan[75], has been developed. A small beam spot, which is defined by the `JJslits` just upstream of the sample, is imaged while the camera is translated horizontally and vertically perpendicular to the incident beam in a raster configuration (usually 3×3 or 5×5). The intensity distribution of each direct beam spot is fitted to a pseudo-Voigt function and the average full width half maximum (FWHM) is optimized by trying with different imaging system configuration. This procedure can reach pretty high resolution in that the horizontal translation stage has sub-micron precision while the vertical translation distances are measured using a displacement gauge head. Furthermore, the effective pixel pitch of the imaging system can be calibrated at the optimal configuration from the apparent motions of the imaged spots..

During the HEDM measurement, the same diffraction patterns are recorded for different sample-to-detector distances, L. Typically, the scintillator screen is placed roughly at the $5mm$ position from the sample first and then moved back $2mm$, i.e. at $7mm$ position with the diffraction images being taken at the two positions. The essence is to provide clues for the reconstruction algorithm to backtrack where the originating grain is located. Otherwise with single position diffraction images, there are infinite numbers of possible grain configurations which can produce such diffraction images.

Sometimes, a third camera position is used to take extra images as shown in Fig. 2.1. This is done solely for calibration purposes, as explained in the next section, for example when taking calibration measurement of a well-annealed gold sample, we usually take measurements at 5, 7 and $9mm$ positions to have the experimen-

tal parameters being more accurately pin-pointed. Another scenario of taking extra camera position is for a large volumetric scan. For a typical volumetric scan, e.g. with 50 layers, usually two or three layers are taken in $3L$-distances, with such layers interspersed evenly in the volume, to track the experimental parameters throughout the volumetric scan. That is because the experiment parameters may drift during a lengthy volumetric measurement, e.g. more than 12 hours, due to some environmental variations, like temperature. Then later in the data analysis stage, the parameter Monte Carlo procedure is performed, c.f. Section 2.4.4 on those $3L$-distance layers to re-optimize the experiment parameters, and those parameters can be interpolated to find the right approximate experimental parameters for those layers whose measurements are taken with only $2L$-distances.

2.4 Reconstruction Procedure

The goal of HEDM is to reconstruct crystallographic orientations for each small volume element, known as a voxel, and to produce orientation maps similar to EBSD. To obtain such orientation maps, after collecting the near field diffraction images in APS, the reconstruction process is undertaken in CMU, which usually is comprised of the following steps

1. Image reduction
2. Parameter determination
3. Orientation reconstruction

These three steps set the workflow for a typical HEDM reconstruction so we will discuss the normal operation for each step as follows and the structure of this section follows the order of the above three steps. Before discussing the steps, we introduce orientation notation and its relation with sample frame and crystal frame, because it is a key output of the reconstruction algorithm.

2.4.1 Orientation, sample frame and crystal frame

Before giving a formal definition of orientation in this section, we start off with the brief definitions of sample and crystal reference frames

- *Crystal frame* is defined as the coordinate system describing the microscopic atomic arrangement locally inside a crystalline grain of some material. The x, y and z-axes are typically the conventional basis vectors of the crystal structure, as defined in standard undergraduate solid state physics textbooks, like Kittel[51].
- *Sample frame* is defined as a coordinate system fixed to the macroscopic sample. The x, y and z-axes are typically the direction of the sample's length, width

and height. Our convention of the sample frame coincides with the lab frame (define later) at $\omega = 0°$. That is at $\omega = 0°$, the x-axis follows the direction of the incident beam, y-axis points to the left of the incident beam while the z-axis points upward, as illustrated in Fig. 2.1.

The key distinction here is that the crystal frame is totally different from the sample frame and our goal of the HEDM measurement is to relate local crystal orientations in the voxels to the sample reference frame since our samples are polycrystalline.

Knowing the fact that the crystal frame of one grain is different from the crystal frame of another grain, it is interesting to find a quantity to characterize the local crystal frame. Since all grains inside the same sample share the same sample frame, we can build each crystal frame by transforming the sample frame and essentially this is how the orientation motivated. It serves as the transformation which bridges the sample frame to the crystal frame

$$\mathbf{R}_{zxz}(\alpha, \beta, \gamma)\mathbf{v}_s = \mathbf{v}_c \tag{2.10}$$

The above equation says that for any vector $\mathbf{v}$, which can be represented as $\mathbf{v}_s$ in sample frame and as $\mathbf{v}_c$ in crystal frame, are connected by the orientation transformation $\mathbf{R}_{zxz}(\alpha, \beta, \gamma)$, which is represented in the Euler angle representation.

Euler angle is one particular representation of the rotation transformation. Besides Euler angle, other forms include axis/angle, rotation matrix and quaternion. And throughout this thesis, the Euler angle uses the x-z-x convention as illustrated in the subscript of the rotation transformation $\mathbf{R}$ in Equation 2.10. This means to coincide the sample frame to the crystal frame, a first rotation around z-axis is followed by a rotation around x-axis followed by another rotation z-axis.

2.4.2 Image Reduction

To reconstruct the orientation in each voxel, we will perform the forward modelling method[36] to simulate peaks and compare them with experimental peaks. Thus properly identifying peaks is a prerequisite for the success of the orientation reconstruction.

Previous image reduction algorithm[73] uses the following steps

1. Hot pixels, which result from stray x-rays possibly diffracted from some experimental instruments, are removed by a median filter, because they are usually composed of a couple of pixels with very high intensity.

2. A background image for the 180° scan is computed by averaging over all images in this scan, and each image subtracts this average images to remove the background which is static across all the diffraction images, e.g. diffraction pattern from the beam block, some defects on the CCD camera or on the scintillator

3. An intensity threshold, specified by the user, is further subtracted from each pixel. Essentially, the intensity below that threshold is considered as background while intensity above that threshold is considered as valid pixel for an experimental peak.

4. For all the valid pixels considered as components of experimental peaks, a graph algorithm to find the connected components is performed to group all valid pixels which are neighboring to each other, into experimental peaks.

5. For each identified peak, thresholding is performed by removing low intensity pixels within the peak. The low intensity is defined from the maximal intensity of the peak by a thresholding factor defined by the user. This post-processing is designed to alleviate the bias from the above steps, because the above background subtraction step uses a threshold value, which keeps more pixels in a high intensity peak instead of a low intensity peak.

This approach works perfectly with well-ordered samples. However, for deformed samples, Dr. Jonathan Lind[76] found that weak peaks neighboring high intensity peaks are frequently removed in the peak thresholding step thus fails to be considered as a candidate peak before the connected component step. This exclusion causes a big problem for forward modeling method because forward modelling suffers greatly if a true peak fails to be considered as a peak but it tolerates the error if a region of background is considered as a peak[43]. With this observation, Dr. Jonathan Lind improved the above reduction algorithm with a introduction of the Laplacian of Gaussian edge detection to replace the simple thresholding described above. This new reduction algorithm is studied in great detail[76] and it is shown that it provides a considerably more robust and accurate reconstructions result.

2.4.3 Forward Modelling Simulation

The kernel of the orientation reconstruction is the forward modelling method, which simulates the peaks given the experimental parameters and any candidate orientation and then the forward modelling simulation computes the locations of all simulated x-rays on the detectors as well as the ω intervals for all the peaks. Given the finite size of the detector, not all peaks need to be simulated – only scatterings up to a user-defined threshold $Q_{\max}$ are simulated

$$\sqrt{h^2 + k^2 + l^2} \leq Q_{\max}$$

where $h, k, l \in \mathbb{N}$. As the list of all the candidate (h, k, l) tuples can be generated, we can simulate peaks from each (h, k, l) based on the diffraction condition as shown in Equation 2.6, which says the momentum transfer $\Delta\mathbf{k}$ equals a reciprocal lattice vector $\mathbf{G}$. And in the following two paragraphs we will show how these two quantities

can be parametrized by unknowns like ω interval of the simulate peak, which will be eventually determined after equating these two quantities.

For $\Delta\mathbf{k}$, since (h, k, l) is known, the angle θ between the incident beam direction $\mathbf{k}_i$ and the diffraction beam direction $\mathbf{k}_f$ can be determined easily by the Bragg's law. Furthermore $\mathbf{k}_i = (1, 0, 0)$ by definition, all possible values of $\mathbf{k}_f$ form a cone with an angle of 2θ from $\mathbf{k}_i$, thus we can introduce a value η to parametrize the location of $\mathbf{k}_f$, where η is defined as the angle tilted from the z-axis as illustrated in Fig 2.1. Under this parametrization of $\mathbf{k}_f$, the momentum transfer $\Delta\mathbf{k} = \mathbf{k}_f - \mathbf{k}_i$ can be retrieved in terms of the η.

For $\mathbf{G}$, since we know the vector representation in the crystal frame, which is $\mathbf{G}_{hkl}$, it is easy to compute the vector representation in the sample frame by the given orientation. A further step is needed to rotate the vector in the sample frame by an angle of ω, where ω is to be determined. Essentially $\mathbf{G}$ is parametrized in terms of ω.

Finally, the two vectors $\Delta\mathbf{k}$ and $\mathbf{G}$ are equated and the parameters η and ω are solved. I am summarizing the key steps of the calculation as follows, where the step 2 is for the computation of $\Delta\mathbf{k}$ while step 3 is for the computation of $\mathbf{G}$

1. Compute all the scatterings up to a threshold $Q_{\max}$ which are denoted as $\mathbf{G}_{hkl}$

2. Compute θ angle for each (h, k, l) by Bragg's law, parametrize $\mathbf{k}_f$ with η and represent momentum transfer $\Delta\mathbf{k}$ by $\mathbf{k}_f$

3. Transform $\mathbf{G}_{hkl}$ from the crystal frame to the sample frame using the orientation $\mathbf{R}_{zxz}(\alpha, \beta, \gamma)$ by Equation 2.10, then rotated by ω to the lab frame, where ω to be determined.

4. Equate $\Delta\mathbf{k}$ and $\mathbf{G}$ to solve for ω and η.

Pictorially, all the possible values of $\mathbf{G}$ for different ω form a right circular cone with the axis in the positive z-axis, while all the possible values of $\Delta\mathbf{k}$ form another right circular cone with axis in the x-axis. Thus there are two solutions for ω and η if the cones intersect but no solution at all if the two cones do not intersect.

2.4.4 Experimental Geometry Determination

Experimental parameter determination is another prerequisite for any method. The forward modeling method needs such parameters to simulate the whole experimental setup and generate the diffraction peaks. The parameters to be determined are the following

- Beam center (j_0, k_0), which is the projection of the intersection of the rotation axis and the incident x-ray beam onto the detector, along the beam propagation direction at each L-distance

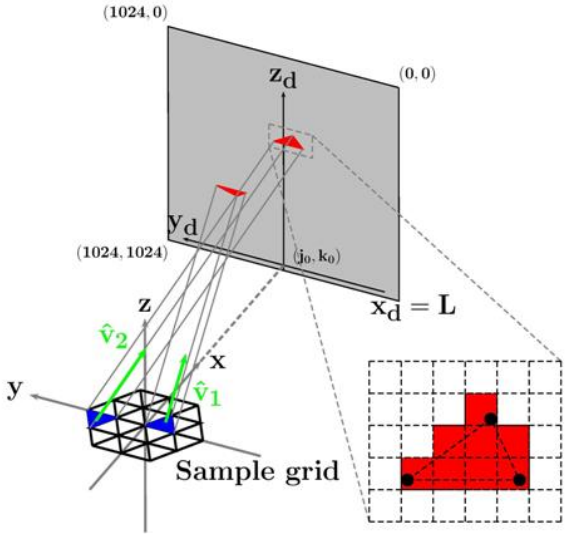

Figure 2.2: Schematic plot of forward modeling method at certain L-distance of $x_d = L$. The sample space is subdivided into triangular grid and two voxels (in blue) with candidate orientation generates two scattering with wave vectors (in green) denoted as $\mathbf{v}_1$ and $\mathbf{v}_2$ respectively and illuminates the CCD camera with two distinctive peaks (in red).

- The rotation axis-to-detector distances, L_is
- Camera orientation, for the camera may be tilted or rotated a little bit relative to the ideal, perpendicular orientation

For each L-distance, the detector has six parameters to be determined (two for beam center, one for camera location, three for camera orientation), and for a typical $2L$-distance HEDM measurement, the total number of parameters is 12 and 18 for $3L$-distance HEDM measurement. Even for the 12-dimensional parameter space, the curse of high dimensionality prevails. To solves this problem, a Monte Carlo scheme was developed by Prof. Robert Suter[36], which fits a small number of voxels while perturbing experimental parameters using a Monte Carlo scheme based on a particular measure of goodness-of-fit, which will be presented in the next section. The original Monte Carlo method has been substantially improved by S.F. Li[43, 77].

2.4.5 Orientation Reconstruction

After all the peaks are identified and accurate experimental parameters are obtained, the forward modeling algorithm can be performed to reconstruct the orientation field. Fig. 2.2 shows the schematic of the forward modeling method.

First the sample space is subdivided into equilateral small triangles (voxels). Fig. 2.2 illustrates a typical sample space in a black sample grid of a hexagonal shape, however, the sample space could be any shape as the user desires.

Our goal here is to find the orientation for each voxel, which is one particular orientation of the whole orientation space $SO(3)$. This whole $SO(3)$ space has redundant regions due to the crystal symmetry, e.g. cubic symmetry and hexagonal symmetry, so it can further be reduced to a unique subspace, known as the fundamental zone. To find the *right* orientation within the fundamental zone, we must design a measure of "goodness-of-fit" for any orientation. Ideally this measure compares the experimental diffraction images with the simulated diffraction image of the given orientation based on the retrieved experimental parameters. One particular measure is called *confidence*, which is defined as the ratio of the number of *overlapping peak*s to the number of *qualified peak*s, where an overlapping peak is a simulated peak that overlaps with an experimental peak while a qualified peak is a peak that intersects multiple detectors.

Given the definition of confidence, in theory, we could identify the right orientation in the fundamental zone which has the best confidence score. However, the fundamental zone is a continuous orientation space, thus for scientific computation, an algorithm is developed to uniformly grid the fundamental zone space to generate a list of candidate orientation at any given resolution. Nonetheless, it is still impractical to perform an exhaustive search at the measurement resolution since the candidate list is too long to work with. To solve this problem, S.F. Li[43, 77] devised the *Stratified Monte Carlo Pruning*, where only the lower order scatterings are compared at early stages using the coarse gridding of the fundamental zone to identify the possible subregions where the right orientation may reside, and then at later stages such candidate subregions are further refined and higher order peaks are compared until a convergence criterion is reached, finally a local Monte Carlo optimization on the orientation is performed to alleviate the effect of orientation griding.

Chapter 3

Experimental Methods

The goal of this chapter is to present the detailed experimental methods for a new technique, which extracts the crystallographic information at the surface. This new technique is supposed to replace the current state-of-the-art techniques using EBSD and photogrammetry, which will be discussed in detail in Chapter 5. In this chapter, we focus on the experimental methods which is a combination of HEDM and x-ray tomography. Though the general approach of HEDM measurement is explained in the preceding chapter, we discuss the specific experimental settings for our measurement and the x-ray tomography measurement will be elucidated as well.

The structure of this chapter is following. First the material of the sample and the sample preparation procedures are presented. Then the experimental setups for HEDM and x-ray tomography measurements are presented, followed by the discussion about the data acquisition processes. Finally, the reconstruction of both measurements are discussed, and some analysis results will be presented.

3.1 Sample Preparation

3.1.1 Material

The material of the sample in our experiment is Rene88DT[78], which is one member of the family of nickel-based superalloys. The nickel-based superalloys are widely used in aerospace industry to fabricate the hottest components, for example the turbine blades inside a jet engine, because of their exceptional mechanical and chemical properties at high temperature[79]. Due to its wide application in the aerospace industry as well as other industries, enormous effort has been made to study its microstructure for further improvement of material properties for such applications.

The sample was prepared in GE Global Research, where a bulk of Rene88DT sample of a cylindrical shape with a diameter around $6mm$ was used as a starting point of a series of sample preparation procedures, as illustrated in Fig. 3.1(a).

3.1.2 Cyclic Loading

Cyclic loading is the process of applying repeated or fluctuating stress to a sample to fatigue or fracture the sample in a similar way as the sample would have been fractured in its working environment. Cyclic loading has been widely used to study the fatigue analysis to study sample's material properties under stress.

In our example, the bulk sample as mentioned above was fatigued at $399°C$ between 0 and 0.65% strain using a triangular waveform at 30 cycles per minute. Failure occurred after $96,101$ cycles. During the cyclic loading, an experimental procedure, known as the plastic replica method, is performed to identify the location where the crack initiates, which will be discussed in Chapter 6.

3.1.3 Mechanical Cutting

As mentioned in previous chapter, the experimental setup of HEDM requires that the whole layer of the sample is always inside the x-ray beam throughout the measurement, which puts a hard constraint on the size of the sample by the size of the beam and the penetration depth of the x-rays. In the Hutch B at the 1-ID beamline at the APS where these measurements were performed, the line focused x-ray beam width is around $1.3mm$. The two fracture pieces after the cyclic loading, being of dimension $6mm$, are too large to be put into the beam. Thus an electrical discharge machining (EDM) procedure is performed to extract a cylindrical pin of diameter around $1mm$ for each fractured piece to be allowed in the beam, as illustrated in Fig. 3.1(b). The locations of the pins are specifically chosen to include the initiation site found previously via the plastic replica method. The two extracted pins are denoted as $S1$ and $S2$, respectively, for later references.

3.2 Tomography and HEDM Measurement at the APS

After the sample preparation, the two pins $S1$ and $S2$ were measured in two separate beam runs at the beamline 1-ID at the APS. As is usual in HEDM work, data collection for these samples was a group effort. The first beam run, which took place in February, 2011, included Dr. Christopher Hefferan, Dr. Jonathan Lind and Dr. S.F. Li. The second beam run, which took place in November, 2013, included Dr. Christopher Hefferan, Dr. Jonathan Lind, Dr. Reeju Pokharel and me. Since the experimental setup for both beam runs are identical, in this section, we will describe this experimental setup.

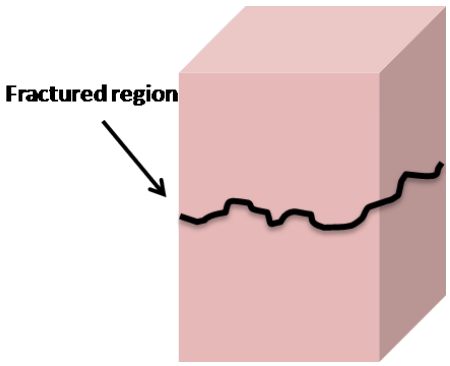

(a) The Starting Bulk Rene88DT

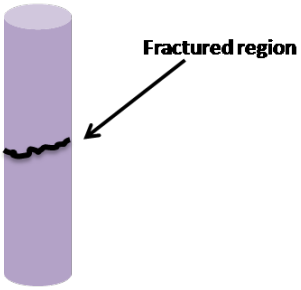

(b) Pins Extracted by EDM

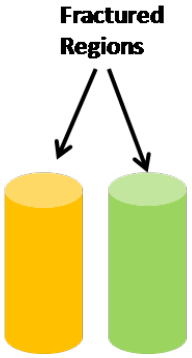

(c) Pins Separation

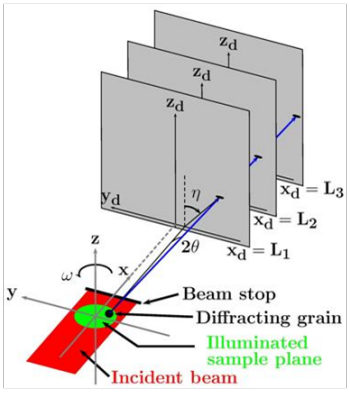

(d) HEDM Measurement for One Pin

Figure 3.1: Schematic diagram showing the workflow of the sample preparation and measure procedures.(a) The starting material is a bulk Rene88DT sample of diameter $\sim 6mm$. Cyclic loading is applied and the sample is fractured in the middle, as illustrated in black line.(b) Mechanical cutting is performed to extract two pins from the resulting two samples covering the initiation site. These two pins are of cylindrical shape with $1mm$ in diameter, and are later referred as $S0$ and $S1$. (c) The two pins $S0$ and $S1$ are separately measured, with one inverted as shown. Note both fracture surfaces are on top and this is the way that they will be put in the beam, which results in the need for a coordinate transformation in later analysis. (d) Two pins are put in the x-ray beam to do the HEDM measurements.

3.2.1 HEDM measurement

Orientation maps were obtained by the HEDM measurements at the beamline 1-ID at the APS with the following experimental setup and settings. Monochromatic high energy x-ray beams were operated at 65.351keV and 64.351keV for $S1$ and $S2$ respectively and planar beams with a size $\sim 1.3mm$ in width and $\leq 4\mu m$ in height illuminated the two pieces. A total of 58 and 53 layers for pins $S1$ and $S2$ respectively were measured and the diffraction images were collected. For most layers, two L-distance configuration was used, in which diffraction images were taken at two detector locations. A couple of layers were measured interspersed in the whole volume under the three L-distance configuration ($4.764mm$, $6.764mm$ and $8.764mm$ for $S1$ and $5.799mm$, $7.799mm$ and $9.797mm$ for $S2$), which served the purpose to calibrate and interpolate the experimental parameters for the parameter Monte Carlo. Layers #7 and #18 in the pin $S1$ and layers #19 and #39 in the pin $S2$ were measured in the three L-distance configuration. For each L-distance, a scan was performed covering a sample rotation range of 180° with images being integrated over $\delta\omega = 1°$ intervals to allow diffractions of various grains to be spotted and the diffraction patterns being captured by the CCD camera. The imaging system is composed of a 12-bit 2048×2048 CCD camera, a scintillator screen and a 5X focusing lens. The effective pixel sizes are $1.48\mu m$ and $1.46\mu m$ for $S1$ and $S2$ respectively, determined from the raster scan. The counting time for each image was 5 seconds and 2.2 seconds respectively, and the deadtime between images was 1.7 seconds for mechanical motion.

3.2.2 High Energy X-ray Tomography Measurement

X-ray tomography or x-ray micro-computed tomography (μCT) is a standard measurement used in medical imaging and the method of reconstructing three dimensional images of material density or more precisely absorption length contrast is well established.

In our experiment, the saw-tooth lenses were removed and upstream slits were positioned so as to obtain a $1.5mm \times 0.8mm$ beam to illuminate the sample at once. This volumetric based scan drastically increased the efficiency of data collection, compared with the layer-based scan of HEDM. The same imaging system was used, where transmission images were recorded rather than diffraction images. The rotation scheme again covers a range of 180° but with finer increment of 0.2°.

The sample stage was carefully aligned to ensure the perpendicularity of the sample during rotation in the beam and the detector was calibrated to yield pixels rows perpendicular to the rotation axis, which facilitates the later reconstruction. That stationary features on the detector typically cause circular features in the reconstruction.

3.3 Tomography and Orientation Reconstruction

The reconstruction of the x-ray tomography volumes and HEDM volumes are performed at CMU after the data collection is done. For the reconstruction procedures, the methods to reconstruct tomography volumes have been well established and documented[80, 81] and the reconstruction procedure of HEDM information was fully presented in 2.4. So in this section, the reconstruction procedures will be briefly mentioned and we will focus more on characterizations of the reconstructed volumes.

3.3.1 Reconstruction of X-ray tomography volume

The procedure of the tomography reconstruction can be summarized briefly as follows. Hot pixels are first removed using a 3×3 median filter. The detector pixel rows with the same height for different ω rotation are stitched together to form sinograms and the `Matlab`™ routine `iradon` based on inverse radon transformation is utilized to reconstruct each layer. The final material density is scaled to a 8-bit integer ranging from 0 to 255.

Fig. 3.2 shows reconstructed material density images of several representative layers from the top of the fracture surface to the bulk for both $S1$ (left column) and $S2$ (right column), respectively. The color scheme is white for full material density, i.e. 255 and black for void material density, i.e. 0. For both tomography volumes, the material density is sparse for layers on the top of the fracture, as illustrated by the few white regions in Fig. 3.2(a) and Fig. 3.2(b). On the other hand, Fig. 3.2(e) and Fig. 3.2(f) shows the layers close to the bulk region where most of the region is covered by the full material density.

One interesting feature is an almost flat edge, which is apparent in the left lower corner of Fig. 3.2(e), and a little bit less evident in the left upper corner of Fig. 3.2(f). This is actually the edge of the much bigger bulk sample that the mechanical cutting has been performed and now it serves as a fiducial marker for the later registration and alignment of the two pieces. The two different directions of the two fiducial edges indicates the two samples are not mounted to the sample holder at precisely the same angle. In fact, since the measurements were performed during two different beam runs, no attempt was made to perform such an alignment during the measurement. So further registration is required to align these two data sets so that the two sides of the fracture surface can be digitally aligned.

The other interesting feature is the similar features between the center black void space in Fig. 3.2(e) and Fig. 3.2(f). The latter image can be rotated and matched to the former image like solving a puzzle. This is expected since the two pins come from the same sample. More formal and detailed analysis will be discussed later.

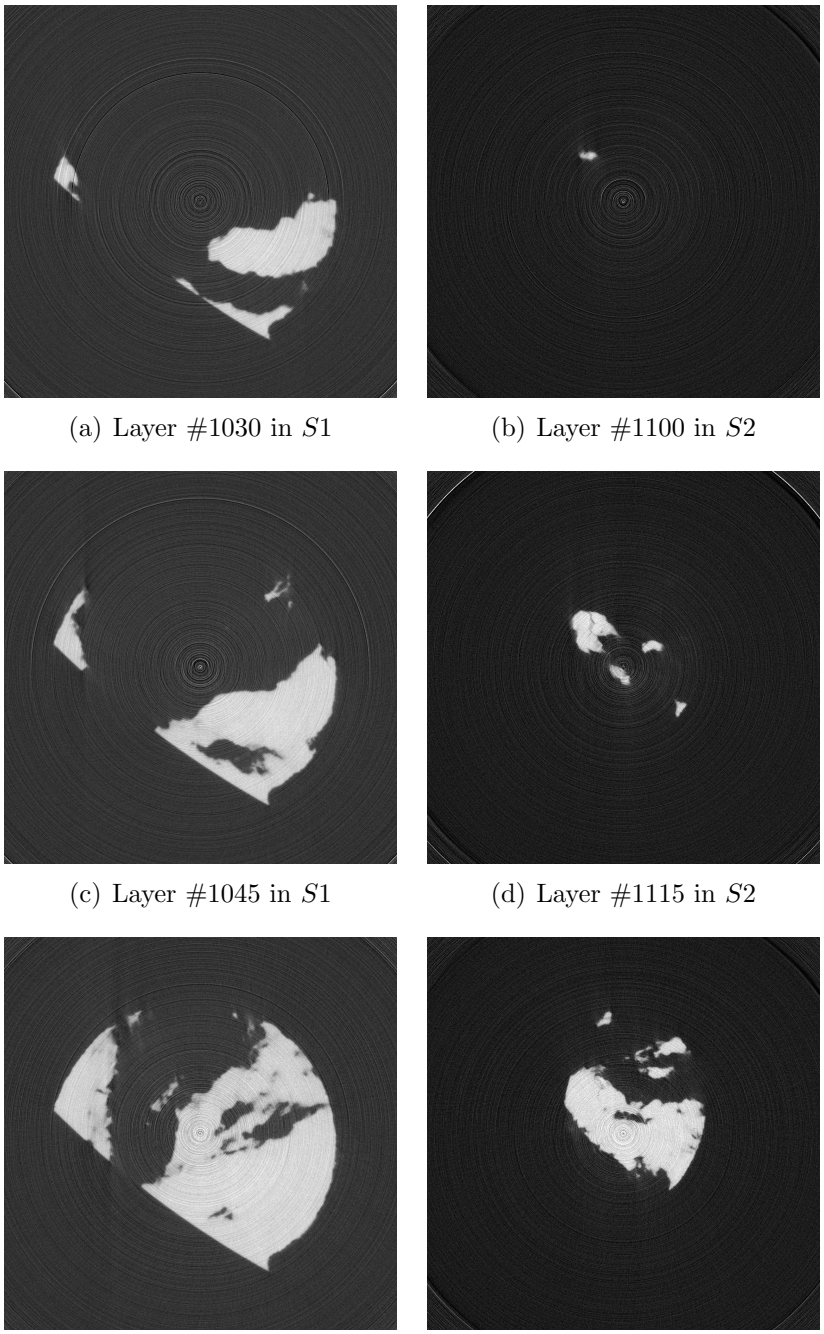

(a) Layer #1030 in $S1$

(b) Layer #1100 in $S2$

(c) Layer #1045 in $S1$

(d) Layer #1115 in $S2$

(e) Layer #1060 in $S1$

(f) Layer #1130 in $S2$

Figure 3.2: Selected reconstructed images for two pins $S1$ and $S2$, where white represents the high material intensity and black represents zero material intensity, i.e. vacuum. The left column shows the reconstructed layers from the top (a) of the fracture surface in $S1$ to layer close to the bulk (e). Similarly, the right column shows layers from the top (b) to the bulk (f).

Table 3.1: Optimal parameters for pins $S1$ and $S2$ from parameter Monte Carlo. (j_i, k_i, L_i) forms a tuple of parameters for the ith detector, $i = 1, 2, 3$, where (j_i, k_i) is the projecting location on the detector of the intersection between the rotation axis and the incident x-ray beam and L_i is the rotation axis-to-detector distance. Both j_i and k_i are in pixels, while L_i is in millimeters.

Pin	j_1	k_1	L_1	j_2	k_2	L_2	j_3	k_3	L_3
$S1$	1019.97	2032.81	4.764	1019.90	2032.78	6.764	1019.90	2032.79	8.764
$S2$	1025.83	2010.96	5.799	1025.49	2009.89	7.799	1023.43	2008.41	9.797

3.3.2 Reconstruction of HEDM volume

The reconstruction of the orientation maps are performed according to the procedure described in 2.4. The new image reduction routine developed by Dr. Jonathan Lind[76] was used. Parameters were determined by parameter Monte Carlo. The parameter Monte Carlo procedure was performed first on the $30\mu m$ gold wire and the resulting parameters were further optimized by the calibration layers with three L-distances where the maximum scattering vector $Q_{\max}$ was set to be $9\mathring{A}^{-1}$. The optimized parameters are listed in Table 3.1. Total 58 layers for $S1$ and 53 layers for $S2$ are reconstructed using the optimized parameters using IceNine software. Sample space is subdivided into equilateral triangles of size $1.56\mu m$ and orientations are reconstructed using a speed-up method, known as the mask trick. This trick is inspired by the observation that the layer above always has less area to be fitted than the current layer. So one can always use all the voxels being fitted in the layer below, possibly with filtering of low confidence voxels, as a mask to define the voxels to be reconstructed for the current layer and start the fitting from the bottom layer and work the way up in the reverse order of layer indices. This trick is estimated to reduce 1/3 of total CPU time that would be otherwise wasted, because some voxels fitted in the current layer are possibly ignored in all layers above, which leads to a huge speed-up because a voxel for which no orientation is found requires the maximum CPU time since other searches can converge without testing all possible orientations.

Fig. 3.3(a) and 3.3(c) show the orientation maps for two particular layers from $S1$ and $S2$. In the orientation maps, a patch of the same color usually represents a grain, however, note that the voxels' orientations are reconstructed independently, the orientation of neighboring voxels are not necessarily the same but may differ in small amount. But due to the relatively coarse gridding in the RGB color space, this small difference may be smoothed out or cannot be resolved by human eyes.

Fig. 3.3(b) and 3.3(d) show the corresponding confidence maps for the above two layers. The confidence is a particular measure of the certainty of the reconstructed orientation and it is one of the outputs from the reconstruction software. The confidence $\mathcal{C}$ is scaled into the $[0, 1]$ range, with $\mathcal{C} = 1$ indicating every simulated Bragg peak matches observed scattering while $\mathcal{C} = 0$ indicating no simulated scattering matches observation. As shown in Fig. 3.3(b) and 3.3(d), the majority area is cov-

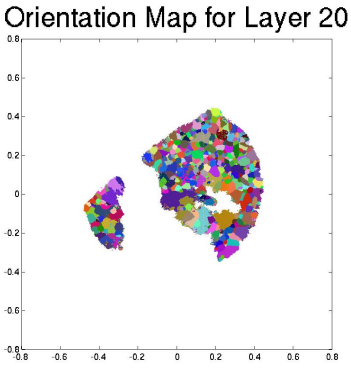

(a) Orientation Map of $S1$ Layer 20

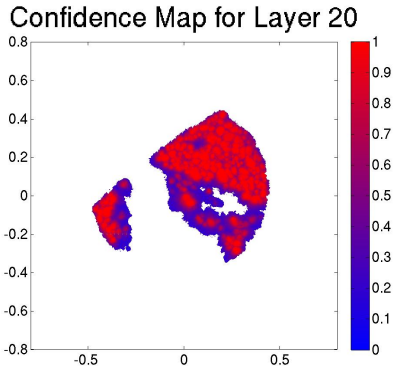

(b) Confidence Map of $S1$ Layer 20

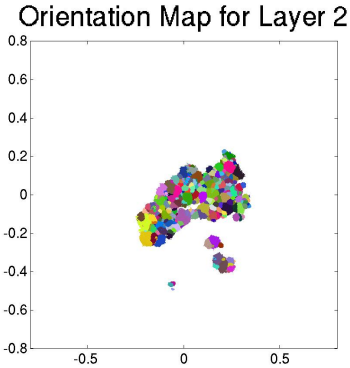

(c) Orientation Map of $S2$ Layer 2

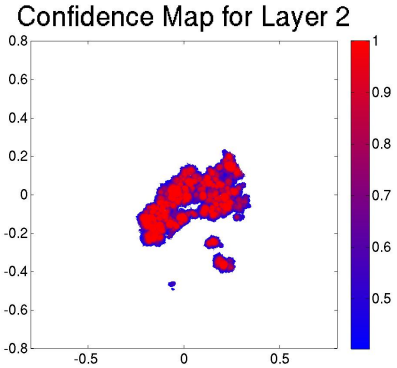

(d) Confidence Map of $S2$ Layer 2

Figure 3.3: Representative reconstructed layers for two pins $S1$ and $S2$. The left column shows the orientation maps, where the orientations are converted to Rodrigues vector representation and these vector components are scaled to RGB colors[82]. The right column shows the confidence maps, which describes how confident the orientation reconstruction is for each voxel. The confidence $\mathcal{C}$ is scaled to $[0, 1]$, where $\mathcal{C} = 1$ means perfect confidence which is indicated by the red color while $\mathcal{C} = 0$ means zero confidence which is indicated by blue color. Layer 20 for $S1$ and Layer 2 for $S2$ are chosen to represent other layers in the volume to illustrate the similarities in grain size and reconstruction quality.

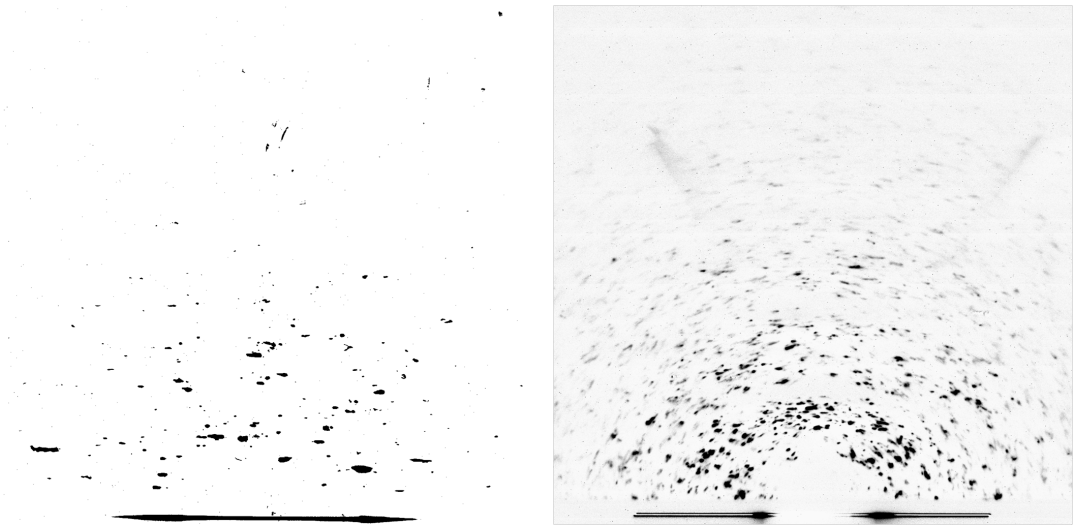

(a) Well-ordered Nickel (b) Fracture surface

Figure 3.4: Detector images of diffraction patterns of (a) a well-ordered Nickel sample and (b) layer 40 of pin $S2$. The well-ordered nickel sample results in shiny and well-shaped Bragg diffraction peaks, while the fractured pin $S2$ leads to weak and faint Bragg diffraction peaks. The difference in terms of the peak intensity distribution causes difference intensity scaling for aesthetic reasons. Two faint streaking areas on the top of (b) are from the artifacts of the beam block which is removed by reduction algorithm before reconstruction.

ered by red color, indicating high confidence on the reconstructed orientations and the blue color, indicating low confidence, is usually located at the edge, which will be revealed to be the boundary of the fracture surface later. Besides the edges, there are blue areas which are the grain boundaries. The drop of the confidence corresponds to the drop of the intensity of Bragg peaks in the detect image as approaching to the sides of a grain.

During the measurement of pin $S2$, we did not collect data from the very top because the x-ray scattering was scarce and, at the time, it was thought not be reconstructible.

3.3.3 Observation of missing peaks due to deformation

As we discussed in Section 2.2.5, the assumptions of perfect x-ray diffraction does not hold for deformed samples where peak shifts and peak broadening can occur. Thus the purpose of this section is to demonstrate such occurrences and to reconcile the experiment with the reconstruction.

For well ordered samples with $> 20\mu m$ grains, x-ray diffraction results in well-shaped Bragg peaks. The peaks are characterized as high intensities, sharp edges

and homogeneous intensity distribution within a peak as illustrated in Fig. 3.4(a) for an annealed Nickel sample. However, for a deformed sample like the fracture surface sample in our experiment, the Bragg peaks are usually weaker, heterogeneous and the edges are hard to identify because of the wide transitions from the high intensity to background intensity. To illustrate this, we show a representative detector image from the layer 40 of pin $S2$, in 3.4(b). Note this is a raw detector image before any image processing or reduction algorithm. One observation is that the peaks from our sample are not as large as the ones in the annealed nickel sample. This is because our sample is generally filled with small size grains. The averaged grain cross-section radius study can be found in Section 3.4.2 and it shows the average grain cross-section radius is around $25\mu m$ which approaches the small end of the spectrum of the nf-HEDM measurements, and the sample itself is fractured. These two factors strongly contribute to the weak and broad peaks. The other observation is that the peaks from our sample are weak and inhomogeneous compared with the ones from the nickel sample. Recall that the detector used in our experiment is 12-bit which has a dynamic range up to 4095, and for visibility, we threshold the gray scale of Fig. 3.4(b) to $[90, 149]$ to show most of the peaks. This clearly indicates most of the peaks are weak, on the order of one hundred counts. This possibly results from the deformation when our sample was fractured.

Another interesting feature in Fig. 3.4(b) is the arc-like diffraction pattern, which is quite common in far-field diffraction measurements due to the large sample to detector distance, but not in near-field measurements, as confirmed by the diffraction image of the nickel sample in Fig. 3.4(a). This indicates the orientations inside a grain are not necessarily uniform. Instead the possible orientation gradient inside a grain due to deformation, leads to this arc-like pattern. Also, deformation generates defects inside grains, which reduces intensity and broadens peaks into arcs in both ω and η (η is the angle describes the location in the 2θ ring, c.f. Section 2.4.3).

More raw detector images and reduced images for representative layers throughout the volume are shown in Fig. 3.5. The left column shows a series of raw images from layer 0 (the topmost layer in pin $S2$) to layer 30 (in the bulk of $S2$). Note all these raw images are scaled to the same intensity range of $[90, 149]$ as in Fig. 3.4. Fig. 3.5(a) shows very few Bragg peaks since the top layer has considerably less material than other layers. One interesting observation is that the arc-like pattern and the peak spread persist even in the bulk layer, for example in Fig. 3.5(c). It is widely believed[3, 4] the deformation is most predominant in the fracture region and becomes less pronounced deep in the bulk. However, our detector images provide direct evidence that the layers rather deep in the bulk are also deformed.

It is also interesting to check the goodness of reconstruction from this deformed sample by simulating the Bragg peaks from reconstructed orientation map and compare these to the experimental peaks. If the sample is reconstructed perfectly, i.e. ideally the reconstructed orientation map is the same as the sample, the diffraction from the reconstructed orientation map should produce all peaks in the detector im-

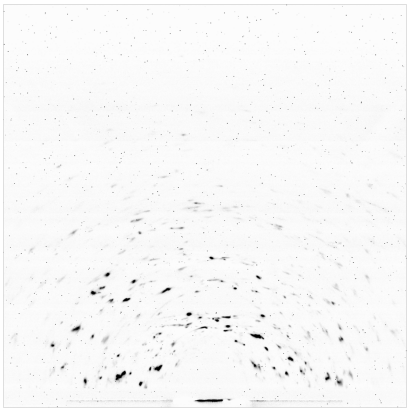

(a) Raw image for Layer 0

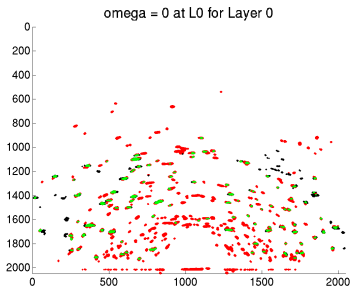

(b) Overlap image for Layer 0

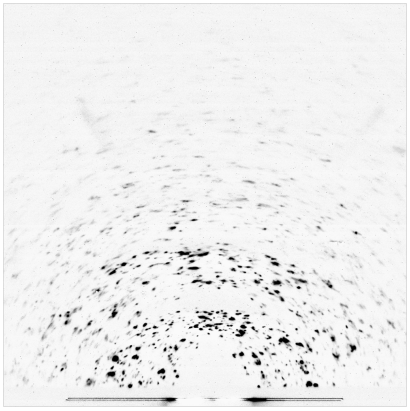

(c) Raw image for Layer 10

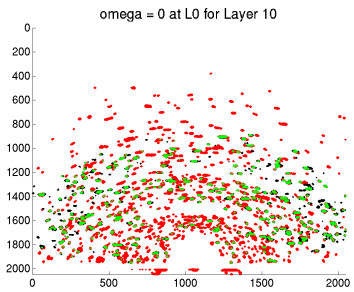

(d) Overlap image for Layer 10

Figure 3.5: Detector images of diffraction patterns and overlap images for representative layers for pin $S2$. The layers are from 0 (the top of the fracture) to 10 (inside to the bulk). The left column shows the raw diffraction images, i.e. before being reduced to identify the peaks, which clearly shows arc-like peak pattern and peak spread, even in the layer which is inside bulk. This indicates the deformation in the bulk of the sample. The right column shows the overlap image, which essentially is a overlapping between the simulated peaks (from the reconstructed orientation map) and the experimental peaks (after reduction). The color scheme is that red represents peaks only from experimental, black represents peaks from simulation, while green means the current pixel is overlapped by both the simulated peaks and the experimental peaks.

ages with perfect overlap. This comparison is generally quite good for well-ordered samples with over 90% of the experimental peaks being overlapped by the simulated peaks.

The right column of Fig. 3.5 shows the overlapped images for $S2$ layers from 0 to 30. For all the overlapped images, only a small portion of apparent peaks are green,

representing overlap between simulated and experimental scattered intensity, while many scattering remain red, representing those experimental Bragg peaks which are not overlapped by any simulated intensity. On the other hand, there are only rare instances in which simulated intensities do not overlap with experimental intensities. We refer these experimentally observed intensity that are not overlapped by the simulation as *missing*.

The first impression in looking at the right column of Fig. 3.5 is that there is a lot of scattering in the measurement that is not reproduced by the reconstructions. One might conclude that the signals shown in the raw detector images are simply too complex for reliable reconstruction. We therefore undertook a search, although somewhat anecdotal, to determine the origin and nature of the missed peaks. To account for the origins of the missing experimental intensities that are not overlapped by the simulation, a manual procedure was followed. The first question to ask is whether these intensities are physical and if they are, are they consistent with x-ray diffraction from the nickel crystal structure. To answer this question, a back-projection is performed. For a missing peaks on the detector image at position $L1$ and a particular ω interval ω_i, we manually determine a corresponding spot at $L2$ and the same ω_i based on the shape of the peak. This allows calculation of the diffracted beam direction yielding 2θ and η (c.f. Section 2.4.3 for definitions of 2θ and η). For valid diffraction , 2θ should correspond to a specific family of Bragg peaks $\{hkl\}$. For valid diffraction, the diffraction is back-projected to the sample space to find which location of the grain which would have generated the missing intensities. We then ask if the observed diffraction is consistent with the crystal orientation found at the back-projected location. The missed scattering intensities are generally weak compared to scattering that is overlapped by the simulation, as illustrated in the images on the left column of Fig. 3.5. We found that most of the missed scattering is from the tails of stronger scattering that occurs in neighboring ω images and/or in neighboring neighboring layers and that is overlapped by the simulation where it is strong.

To illustrate, we explain the origins of two particular peaks, circled in purple and blue in 3.6(a), which has been verified as valid Bragg scattering. For the purple peak, we simulate the diffraction of reconstructed orientation map at the neighboring ω bin $\omega = 1^\circ$, as illustrated in 3.6(b). At the exactly same position, which is circled in purple, in the neighboring ω bin shown in Fig. 3.6(b). This indicates the experimental peak is spread across $\omega = 0^\circ$ and $\omega = 1^\circ$ because of deformation. However, in the HEDM reconstruction of orientation of each voxel, forward modelling algorithm assumes perfect x-ray diffraction on a perfectly ordered sample without considering a modelling of deformation. That is why the reconstruction picks up the spot at $\omega = 1^\circ$ but not $\omega = 0^\circ$.

The blue peak as illustrated in 3.6(c), however, is not in the neighboring ω bin. Instead it is originated from the grain from the layer below, as shown in Fig. 3.6(d). By comparing the overlapping peak generated from layer 1, another peak, which is

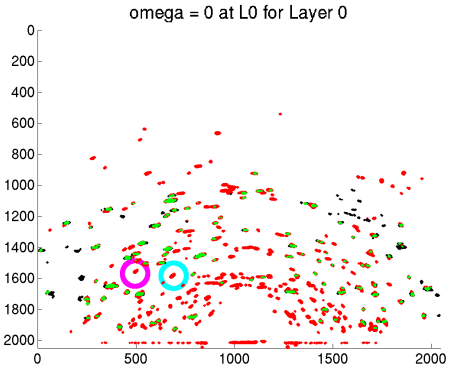

(a) Layer 0, $\omega = 0°$

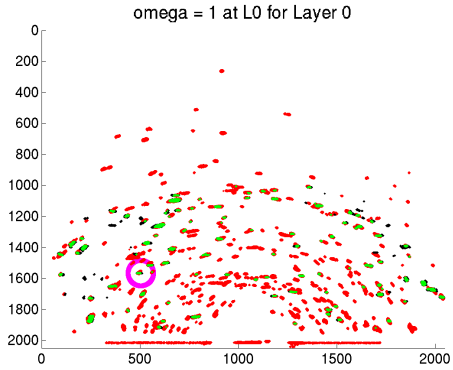

(b) Layer 0, $\omega = 1°$

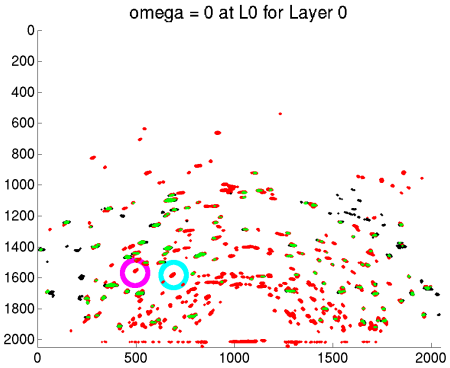

(c) Layer 0, $\omega = 0°$

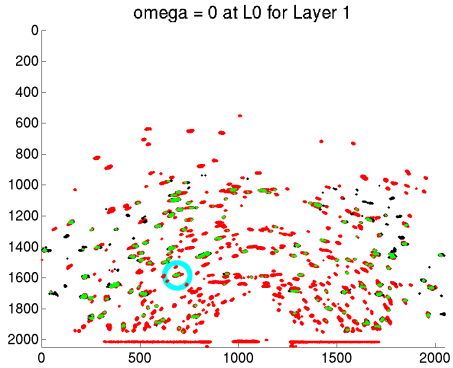

(d) Layer 1, $\omega = 0°$

Figure 3.6: Illustrations of the origins of two missing peaks, circled by blue and purple color. (a) and (b) explains the origin of the missing peak circled in purple is from the peak shift at $\omega = 1°$. (c) and (d) explains the origin of the missing peak circled in blue is due to the finite hight of the incident x-ray beam.

circled in blue color in Fig. 3.6(d) with almost the same shape, shows up at the same detector position for layer 0 and more importantly this peak is overlapped by simulation. This reveals another assumption we made in our reconstruction algorithm that the incoming x-ray beam has zero height, while in experiment our beam has a finite height. So our reconstruction algorithm reconstructs an orientation map for a layer of zero height, at the nominal in the center of the finite experimental beam. The experimental illumination can provide other x-ray diffraction peaks from other parts of the physical beam. This explains why we can have physically existent Bragg peaks from experiment, but the forward modelling does not pick up this signal. However, this effect is significantly reduced for well-ordered samples with relatively large grains.

Here we only demonstrate the origins of two particular peaks, however, due to the enormous number of peaks, it is impractical to account for the origins for all the missing scattering. Currently, the reconstruction algorithm is striving for incorporation of local strain effect and intensity fitting. This issue can be perfectly solved with the updated implementation of reconstruction algorithms in the near future. A smaller focal size has also been achieved in the new Hutch E end station where current and future work will be conducted.

3.4 Characterization of the Bulk Superalloy Sample

After reconstruction of the tomography and HEDM data sets, it is interesting to characterize some important statistics for our sample, which serve as cornerstones for later investigation. In this section, we study four quantities. Edge width for tomography data, the grain cross-section radius distribution, volumetric texture of the orientations and grain orientation variation.

3.4.1 The Edge Width for Tomography Data

The edge width is defined as the width of the measured transition between high material density in the bulk and low material density which is considered as a background or vacuum. The reason to characterize the edge width here is because it is is an important measure of the error bar of the reconstructed tomography features. For later investigations, it characterizes the goodness of the volumetric registration as well as indicates the missing materials during the fracture process.

To characterize this width, an error function of the following form is applied to selected density transitions

$$f(x; x_0, d, A, B) \equiv B + \frac{A}{2} \cdot \left[1 + \operatorname{erf}\left(\frac{x - x_0}{d}\right)\right] \tag{3.1}$$

where x_0, d, A, B are all the parameters to be determined, x_0 is the position of the center, d is a measure of the width as we will discuss soon, A is the amplitude of the

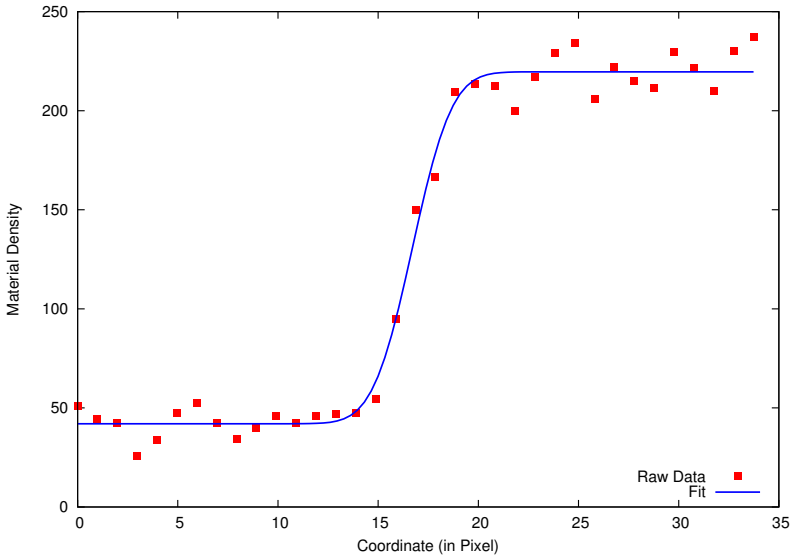

Figure 3.7: Plot of material density profile across the boundary. The blue data points are the tomographically measured density at different coordinate points, which clearly shows two plateaus (the left being air or background, while the right being the bulk material). The red line is the error function parameterization of the transition.

transition and B is the background material density. And $\mathrm{erf}(x)$ is the standard error function which is defined as

$$\mathrm{erf}(x) = \frac{2}{\sqrt{\pi}} \int_0^x e^{-t^2}\, dt,$$

for $-\infty < x < \infty$ which implies that the function range is $-1 < \mathrm{erf} < 1$. Fig. 3.7 shows a material density profile for a particular edge across the fracture boundary in blue data points. A non-linear fitting routine of the function form in Equation 3.1 is applied to the data and the fitted values are computed and plotted as the red line. The comparison shows quite satisfactory agreement.

To characterize the width of the edge, we define the width to be the Full Width Half Maximum (FWHM) of the error function, i.e. the range in x axis corresponds to $f(x; x_0, d, A, B)$ being between $B + A/4$ and $B + 3A/4$, or equivalently the FWHM of the underlying Gaussian function. According to the numerical table for the error function, $\mathrm{erf}(0.477) \approx 0.5$, thus $f(x; x_0, d, A, B) = B + A/4$ corresponds to $x = x_0 - 0.477 \cdot d$ and similarly $f(x; x_0, d, A, B) = B + 3A/4$ corresponds to $x = x_0 + 0.477 \cdot d$, so the FWHM is equal to $0.477 \times 2 \times \hat{d}$, where $\hat{d}$ is the fitted value of d in Equation 3.1. The fit of $f(x)$ to the raw data is applied using `gnuplot`, which determines the FWHM to be $3.6\mu m$ which is 2.4 pixels. This is confirmed by the reading on the data points in Fig. 3.7. Comparing the fact that the resolution of the tomography reconstruction is roughly 1 pixel, the FWHM of the edge is as small as 2.4 pixels, which indicates the precision of the determination of boundary points.

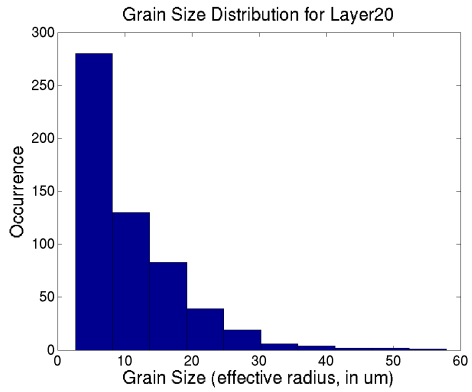

(a) Grain Cross-section Radius Distribution of $S1$ Layer 20

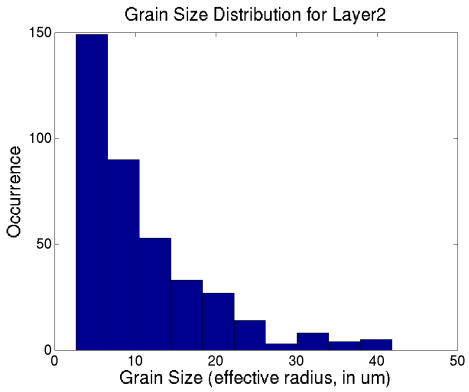

(b) Grain Cross-section Radius Distribution of $S2$ Layer 2

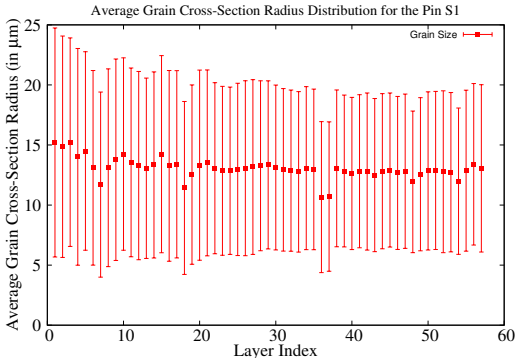

(c) Average Grain Cross-section Radius of $S1$

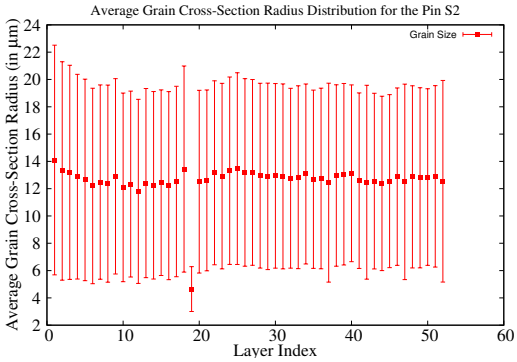

(d) Average Grain Cross-section Radius of $S2$

Figure 3.8: Plots of the grain cross-section radius distributions. (a) and (b) show the histograms of the grain cross-section radius distribution for the two layers shown in Fig. 3.3, where the grain size is computed as the effective radius in micrometres. (c) and (d) show the computed average grain sizes as a function of the layer index for pins $S1$ and $S2$ respectively.

3.4.2 Grain Cross-Section Radius Distribution

The grain cross-section radius distribution is an important statistics for grains inside a sample, where a *grain* is defined as a crystallite with a single lattice orientation. In our grain cross-section radius computation, a grain is defined by the maximal 2° misorientation convention. That is a misorientation between two neighboring voxels larger than 2° considers these two voxels to belong to different grains. The effective grain size is computed from its cross sectional area and further converted to effective radius assuming the grain is of circular shape. Fig. 3.8(a) and 3.8(b) show the grain cross-section radius distribution for the two layers shown in Fig. 3.3. We can observe a similar pattern that the occurrences decay as a function of the grain cross-section radius. There is a great number of grains of small size ($< 5\mu m$ in radius) and large

grains ($> 30\mu m$ in radius) are scarce.

Fig. 3.8(c) and 3.8(d) show the computed average grain size for all layers of pins $S1$ and $S2$, where the average grain size of a particular layer takes the average over all grains of that layer weighted by the area of each grain cross-section. Both pins show similar average grain cross-section size. The average grain cross-section size is roughly around $12.5\mu m$ in radius and this $12.5\mu m$ average grain size corresponds to the small end of the spectrum of nf-HEDM measurements so far.

3.4.3 Volumetric Texture

Texture is the distribution of the orientation of a polycrystalline sample and a sample is said to have texture if it has a preferred orientation. Texture is an important statistics because preferred orientation usually influence of the properties of the material.

To quantify the distribution of the crystallographic orientations, people generally resort to *pole figure* and *inverse pole figure*. Due to the abstract nature of orientation in plotting, both the pole figure and inverse pole figure convert the distribution of orientations to the distribution of vectors and adopt a stereographic projection to collapse the distribution of 3D vectors to a 2D map. However, they differ in terms of the context of plotting. The pole figure displays the distribution of orientations of a particular crystallographic direction in the sample frame. For example for the {111} pole figure, all grains' {111} directions in the sample frame are collected and their distribution is projected stereographically in 2D. On the other hand, an inverse pole figure displays the distribution of a selected sample frame direction distributed in the crystal frame. A typical application of inverse pole figures is to study which direction in the crystal frame that is most likely parallel to the sample frame direction.

A popular and powerful software for texture analysis is called `mtex`[1] and all the pole figures and inverse pole figures are plotted in `mtex`. Fig. 3.9(a) and 3.9(b) show inverse pole figures of all grain orientations in the two pins from the perspective along the (001) sample direction, i.e. z-axis. Though a little bit differences maximal intensities, both of them show maximum at the {111} crystal directions. Thus this sample is textured. A double check is performed by plotting the {111} pole figures, as shown in Fig. 3.9(c) and 3.9(d). The strong intensities at the centers of both pole figures indicate texture. However, the peak at two times a random distribution indicates only weak texture compared to, say a drawn wire or extruded material.

3.4.4 Grain Orientation Variation

Ideally, a grain is a perfect crystallite with a single orientation. In reality due to the existence of deformation, the orientations inside a grain may vary. Thus the orientation variation is a great indication of the deformation level. Since our sample is deformed, it is interesting to quantify such deviations.

[1] `https://code.google.com/p/mtex/`

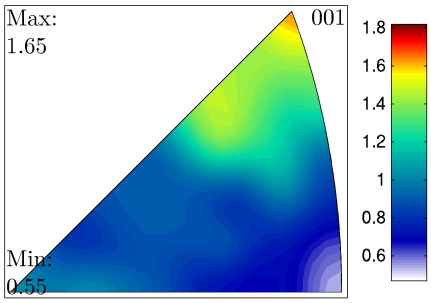

(a) Inverse Pole Figure for $S1$ Volume

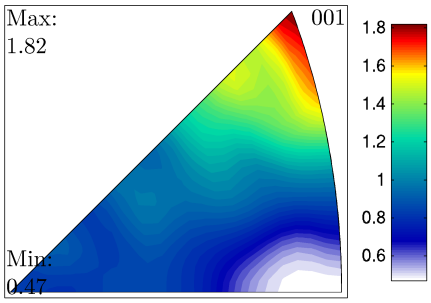

(b) Inverse Pole Figure for $S2$ Volume

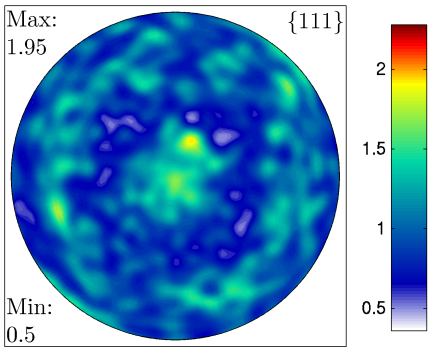

(c) Pole Figure for $S1$ Volume

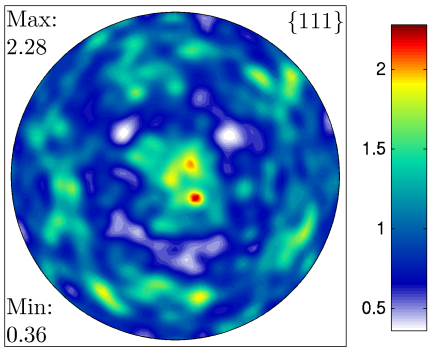

(d) Pole Figure for $S2$ Volume

Figure 3.9: Volumetric texture plots for the pins $S1$ and $S2$. Fig. (a) and (b) show the inverse pole figures along the sample z-axis, i.e. (001). In both subfigures, the left corner represents $\{001\}$, the right corner represents $\{110\}$ while the upper corner represents $\{111\}$. And the color scheme for both subfigures is scaled between 1.82 (red) and 0.47 (white). Fig. (c) and 3.9(d) show the pole figures for the $\{111\}$ poles and the color schemes are rescaled between 2.28 (red) and 0.36 (white).

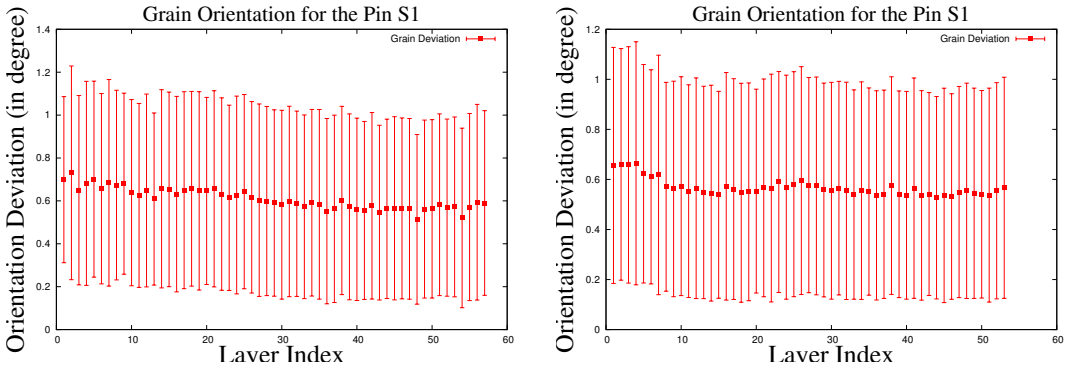

(a) Orientation Variation for $S1$ Volume (b) Orientation Variation for $S2$ Volume

Figure 3.10: Orientation variation plot as a function of layer index for (a) the pin $S1$ (a) the pin $S2$.

During the computation of the grain orientation variation, we adopt the same 2° misorientation convention to define a grain, as in Section 3.4.2. Then average grain orientation is computed by averaging corresponding quaternions of each orientation and special care is taken to track all 24 symmetry equivalent orientations and assign them to the right subgroup to account for the shape of the fundamental zone. Once the average orientation for each grain is computed, the misorientation of each voxel from the grain average orientation is computed, also known as *intra-granular misorientation (IGM)*

$$\Delta\mathbf{R}_i \equiv \mathbf{R}_i^{-1}\mathbf{R}_{\text{avg}}$$

where $\mathbf{R}_{\text{avg}}$ represents the average grain orientation, $\mathbf{R}_i$ represents the orientation of the ith voxel inside the grain and $\Delta\mathbf{R}_i$ is the ith voxel's misorientation matrix. In our orientation variation computation, we are interested in the misorientation angle, i.e. the angle needed to rotate to coincide $\mathbf{R}_i$ with $\mathbf{R}_{\text{avg}}$ and we define *orientation variation for a grain* as the average of the all misorientation angles of all voxels inside the grain. We are also interested in the *orientation variation for a HEDM layer*, which is defined as the average over all grains' orientation variations for a HEDM layer

$$\langle\Delta\mathbf{R}\rangle \equiv \frac{1}{n}\sum_{j=1}^{n}\langle\Delta\mathbf{R}_j\rangle$$

where $\langle\Delta\mathbf{R}\rangle$ represents the layer's orientation variation, n represents the number of grains in that layer and $\langle\Delta\mathbf{R}_j\rangle$ represents jth grain's orientation variation. We also define the standard deviation of the orientation variation as the standard deviation of all grains' misorientations $\langle\Delta\mathbf{R}_j\rangle$.

Fig. 3.10 shows the plots of the orientation variation for all layers of the pins $S1$ and $S2$. Both subfigures show similar trends that the layer's orientation variation drops as the layer index increases, i.e., as going into the deep of the bulk material.

Even the deepest layers inside the bulk display finite orientation variations, which are not too different from the highest value of orientation variations from the top layers. This indicates that even deep inside the bulk, the deformation still has an influence. This is confirmed with the diffraction images where peak broadening and shift are still observed (c.f. Section 3.3.3). The most striking feature of Fig. 3.10 is that the standard deviation (error bars) is large compared to the weak trend toward lower orientation variations as one moves away from the fracture surface. Thus, different grains experience significantly different spreads in orientation and this characteristic does not correlate with position relative to the fracture surface.

Since orientation variations of all layers are more or less the same, we deem 0.7° as the average orientation variation for the whole sample.

Chapter 4

Registration and Merging of Tomography and HEDM Data

The HEDM and x-ray tomography measurements for two distinct pins $S1$ and $S2$ lead to four volumetric data sets, and in order to extract meaningful results in the later chapters, it is necessary to combine all these four data sets together as a whole sample like it was before being fractured by cyclic loading. Thus the purpose of this chapter is to develop a robust registration and merging framework for our new technique combining HEDM and x-ray tomography.

In this chapter, the detailed registration and merging techniques will be discussed as follows. We will start with primitive tomography layer alignment based on image registration in Section 4.1, then we present a novel registration technique using volumetric data rather than layered data in Section 4.2 and finally we evaluate the robustness of the volumetric registration in Section 4.3.

4.1 Primitive Tomography Layer Alignment

Image registration is a set of standard processes that transform images to bring them into a unified coordinate system and it has various applications in photography, medical imaging, computer vision, etc.. As mentioned briefly in the preceding chapter, Fig. 3.2(e) and Fig. 3.2(f) bear similarity, indicating a good candidate for image registration and the quality of registration is supposed to be high since the two pins are originally from the same sample. This image registration technique is primitive in the sense that it works only on layers of the sample but not on the whole volume. Though more advanced volumetric registration will be presented later, this image registration serves as a building block for later volumetric data set.

4.1.1 Image Registration on a Sample Layer

In this work, the image registration is performed by Insight Segmentation and Registration Toolkit (ITK), which is a open-source, cross platform image segmentation and registration library written in `C++`, which is composed of a collection of image registration algorithms, e.g. pattern intensity algorithm, mutual information algorithm, etc.. A general image registration algorithm usually contains three important components: cost function, transformation scheme and optimization method. Essentially, an image registration problem can be viewed as a specific optimization problem, which minimizes the difference, defined by a cost function, between two images. A transformation is applied to one of the images, defined by a transformation scheme and parameters are optimized by some algorithm.

For our problem, efforts have been made to try out different image registration algorithms provided by ITK. Among them, a simple algorithm called *mean square* bears the best results, considering efficiency and quality. In the mean square algorithm, the cost function is the mean square of the intensity difference for each pixels of the two images. The transformation scheme is a 2D rotation and translation and the optimization method is gradient descent which is based on the fact that the gradient can be evaluated efficiently.

Before registration, several image preprocessing steps are needed, i.e. justifying a unified coordinate system, choosing the corresponding transformation and image inversion to produce the right inputs for image registration algorithms.

Fig. 4.1(c) and 4.1(d) demonstrate the quality of image registration by comparing the difference image between the two images before and after the registration, respectively. The difference image is the intensity subtraction of the two images on a pixel-by-pixel basis and then rescaling the intensity to $[0, 255]$. Fig. 4.1(d) shows the matching after registration. Clearly almost all the features are perfectly matched except a white corner.

The investigation of the white corner leads to an interesting discovery of the image registration, which reveals the fact that during the sample preparation, the pins $S1$ and $S2$ were extracted off-axially, as illustrated in Fig. 4.2. This leads to the necessity of trimming away non-overlapping portions for the quantitative registration described below. This is referred to as the *mechanical cutting problem*.

4.2 Volumetric Boundary Point Registration

Image registration is a typical 2D technique which works on single layer of either tomography or HEDM data. Though it detects the mechanical cutting problem, the 3D nature of the volumetric data in our experiment calls for a volumetric registration scheme. The purpose of this section is to develop a general 3D volumetric registration scheme to align tomography volumes as well as aligning tomography volumes with HEDM volumes. In this section, we start off with a discussion of the general approach,

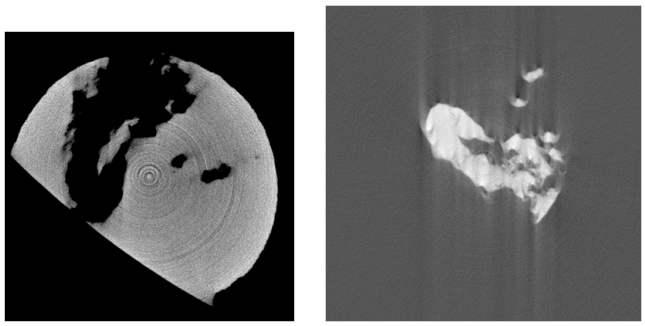

(a) Layer 1066 from $S1$ (b) Layer 1132 from $S2$

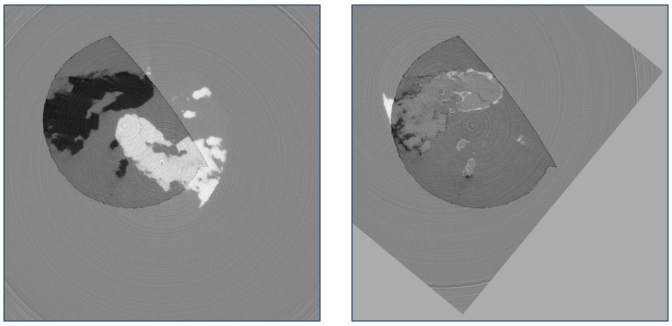

(c) Difference image before registration (d) Difference image after registration

Figure 4.1: Registration of two tomography layers from the pin $S1$ and $S2$ that bears similar features. (a) shows the reconstructed tomography layer 1066 from pin $S1$. (b) shows the reconstructed tomography layer 1132 from pin $S2$. (c) shows the difference image between the two images before registration. (d) shows the difference image after registration, which shows almost perfect registration. Note the difference image is the image of intensity subtraction between two images and rescaled intensities to $[0, 255]$.

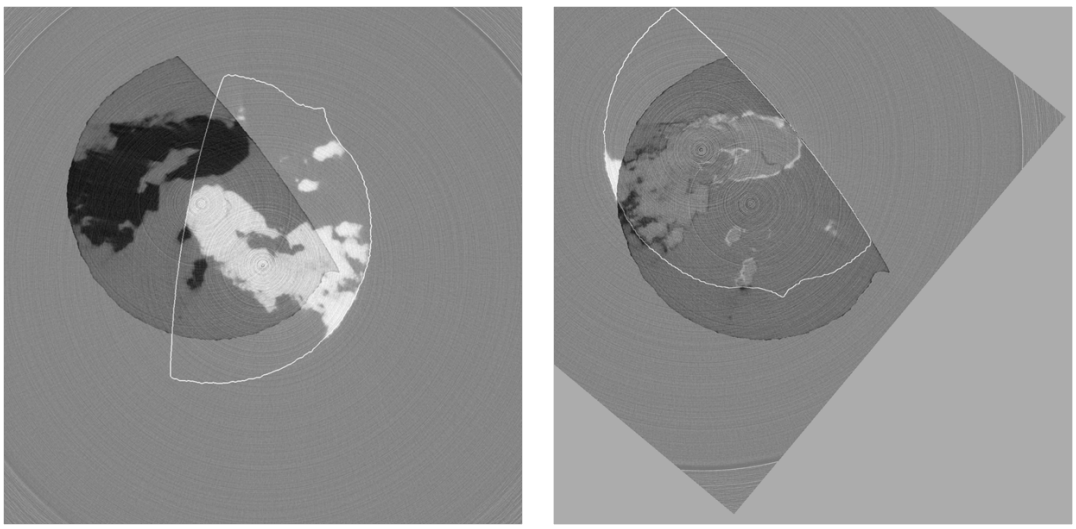

(a) Before Registration (b) After Registration

Figure 4.2: Aligned matching the same layers as in Fig. 4.1 from $S1$ (dark) and $S2$ (light). The white line shows the sample edge from a bulk layer superimposed to show that the two samples were not cut on the same axis.

like the motivation, pre-processing and procedures. Then we will apply this general approach to specific problems, i.e. 3D registration between tomography volumes and between tomography and HEDM volumes. The discussion which quantifies the goodness of registration is left to the next section.

4.2.1 General Approach

The use of boundary points in our volumetric registration scheme is motivated from the observation of the image registration process, for example from Fig. 4.1, that the most important information for registration is the feature information, i.e. the boundary of the samples, not the points in the bulk region. That is if we manage to extract the boundary of the samples by taking the gradient of the image, and repeat the image registration process, we should be able to retrieve the same registration result. One advantage of this process is that it heavily reduces both the memory and CPU computation because the bulk pixels, which are previously majority of all data points, are now ignored. More importantly, this idea to use only the boundary points can easily be extended to 3D space, because the 3D boundary points of both tomography and HEDM volumes can be extracted easily as the input data points and we can apply the same spirit of the image registration to develop new 3D registration scheme by building a unique cost function and a new optimization technique.

With this motivation of the boundary point scheme, we can re-formulate the registration problem in 3D. Given two volumes V_1 and V_2 specified by boundary point coordinates, we develop a cost function χ and an optimization scheme to find the optimal transformation parameter $\mathbf{p}^*$ such that the cost between V_1 and V_2 is minimized as follows

$$\arg\min_{\mathbf{p}} \chi(V_1, \mathbf{p}V_2) \tag{4.1}$$

Now the 3D transformation $\mathbf{p}$ is a combination of a 3D translation and a rotation around z axis. The cost function χ is redefined as sum of squared distances over all points in V_1 to V_2

$$\chi(V_1, V_2) \equiv \sum_{\mathbf{x} \in V_1} d^2(\mathbf{x}, V_2)$$

where the distance between a single point $\mathbf{x}$ and the volume V_2 is defined as the Euclidean distance of $\mathbf{x}$ to its nearest neighbor in V_2, mathematically it is given by

$$d^2(\mathbf{x}, V_2) \equiv (\mathbf{x} - \mathcal{N}(\mathbf{x}; V_2))^2$$

where $\mathcal{N}(\mathbf{x}; V_2)$ denotes a function which finds the nearest neighbor point of $\mathbf{x}$ in V_2. Thus, we can rewrite the cost function between V_1 and V_2 as follows

$$\chi(V_1, V_2) \equiv \sum_{\mathbf{x} \in V_1} (\mathbf{x} - \mathcal{N}(\mathbf{x}; V_2))^2 \tag{4.2}$$

Given the above construction of the cost function, it is easy to picture that the landscape of its cost function is asymptotically parabolic because of the squared of Euclidean distance in the cost function. However, the landscape of its cost function close to the global minimum is generally unknown because this depends on the input data. In the worst case scenario, there might be local minima close to the global minimum, which complicates our parameter search process.

Since the landscape of the cost function is generally parabolic in the large scale while with possible local minima in small scale, we adopt an optimization scheme known as the *Hybrid Monte Carlo*[83] method. The reason to choose hybrid Monte Carlo is motivated from the observation of one drawback of the normal Monte Carlo scheme. The random sampling of points in the parameter space causes the rate of convergence to be proportional to $1/\sqrt{n}$ where n is the number of sampled points. However, due to the parabolic shape of the cost function in the general sense, we have some rough estimation on the local gradient, so a guided sampling is preferred for a much faster convergence speed. And the hybrid Monte Carlo has a stochastic sampling scheme which simulates the evolution of a dynamical system governed by Hamiltonian dynamics, and allows the sampling to vary in a systematic way so as to avoid random walk behavior. More importantly, the hybrid Monte Carlo preserves the ergodicity of the sampling. The time invariance of Hamiltonian system and Liouville's theorem ensure the distribution in phase space is invariant with respect to time; however, to ensure ergodic sampling scheme, a special scheme similar to Gibbs sampling, known as the leapfrog discretization, must be performed.

As for the detailed implementation of hybrid Monte Carlo scheme, the cost function $\chi(V_1, \mathbf{p}V_2)$ is treated as a potential energy term, and the kinetic energy term is given by

$$K(\mathbf{r}) \equiv= \frac{1}{2}||\mathbf{r}||^2$$

where $\mathbf{r} \equiv d\mathbf{p}/dt$ ($\mathbf{p}$ serves as the coordinate in Hamiltonian system, while $\mathbf{r}$ serves as the momentum in Hamiltonian system[1]. The leapfrog scheme is adopted from [83] and modified as follows

$$\begin{aligned} r_i(\tau + \varepsilon/2) &= r_i(\tau) - \frac{\varepsilon}{2}\frac{\partial E}{\partial p_i}(\mathbf{p}(\tau)) \\ p_i(\tau + \varepsilon) &= p_i(\tau) + \varepsilon r_i(\tau + \varepsilon/2) \\ r_i(\tau + \varepsilon) &= r_i(\tau + \varepsilon/2) - \frac{\varepsilon}{2}\frac{\partial E}{\partial p_i}(\mathbf{p}(\tau + \varepsilon)) \end{aligned} \tag{4.3}$$

where $E(\mathbf{r}, \mathbf{p}) = K(\mathbf{r}) + \chi(V_1, \mathbf{p}V_2)$ which is the total energy. It is easy to see that the sampling scheme is guided by the landscape of the cost function because we take the gradient $\partial E/\partial p_i$ for each component of $\mathbf{p}$. Computationally, this gradient is estimated for each step by taking the difference between $E(\mathbf{p} + \Delta\mathbf{p})$ and $E(\mathbf{p})$ and

[1]The notations of $\mathbf{r}$ and $\mathbf{p}$ are reversed as in the classic physics textbooks but we have to adopt that because the notation $\mathbf{p}$ has been used to represent transformation parameters.

then divided by $\Delta\mathbf{p}$. And ε is the step size for leapfrog which controls the length of system evolution. For a desired time of τ, one needs of order τ/ε steps for convergence.

The randomness of this process comes from the random sampling of momentum $\mathbf{r}$ before each time period and a typical Hybrid Monte Carlo consists of s time periods, and each time period is composed of t leapfrog steps, where s and t are specified beforehand. The necessity of sampling $\mathbf{r}$ is because Hybrid Monte Carlo essentially samples the joint distribution of coordinates and momentum. The sufficiency of sampling of momentum independently is because of the independent distributions of $\mathbf{r}$ and $\mathbf{p}$ by our construction of the total energy $E(\mathbf{r}, \mathbf{p}) = K(\mathbf{r}) + \chi(V_1, \mathbf{p}V_2)$ where $\mathbf{r}$ and $\mathbf{p}$ are separable. $\mathbf{r}$ is usually sampled as a multivariate normal distribution because of the availability.

4.2.2 Volumetric Registration between Tomography Volumes

Before applying the general approach of the volumetric registration scheme to the tomography volumes, we must first extract the boundary points for each volume. Generally speaking, these boundary points are retrieved based on the result from Section 3.4.1, where the intensity profile is fitted to an error function, and the value of the transition point, which is the center point of the sigmoid shape, is estimated. Thus this transition point serves as a threshold to segment the whole data set into two groups as well as determining the boundary points.

Two more processes are needed to filter out extra points, for the sake of ensuring a common region, on which the cost function is to be evaluated. The first set of extra points are generated due to the mechanical cutting problem, as we discussed in Section 4.1. The off-axial nature of the cutting makes the two volumes cover different regions of the original sample, so a common region must be first determined and those points which are outside of such common region are filtered out. The second process is to remove the sample boundary in the pin $S1$. Comparing Fig. 4.1(a) and Fig. 4.1(b), the tomography layer of pin $S1$ differs from the one in $S2$ by the extra sample boundary, which should also be removed. Note for the first process, a common region is determined by the parameters from the image registration, which is actually a little bit off, on the order of a couple pixels, from the one retrieved from the volumetric registration.

The elements of the volumetric registration for the tomography volumes is summarized as follows. The transformation is a 3D transformation of the pin $S2$, represented by a tuple containing six parameters (three for 3D translation, two for specifying rotation axis in x-y plane and one for rotation angle) , the cost function $\chi(V_1, V_2)$ as defined as Equation 4.2, and the optimization method is the hybrid Monte Carlo to have guided convergence but we add a final Monte Carlo locally. A hybrid Monte Carlo run stops at a maximal 2000 steps or exits early if satisfying the convergence criterion in which all six parameters change by less than 10^{-3} pixels. Several runs are performed after the 2000 step limit to ensure convergence.

(a) Layer 20 before registration

(b) Layer 20 after registration

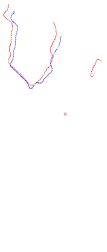

(c) Layer 40 before registration

(d) Layer 40 after registration

(e) Layer 60 before registration

(f) Layer 60 after registration

Figure 4.3: Volumetric registration between tomography volumes of the pins $S1$ and $S2$. The red dots show the boundary points in the pin $S1$ while the blue dots show the boundary points in the pin $S2$. The left column shows overlapping before volumetric registration, while the right column shows the overlapping after the registration, which clearly shows improvements.

Fig. 4.3 shows the comparison between before registration (left column) and after registration (right column) for four representative layers in a particular volumetric registration of 2000 steps. In each subfigure, the red dots shows the boundary points in the pin $S1$ while the blue dots show the boundary points in the pin $S2$. Judging from the before registration subfigures, it is easy to notice the systematic offset by a counter-clockwise rotation and a little bit of shape difference might require a shift in the z-axis. After the volumetric registration, the right column shows much improved overlapping with many features being satisfactorily matched. Some minor features are not explained, for example in Fig. 4.3(f), which may require further adjustment in z axis or might be the artifacts due to the boundary extraction procedure. Of course the optimization of the cost function is a compromise of summation of cost over the whole volume not just the layers shown here.

After the volumetric registration between the two tomography volumes, the two tomography volumes are combined together, where a simple scheme is used. Cubic voxels of one piece take up empty spaces belong to the other piece and if the space is occupied by both pieces, the cubic voxel with higher material density wins that spot. After the combination, it is interesting to quantify the errors. Since the distance to the nearest neighbor is used to measure the cost during the volumetric registration, it is preferred to use an independent indicator to further characterize the error. For this purpose, we decide to study the error of the volumetric registration by *z-height*, which measures heights in z-axis for each boundary points of the volumetric data.

Fig. 4.4(a), 4.4(b) and 4.4(c) show the z-height maps for $S1$, $S2$ and the merged volume, respectively. The z-height map of the merged volume is computed by looking for the location in z-axis where the transition between $S1$ and $S2$ occurs. All the subfigures closely resemble each other, which indicates good agreement. It is also interesting to further characterize the error in the z-height maps, so we plot the difference of each z-height of $S1$ or $S2$ from the deduced fracture surface, determined as the z-height of the merged volume, as shown in Fig. 4.5. The zero difference of the z-heights, colored in green, occupies the majority region for $S1$ which indicates pretty good agreement from the nominal fracture surface while a couple of red pixels indicate discrepancy as large as 10 pixels, corresponding to the high hill in Fig. 4.4(a). One possibility is that this discrepancy results from a loss of the material during the sample fracturing step. For the pin $S2$, the large difference in z-height occurs frequently on the two opposing sides, which indicates a possible tilting of the rotation axis for $S2$. Considering the z-height differences are around eight pixels and the sample is about $500\mu m$ in radius, this tilting is estimated to be $\arctan(8 \times 1.47/500) \approx 1.35^\circ$. Since the average grain cross-section diameter is $\approx 25\mu m$, it is expected that this tilt will have only a minor impact on the characterizations given below. Nevertheless, in a next generation volumetric registration, the tilting will be incorporated and corrected to produce better alignment.

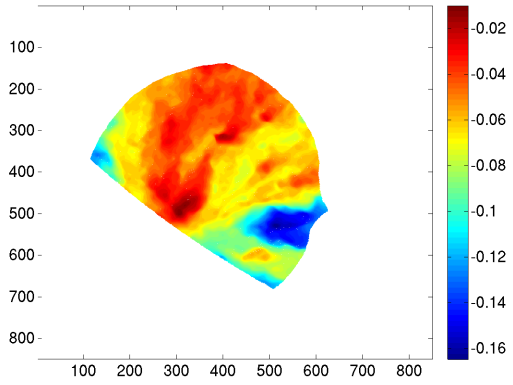

(a) Tomography z-Heights for $S1$

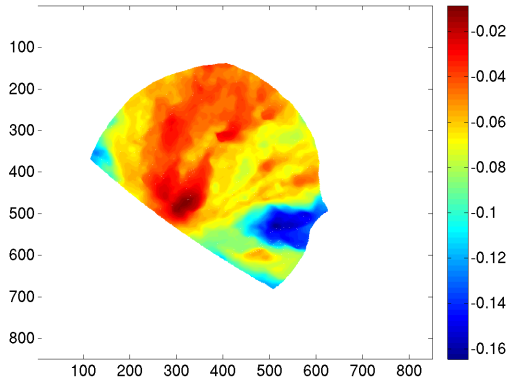

(b) Tomography z-Heights for $S2$

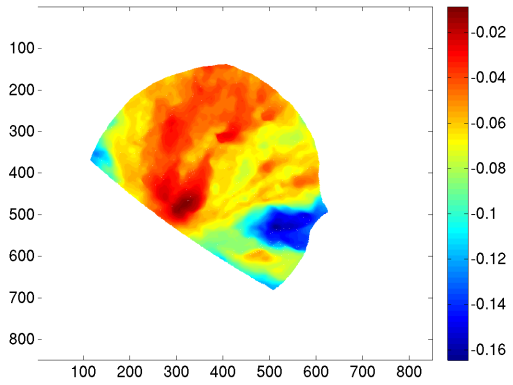

(c) Tomography z-Heights for Merged

Figure 4.4: z-height maps from tomography volumes for (a) $S1$, (b) $S2$ and (c) merged volume. All three height maps are colored based on the z-heights, measured in units of millimeters. Axis labels are in pixels which are $1.47\mu m$ on each side.

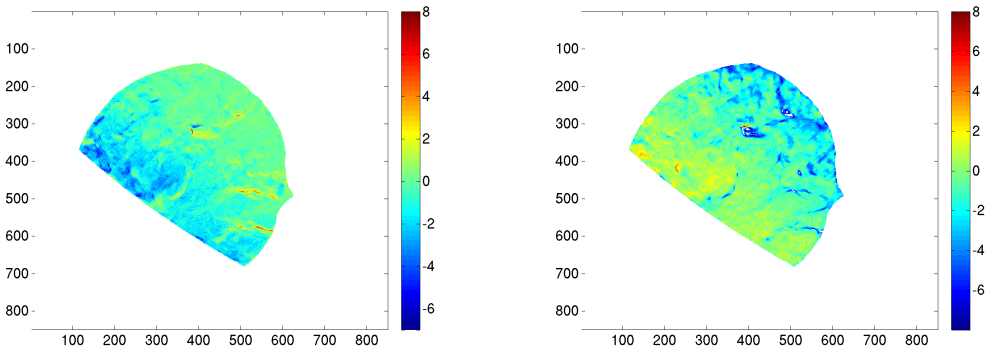

(a) Error of z-Heights for $S1$

(b) Error of z-Heights for $S2$

Figure 4.5: Differences of z-height maps from the nominal fracture surface. (a) for $S1$ and (b) for $S2$. The difference in z-height is in units of pixels (one pixel equals $1.47\mu m$).

4.2.3 Volumetric Registration between Tomography and HEDM Volumes

For the registration of tomography with HEDM volumetric data, in theory, we can adopt the same general approach. However, as we will show, this problem is complicated by the extraction of the boundary points from HEDM volumes, as will be discussed next. Each tomography and HEDM volume is measured and reconstructed in the same x-y coordinate system. Registration then requires only optimizing the z-coordinate of one of the data sets. This is a simple enought problem that we use an exhaustive linear search which guarantees a global minimum.

The second modification is based on the observation that the extraction for HEDM boundary points is not as straightforward as the extraction in the tomography case. To extract the boundary points of HEDM volumes, the confidence maps are a much better candidate than the orientation maps because the confidence on the boundary drops due to few simulated peaks being overlapping with experimental peaks, which gives us some clue on the locations of the boundary. Thus it is tempting to extract the boundary points by enforcing a fixed thresholding, like we did in the tomography case. However, the setting of the threshold can be challenging and is not as straightforward as fitting an error function across the sample edge in the case of tomography data. Thus it is possible to use a threshold to extract the boundary points for the HEDM volumes, but the determination of an appropriate threshold requires further analysis.

To set the confidence threshold, we resort to the general approach of volumetric registration, and we modify the algorithm by incorporating the confidence threshold as a new parameter to be optimized. Thus the optimization problem can be rewritten as follows

$$\arg\min_{\mathbf{p},\chi} \sum_{\mathbf{x}\in V_1} \left[\mathbf{x} - \mathcal{N}(\mathbf{x}; \mathbf{p}V_2(\chi))\right]^2 \tag{4.4}$$

where V_1 represents the set of the boundary points of the tomography volume, $V_2(\chi)$ represents the boundary points of the HEDM volume under the threshold by the confidence level χ and $\mathbf{p}$ is the transform parameter, which is now just a one dimensional shift in z axis. More importantly, the parameter space becomes two dimensional. The optimal parameters can be found by a 2D grid search over a predefined parameter region. The z-axis shift is bounded by the total height of the tomography volume while the confidence level is bounded between $[0.1, 0.7)$.

After performing the 2D parameter search, we can map out the cost landscapes for both pins as a function of z-axis shift and confidence threshold χ, as shown in Fig. 4.6. For both pins, the parameter space covers a 2D grid with z-axis shift ranging from -50 to $+50$ pixels, with the increment of one pixel, and the confidence threshold χ ranging from $\chi = 0.1$ to $\chi = 0.7$ with increment of 0.01. Generally speaking, both landscapes show parabolic shapes and the variation in the z-shift direction is much larger than the confidence threshold level, within the parameter space we choose. This lack of sensitivity allows us flexibility in the choice of confidence level, as long

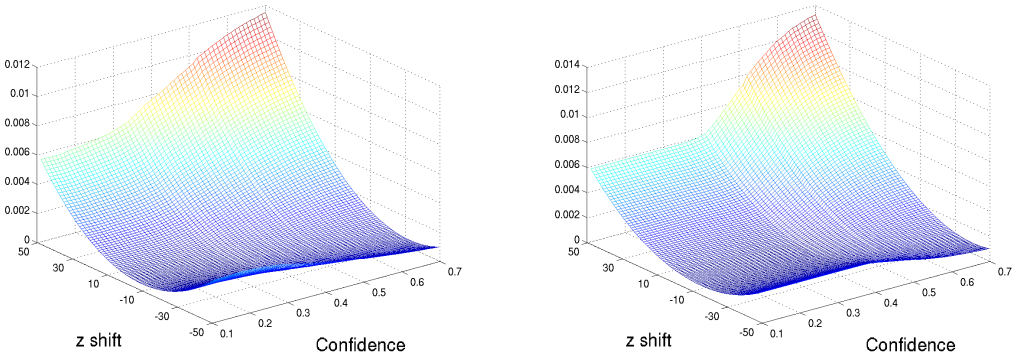

(a) Cost Landscape for $S1$

(b) Cost Landscape for $S2$

Figure 4.6: Cost function landscape of the 2D grid scan for volumetric registration of (a) the pin $S1$ and (b) the pin $S2$. For both subfigures, z-shift axes represents the shift in the z-axis and the unit is in pixels. The confidence axis represents the confidence threshold χ, which ranges from 10% to 70%.

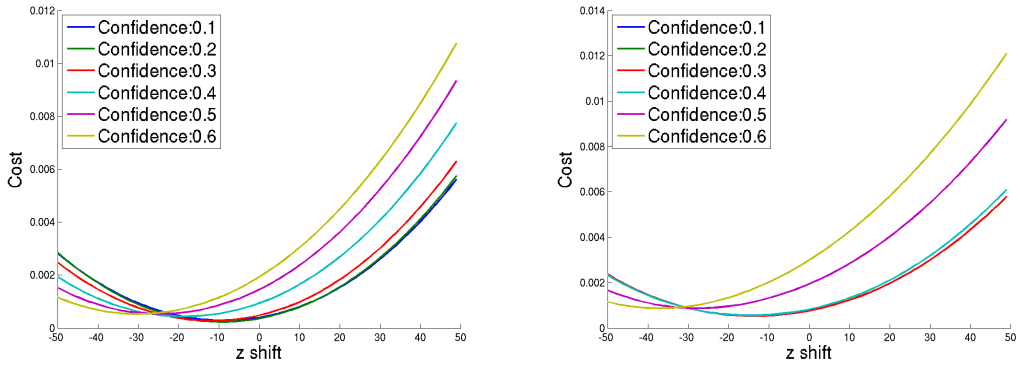

(a) Cost Profile for $S1$

(b) Cost Profile for $S2$

Figure 4.7: Profile plots of cost functions in volumetric registration of the two pins as a function of z-shift. (a) the pin $S1$ and (b) the pin $S2$. For both subfigures, the y axis represents the cost while the x axis represents the z-shift, which is in pixels.

as we can pinpoint the optimal z-shift.

This can be further illustrated in Fig. 4.7, where we plot the confidence measure as a function of z-shift for different confidence thresholds by different colors. All the cost profiles are of parabolic shapes as a function of z-shift, partly because the cost is the sum of squared distances, which has the inherently quadratic form. Furthermore, the position of the minimal cost does not vary as much, typically because confidence is a small factor. Consider a $30\mu m$ grain for example, a 10% confidence threshold drop usually results in a less than $3\mu m$ surface shrink. For both pins, the profile with lower confidence threshold corresponds to larger z-shift, while the profile with higher confidence threshold corresponds to small z-shift. It can be understood that with lower confidence threshold, more material is trimmed away, which forces the matching to translate the HEDM image in z-direction to coincide.

It is again interesting to quantify the error of this volumetric registration by using the z-height as we did for the registration between the tomography volumes, except in this case the difference is taken between the z-height maps of the tomography volume and the HEDM volume. Fig. 4.8(a) and 4.8(b) show the z-height maps for HEDM volumes of $S1$ and $S2$. The z-height maps from the HEDM volumes qualitatively resemble the ones from the tomography volumes (c.f. Fig 4.4). This is mainly because HEDM volumes have larger z-spacing ($4\mu m$) compared with the spacing in the tomography volume ($1.47\mu m$), thus z-height map in the tomography volume has higher resolution. As a side note, $S2$ has a plateau, shown as the dark red region in Fig. 4.8(b). This is because we did not collect data from the very top of $S2$, c.f. Section 3.3.2.

Fig. 4.8(c) and 4.8(d) show the z-height difference map for $S1$ and $S2$ computed from their own tomography z-height maps. Note, in $S2$, tomography layers above

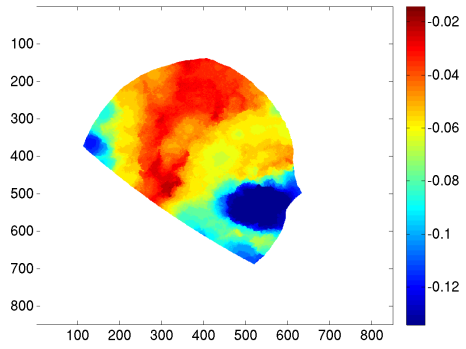

(a) HEDM z-Height Map for $S1$

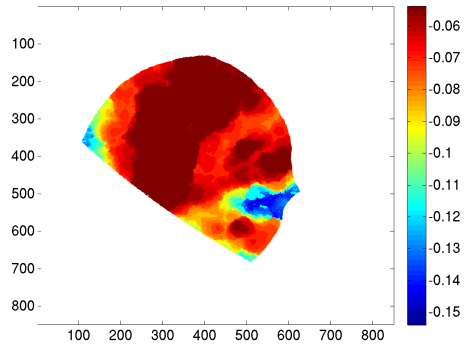

(b) HEDM z-Height Map for $S2$

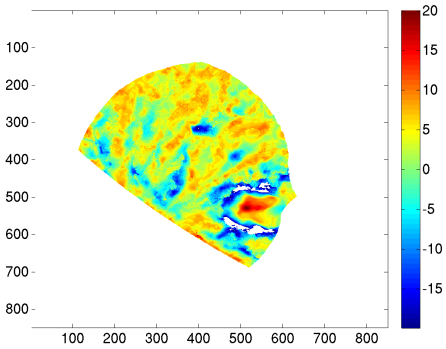

(c) HEDM z-Height Difference Map for $S1$

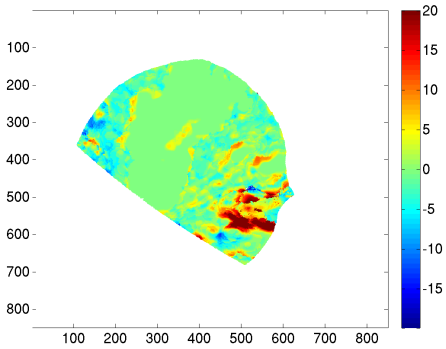

(d) HEDM z-Height Difference Map for $S2$

Figure 4.8: z-height and z-height difference maps for $S1$ and $S2$. (a) and (b) are the z-height maps for HEDM volumes of $S1$ and $S2$ colored by the z-height in millimeters. (c) and (d) are the z-height difference maps from the corresponding tomography z-height maps, which are colored by the difference of z-height in pixels (one pixel equals to $1.47\mu m$).

the top of the first HEDM layers are not considered during the z-height difference calculation, to account for the missing data of the top HEDM layers. Considering the average grain size is around $30\mu m$, the orientation probably changes drastically into another grain's orientation if the z-height is off by more than $30\mu m$, which corresponds to 20 pixels. So in both subfigures, the color scheme has been set to span ± 20 pixels and it indicates pretty large area is in the good agreement, where the offset is less than 10 pixels.

4.2.4 A Final Merge Scheme

The previous two sections discuss the ways to perform (a) volumetric registration between tomography volumes and (b) volumetric registration between tomography and HEDM volumes. Now we can combine all the four volumes to a full data set. This final step, known as merging, is to integrate the two pins, as if it were before the fracture.

Mapping Triangular Mesh Data onto a Square Grid

Before performing the merge, a technical issue here is that HEDM data is reconstructed in a triangular grid while tomography data is generated on square grid, so the merging between them is inconsistent and a unified grid is needed here. Due to the relatively easy manipulation of the square grid, especially for nearest neighbor analysis in later investigation, we convert the triangular grid to the square grid. However, this conversion is not straightforward. For a square area covered by just one triangle, a simple copy of HEDM information is sufficient. However, for a square area covered by several triangles, there is ambiguity. Especially, in our data set, the sizes of the square grid and the triangular grid are comparable, being $1.47\mu m$ and $1.56\mu m$ respectively. Thus it is quite common to have a square grid occupied by multiple equilateral triangles.

The first consideration is whether some smoothing between orientations is needed, i.e. if the square region is covered by several triangles, whether the orientation of the square grid should be the average over all orientations of those triangles. A typical orientation average scheme, which averages in terms of the quaternions of all the orientations, results in an output orientation that is at the center of mass of all the orientations in the quaternion space. This average could be good if all the orientations are very close to each other, since the averaged orientation does not differ too much from each of the orientation cloud of points. However, for cases with totally different orientations, especially at the grain boundaries, this averaging scheme leads to a new orientation that is not even in the original data set. Due to this consideration, we use majority vote scheme. That is the orientation with the largest weight will be the orientation of the square region. Under this scheme, the problem of losing original orientation information is alleviated, however, the only drawback is that the grain boundaries may move, but probably within sub-microns. Since the pixel sizes of the square grid and triangular grid are comparable, the upper limit of this boundary motion is half a pixel because the worst case scenario happens when half of the triangle overlaps with the square pixel due to the majority vote rule. This boundary move can be ignored considering the HEDM's spatial resolution.

The second consideration is how to measure the weight of each original orientation, which is used in the majority vote scheme. An area based weighting scheme, i.e. based on area of each orientation occupied in the new square grid, is theoretically reasonable, however, practically difficult, because coding such algorithm to compute the area

occupied by different triangles is not computationally practical since it requires to consider different scenarios for overlap of the two elements which can be a triangle, quadrangle or pentagonal shape. A more intelligent way is to sample the square region uniformly, say sampling an $n \times n$ grid, where n is the number of points to be sampled in one direction. It is easy to see that if $n \to \infty$, it converges to the area based approach. This algorithm is simpler to write and is probably faster due to the simplified algebra. The only concern is the efficiency to find the right triangle given the coordinates in x and y. In order to solve this, I create a new data structure of the .mic file to reduce the access time to guaranteed constant time (c.f. Section A).

Merging Process

With the uniform sampling and the majority vote scheme, the conversion from the triangular grid to the square grid can be easily done and the merging can proceed. Note during merging, we use the tomography data as a mask while the HEDM information is considered auxiliary. The reason to use tomography material density as a mask is because tomography material density provides much more precise spatial resolution of the material than HEDM.

The actual merging are performed in the following steps. First the tomography volumes are aligned to each other and then merged. Each cubic voxel is assigned to either volume based on the reconstructed material density. Secondly, the HEDM voxels are translated in z direction to the new positions and the orientation and confidence are stored in the merged data structure.

The outcome of the merging process is presented in Chapter 5, together with the characterization of the fracture surface.

4.3 Robustness of Volumetric Registration

The kernel of the volumetric registration scheme is the hybrid Monte Carlo method and it is natural to investigate how robust it is. Recall Section 3.4.1, the material density profile across the sample edge is fitted into an error function. Though the boundary point is picked as the center of fitted error function, the true boundary point is distributed with a FWHM of 2.4 pixels. Thus this uncertainty leads to many other possibilities of the boundary points' locations, each of which deviates from the original position. Thus we are interested in the effect of different deviation of the input data on the output optimal transformation parameters, i.e. characterizing the robustness of the hybrid Monte Carlo, by studying the error bars of all the transformation parameters as well as the sensitivity to input data.

To fully characterize the error bars for each parameter, we introduce a scheme to measure the effect of deviated positions. For each run, we perturb each point (x, y, z) in V_1 and V_2 as follows

$$(x, y, z) \to (x + \Delta x, y + \Delta y, z + \Delta z)$$

where Δx, Δy and Δz are distributed normally as $\mathcal{N}(0, \sigma^2)$ where $\sigma = 2.4$ in pixels. In this sense, V_1 and V_2 are randomized point clouds based on the original data with a small deviation. The same hybrid Monte Carlo scheme is performed to compute the optimal transformation parameters for each randomized set of points. This process is repeated for 2000 times and all the optimal parameters are summarized and the sample standard deviation for each parameter are estimated.

Fig. 4.9 shows the distribution of the transformation parameters for the repeated 2000 perturbations. Each of the subfigures shows a normal-like distribution and the standard errors are summarized in Table 4.1 (note 1 pixel equal to $1.47\mu m$)

Table 4.1: Error bars for transformation parameters in hybrid Monte carlo method.

Parameter	Standard Error
Translation X	$0.0340mm$
Translation Y	$0.0335mm$
Translation Z	$0.0378mm$
Rotation Center X	$0.0612mm$
Rotation Center Y	$0.0602mm$
Rotation Angle	0.0035°

The translation parameter error bars are less than $0.0735mm$ which is 0.05 pixels. The rotation error bar is also negligible in that the motion of a point at the outer radius of the sample would be $500\mu m \times \tan(0.0035^\circ) = 0.0305\mu m$, which is less than the pixel size. Thus it is sufficient to say the hybrid Monte Carlo is robust within the error bars of the input data.

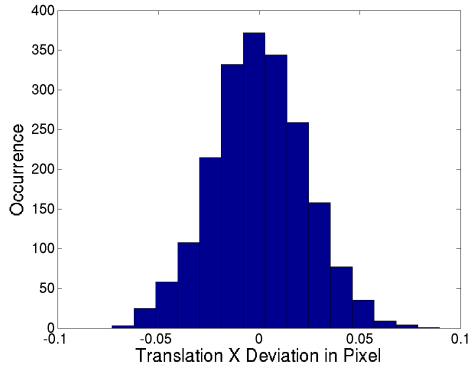

(a) Translation X

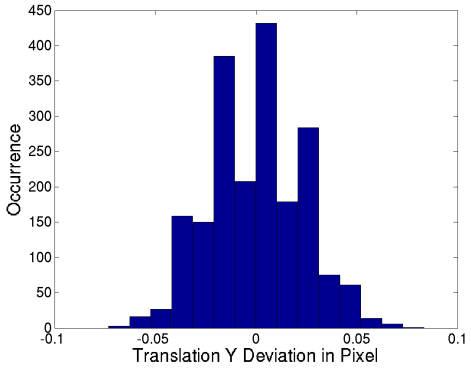

(b) Translation Y

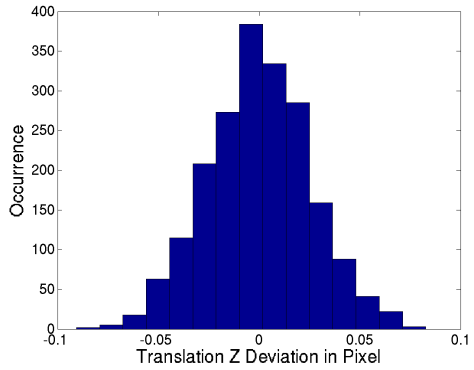

(c) Translation Z

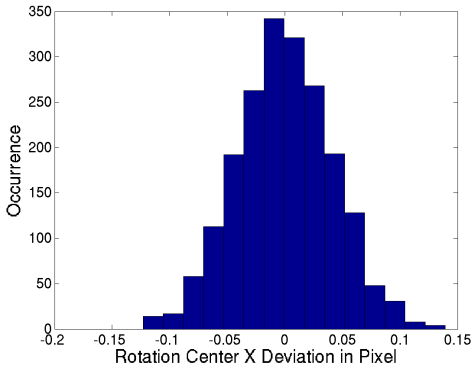

(d) Rotation Center X

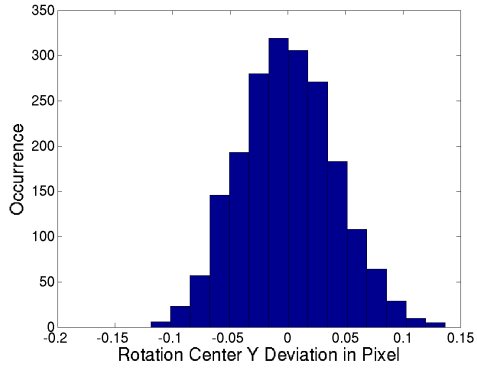

(e) Rotation Center Y

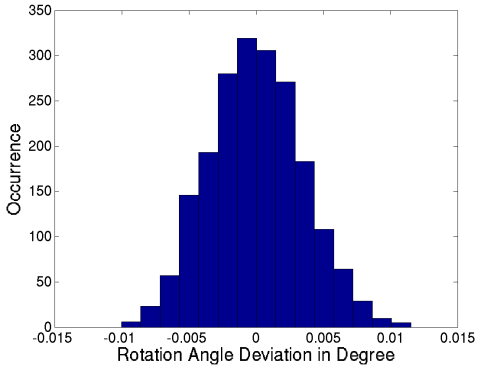

(f) Rotation Angle

Figure 4.9: Histograms for each of the transformation parameters deviated from the optimal solution after repeated 2000 randomized perturbations

Chapter 5

Characterization of the Fracture Surface

Up to this point, our discussion has been focusing on the presentation of our new method which combines HEDM and x-ray tomography and the registration of the four volumetric data sets. We now turn our attention to analyse the aligned data set as a whole. Specifically, we are interested in the *preferred crystallographic direction normal to the fracture surface*, which is an important statistics which gives valuable insight to the crack initiation and propagation mechanisms and it serves as one of the vital outputs for our new method.

The structure of this chapter is following. First we measure the quality of volumetric registration by studying the correlation across the fracture surface. Secondly, we study the local normal estimation by the Principle Component Analysis. Thirdly, the crystallographic directions normal to the fracture surface are extracted based on the local normal estimation and plotted in terms of the modified inverse pole figure. Finally, we discuss the implications of the distribution of the crystallographic normals.

5.1 Correlation across the Fracture Surface

5.1.1 Boundary Correlation Test

The first measure of the quality of registration between the two data sets is to overlap on HEDM confidence maps the fracture surface contour that intersects nominally the same plane. This is motivated from the observation that the reconstructed material density and confidence are expected to drop across the same sample boundary.

Fig. 5.1 shows the confidence maps for four representative layers in the registered and merged volume. The fracture surface contours obtained from tomography are plotted in white in each of the subfigures. The left column of Fig. 5.1 shows the confidence maps of the pin $S1$ overlapped by the fracture surface boundary, while the

middle column shows the confidence maps of the pin $S2$ and the right column shows the merged confidence maps after registration. The usual confidence color scheme is used (red means $\chi = 1$ while blue means $\chi = 0$). It is easy to see that in all subfigures in the left and middle column, the white lines (where the fracture surface lies) are very close to the regions where confidence drops quickly. This indicates high correlation between the tomography boundaries and the HEDM boundaries.

Note that when plotting the left column and middle column, the samples have not been cut to a common region to account for the mechanical cutting problem, because the mechanical cutting problem does not influence the registration within in the same pin. This gives us more area to study the correlation. However, for the right column, the two samples are cut into the same common region because of the mechanical cutting problem, so the shape in the right column is not the addition of the left column and the middle column.

This test is a qualitative approach to quantify the goodness of registration between tomography and HEDM volumes, which serves as a sanity check for the volumetric registration. Not all features are closely matched because the cost function is built to consider all layers instead of only the above four layers and some compromise must be made between all layers.

5.1.2 Intra- (Trans-) versus Inter-granular Fracture

The second measure of the quality of the registration is to study the intra-granularity versus the inter-granularity for grains along the fracture surface. Intra-granularity, also known as trans-granularity, describes one particular fracture that breaks through grains of a material, while the other term, known as the inter-granularity, describes fracture that follows the edges of grains. Fig. 5.2 shows a schematic diagram illustrating the two concepts, where the white gap represents the fracture passing through the sample.

The rule of thumb to distinguish the intra-granularity and inter-granularity is the color between the grains across the boundary. For the intra-granular fracture, the colors of the grains across the fracture surface are the same because by definition the two grains separated by the fracture are originally from the same grain so the colors should be the same. On the other hand, for the inter-granular fracture, the colors are usually different because the inter-granular grains follows grain boundaries so the two grains across the fracture are originally different. This provides us with a quick method to distinguish intra-granularity from inter-granularity.

Fig. 5.3 shows the orientation map of one representative layer after the volumetric registration. Following the fracture surface (denoted by the black line), it is easy to identify several spots where the same color exists across the fracture surface, i.e. intra-granular grains and we present six such spots in insets. However, grains with different colors across the fracture surface, i.e. inter-granular fractures, also exist, and occur quite often.

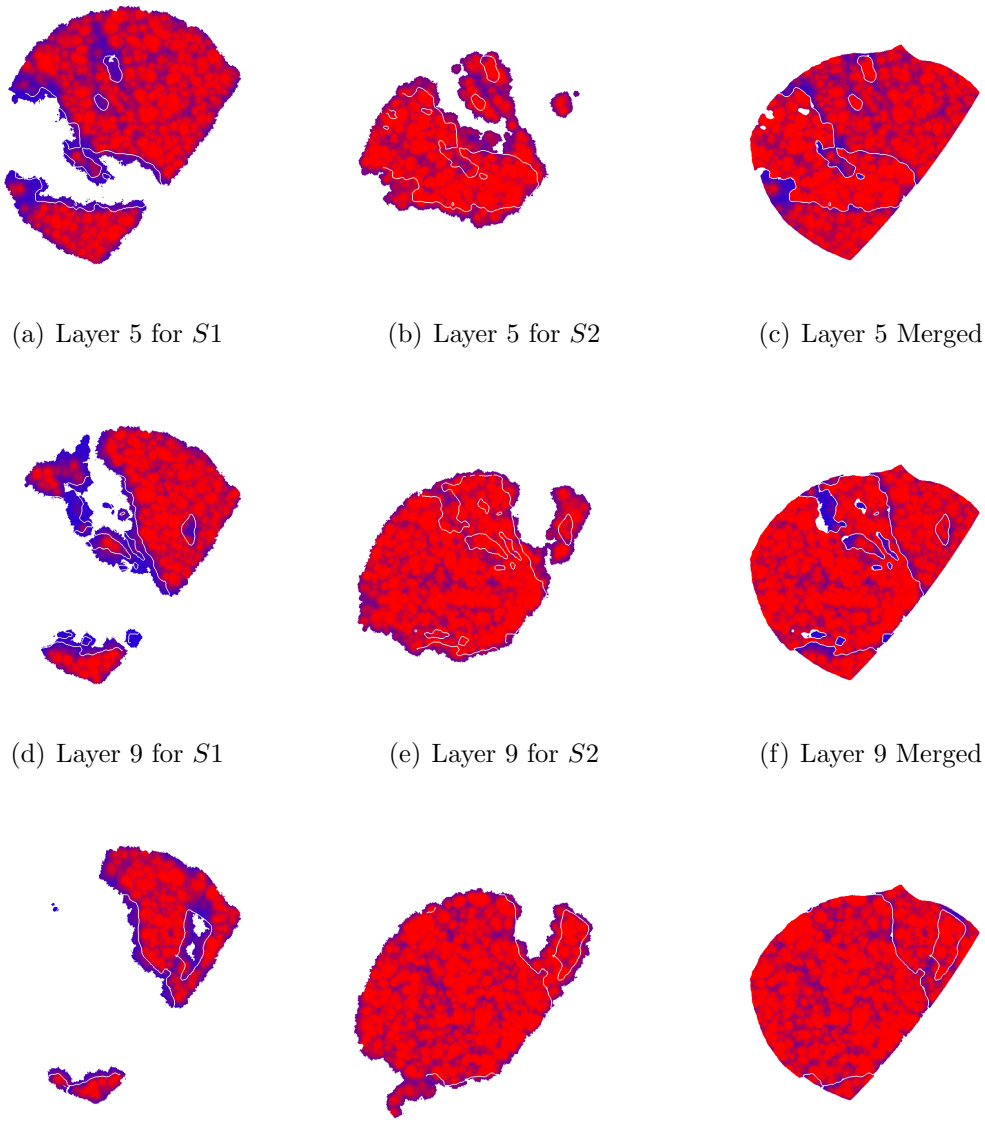

(a) Layer 5 for $S1$ (b) Layer 5 for $S2$ (c) Layer 5 Merged

(d) Layer 9 for $S1$ (e) Layer 9 for $S2$ (f) Layer 9 Merged

(g) Layer 13 for $S1$ (h) Layer 13 for $S2$ (i) Layer 13 Merged

Figure 5.1: Confidence maps for representative layers overlapped with fracture surface lines (in white). The fracture surface lines are determined based on tomography material density information. Each row represents the same layer in the registered volume with first column representing the confidence map for the pin $S1$, middle column representing the confidence map for the pin $S2$ and right column representing the merged confidence map. All confidence in each subfigure ranges from 0 to 1.

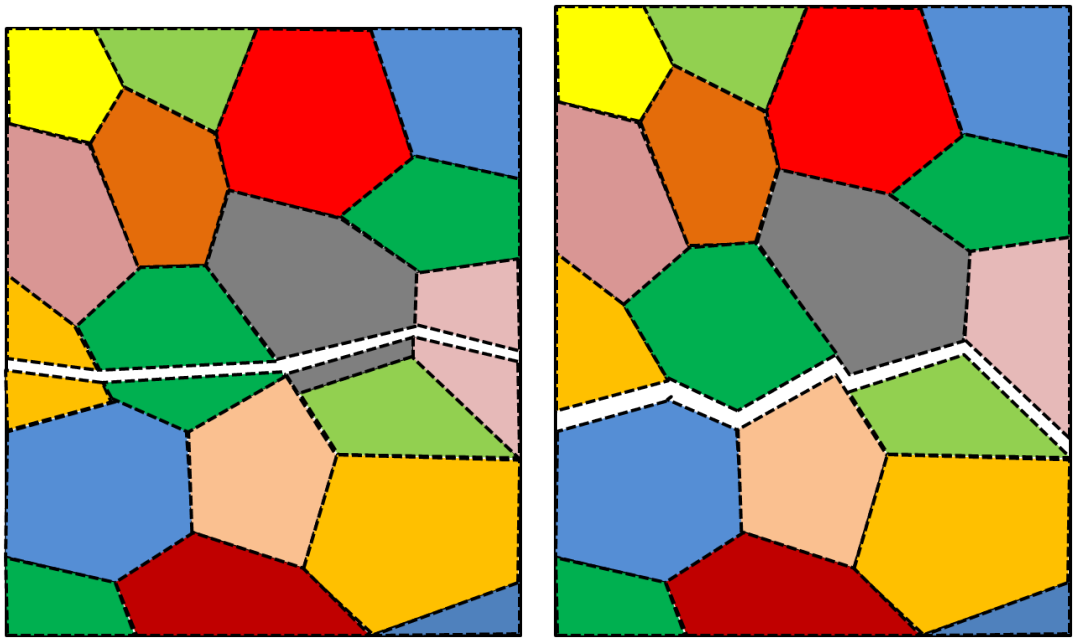

(a) Intra-granularity (b) Inter-granularity

Figure 5.2: Schematic diagram showing intra- and inter-granular fracture surface in (a) and (b) respectively. Schematically, the orientation maps are shown here with each grain represented as a colored patch and the fracture path denoted by the white gap.

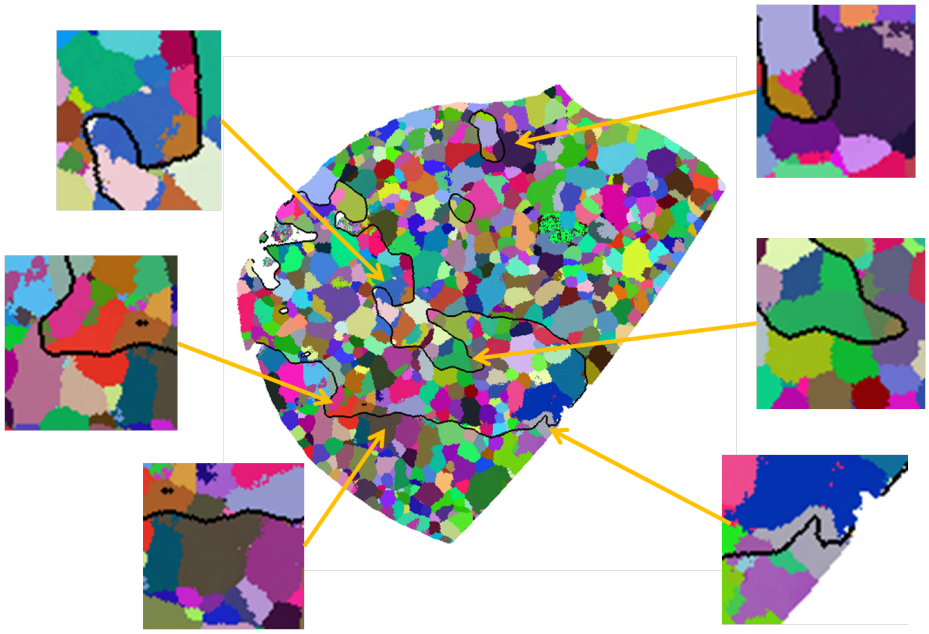

Figure 5.3: Orientation map of a particular microstructure layer with 6 zoom-in local regions which show evidences of intra-granularity within the sample. By the definition of intra-granularity, fracture travels through grains thus orientations across the fracture surface is close, which is reflected by the similar colors across the fracture surface (black line). Note color scheme here is based on the same color scheme used in the orientation map, i.e. using Rodrigues vector mapped to RGB color.

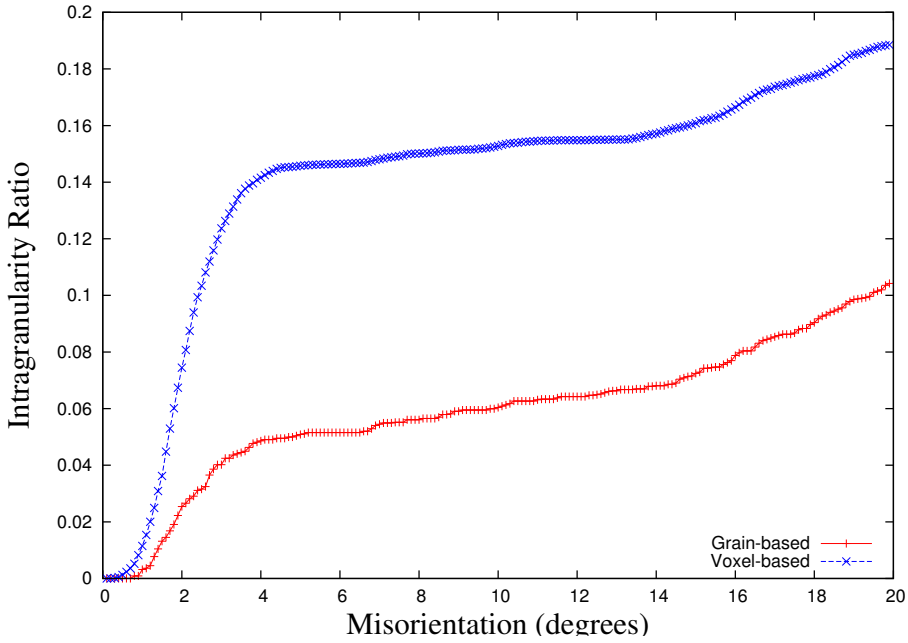

Figure 5.4: Plots of intragranularity ratio as a function of misorientation thresholds (in degree) which defines a grain. Intra-granularity statistics based on grain and voxel are plotted in red and blue respectively. Note this statistics does not incorporate weighting scheme on the misalignment.

The existence of the intra-granular fractures, which is previously reported, strongly indicates the accuracy of the volumetric registration. Furthermore, the shapes of many grains on the fracture surface can be naturally extended to the other side of the fracture surface, which indirectly indicates the accuracy of the registration. However, not all grains across the fracture surface are intra-granular in Fig. 5.3. This may result from the local misalignment of the volumetric registration. As illustrated in Sections 4.2.2 and 4.2.3, the volumetric registration may not be perfect in some local regions. Considering the small grain size in our sample, the misalignment in local region would typically use the orientation in another grain by mistake.

Due to the coexistence of inter- and intra-granular grains, it is interesting to quantify the intra-granularity ratio. We calculate with respect to the whole registered volume, the statistics of the ratio based on two counting schemes. First, we count the total number of intra-granular grains and divide by the total number of grains along the fracture surface. In the second approach, we calculate the fraction of voxels at the fracture surface that have nearest neighbors across the surface with similar orientations.

Fig. 5.4 shows the plots of the two intra-granularity ratios as a function of the misorientation threshold used to define a "grain". The setting of the misorientation threshold determines the definition of the grain, by specifying the maximally allowed

misorientation within the grain and further affects the definition of intra-granularity. The reason to study the two statistics over misorientation threshold is because it gives us a perspective of the misorientation angle distribution for those intra-granular grains. In Fig. 5.4, the two statistics show similar trends with a sharp increase in the region where the threshold ranges from 0° to 4° and shows a plateau region between 4° to 13° misorientation and then further increases after 13°. For all misorientation threshold settings, the voxel-based statistics show higher intra-granularity ratio than the grain-based statistics. Especially, at the plateau region $[4^\circ\ 13^\circ]$, the Intragranularity ratios are approximately 4% and 13% for grain-based and voxel-based statistics respectively. Thus the gap is as large as 10%, which is more than 2 times of the grain-based intra-granularity, thus we expect a great portion of intra-granular grains are large.

The transition to the plateau region is around 4° for the misorientation threshold. However, as we illustrated in Section 3.4.4, the average orientation deviation within a grain for layers is roughly 0.7°. The discrepancy between 0.7° and 4° may be attributed to a couple of reasons. First, deformation is predominant at the fracture surface, so it is possible that the intra-granular grains get rotated during the fracture process. Secondly, since our volumetric registration scheme has not incorporated the tilting and we expect a tilt of about 1° (c.f. Section 4.2.2), it is possible that this 4° threshold may mainly come from the tilting. In this case, this should go away after a next generation volumetric registration.

As mentioned earlier, the small intra-granular ratio may be limited by the local misalignment of the volumetric registration. So we correct this effect by introducing a weighting scheme. Recall we quantified the quality of the volumetric registration in terms of the difference in z-height (c.f. Fig. 4.2.3), from which we know the position that the registration may be wrong. So we introduce an exponential weighting scheme as follows

$$\omega(i,j) = \exp\left(-\frac{\Delta(i,j)}{d}\right) \tag{5.1}$$

where $\omega(m,n)$ denotes the weighting factor of the pixel at ith row and jth column, $\Delta(i,j)$ is the corresponding z-height difference in millimeters, and d is an average grain radius ($12.5\mu m$ in our case). Under this weighting scheme, the intra-granularity ratio is defined as

$$R \equiv \frac{\sum_{i,j} I(i,j)\omega(i,j)}{\sum_{i,j} I(i,j)}$$

where $I(i,j)$ is the indicator function, which is 1 if the voxel on the fracture is intra-granular and is 0 if not.

Fig. 5.5 shows the computed intra-granularity ratio compared with the voxel-based ratio. The weighted intra-granularity ratio displays similar trend as voxel- and grain-based ratios, with a quick growing region in $[0^\circ, 4^\circ]$ and a plateau in $[4^\circ, 13^\circ]$. More importantly, weighted scheme improves the ratio by 5% roughly, which qualitatively indicates intra-granular grains generally follow the fracture where the z-

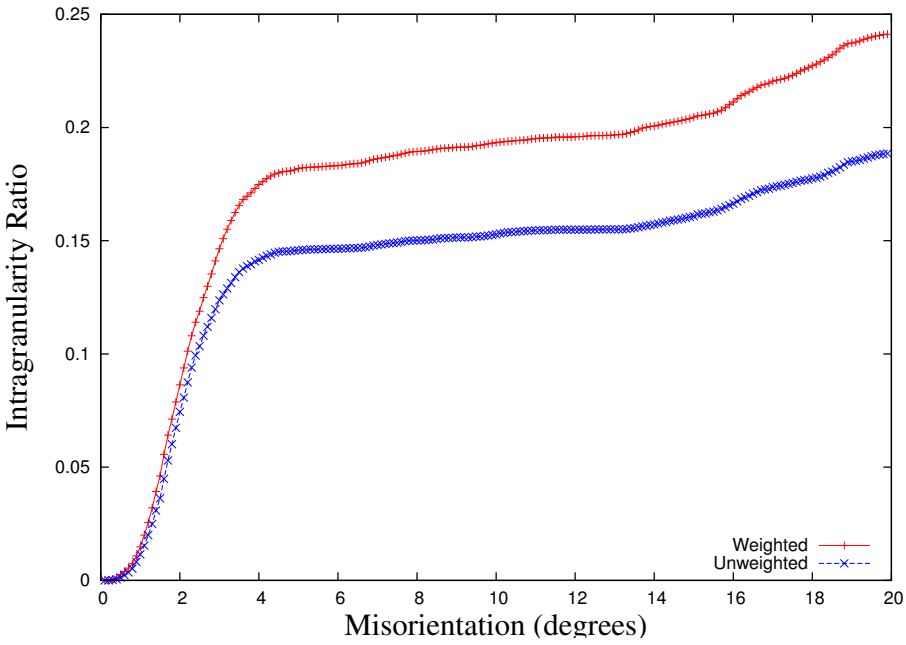

Figure 5.5: Plots of intragranularity ratio as a function of misorientation thresholds (in degree) weighted by the z-height (red, c.f Equation 5.1 for the weighting scheme) compared with unweighted ratio (blue). The unweighted ratio is essentially the intragranularity ratio based on voxels.

differences are small. Though the intra-granular ratio is still low, it qualitatively represents the ratio we saw in Fig. 5.3.

5.2 Local Normal Estimation

To extract the crystallographic directions normal to the fracture surface, we first need to estimate the plane normal locally on the fracture surface, so that later we can convert it into the crystal frame. In this section we discuss the procedure to estimate the local normals. First we will discuss the general scheme we use which is called the principal component analysis. Then we will tailor this method to our problem. Finally we will discuss the distribution of the local normals in the sample frame.

5.2.1 Principle Component Analysis

Principle component analysis (PCA) is a statistical technique to reduce dimension. The general problem PCA solves is to project a set of d-dimensional observations of possibly correlated variables into a new subspace, with lower dimension m ($m < d$), spanned by a set of linearly independent variables (a.k.a principle components)[83]. In our problem, we are given a set of boundary points in 3D coordinate, and we want to approximate a 2D plane. In the PCA's syntax, $m = 3$ while $d = 2$.

To implement PCA, let us consider the general question where we want to approximate a set of d-dimensional data points by a m-dimensional hyperplane, where $m < d$. To best approximate the original data, PCA maximizes the variance of the projected points (or equivalently minimizing the projected distances between the data points and their projections) and it turns out that we only need to approximate the sample covariance matrix which characterizes the correlation between the input data points[83]

$$\mathbf{S} = \frac{1}{N}\sum_{n=1}^{N}(\mathbf{x}_n - \bar{\mathbf{x}})(\mathbf{x}_n - \bar{\mathbf{x}})^T \tag{5.2}$$

where $\bar{\mathbf{x}}$ is the average of the all data points $\mathbf{x}_n$ of dimension d and $\mathbf{S}$ is the data set covariance matrix. Our objective is to find a new set of independent principle components, whose covariance matrix is as close to $\mathbf{S}$ as possible. Note $\mathbf{S}$ is symmetric and real, thus it can be diagonalized and spectrally decomposed into,

$$\mathbf{S} = \sum_{i=1}^{d}\lambda_i \mathbf{u}_i \mathbf{u}_i^T$$

where λ_i is the i-th eigenvalue and $\mathbf{u}_i$ are the corresponding unit eigenvector. Assume eigenvalues are sorted, i.e. $\lambda_1 \geq \lambda_2 \geq \lambda_3 \geq \cdots$, the contribution of each term is decreasing from λ_1 to λ_d. For example, consider a eigenvalue as small as 10^{-6}, which is typical for a 100×100 matrix. If we are only allowed to choose one principle

component to approximate $\mathbf{S}$, choosing the smallest eigenvector would be a bad idea since the resulting new matrix is probably close to the zero matrix. Instead, we should choose the first eigenvector since it has the largest eigenvalue which preserves the most as we can. Similarly, if we are entitled to choose some principle components, we probably want to choose the first few terms and we keep some structure of $\mathbf{S}$ but not all. If we can choose all principle components, essentially we recover all the structure of $\mathbf{S}$, however, the last few terms would introduce negligible contributions at all and practically, around first 10% of eigenvalues are important (c.f. Fig. 12.4 in [83]).

5.2.2 Tailored Method

In our particular problem, we are given a set of boundary points (denoted as $\mathcal{P}$), and for any given boundary point $p \in \mathcal{P}$ we are interested in estimating its local normal, defined as the normal of the plane that is tangential to $\mathcal{P}$ at the point p. The input is the set of x-y-z coordinates and the output is the estimated normals also in x-y-z coordinates.

To estimate the local normal, we use a modified PCA approach. That is, for a particular boundary point, all its neighbors are first identified, then the corresponding covariance matrix is computed as Equation 5.2 and diagonalized to find the eigenvalues and corresponding eigenvectors. However, one twist here is to pick the eigenvector with the smallest eigenvalue, unlike PCA picks the eigenvectors with large eigenvalues. That is because PCA projects to the plane with two large eigenvectors in plane, while we want the normal of that plane which corresponds to the eigenvector with the smallest eigenvalue.

In our modified local normal estimation scheme, it is critical to pick the right neighbors. Specifically, it is natural to ask (a) how many neighbors are to be chosen and (b) what is the criterion to consider one point to be a neighbor.

The first question is generally easy to answer. For our data set, the general rule is to prefer a small number of neighbors rather than large number of them because the latter usually covers a relatively large region and therefore can smooth out small features with a local change in elevation. This can lead to bias towards a plateau plane. The actual choice of number of neighbors will be revealed after we answer the second question.

The answer to the second question is subjective. For example, a typical implementation of `cgal`[1] uses the nearest-neighbor scheme in 3D coordinates. However, in our input data the boundary points are extracted on the uniform x-y grid, thus it makes sense to choose neighbors based on x-y coordinates instead of 3D nearest-neighbor scheme, because the latter turns out to be biased towards a plateau. To illustrate, we demonstrate with a typical example, usually found in our debug process, in Fig. 5.6.

[1] Computational Geometry Algorithms Library, `http://www.cgal.org`

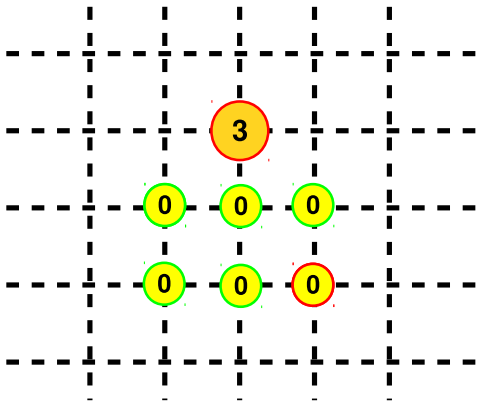

(a) 3D Nearest-Neighbor Scheme

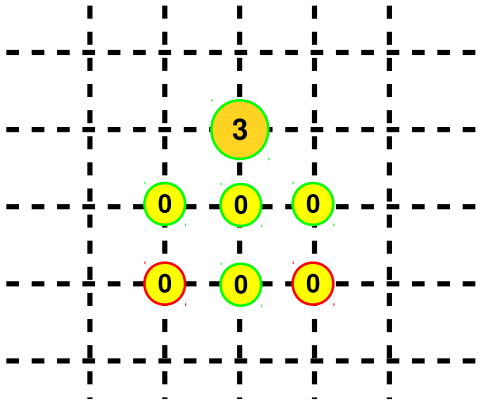

(b) 2D x-y Nearest-Neighbor Scheme

Figure 5.6: Schematic diagram of local estimations using (a) 3D nearest-neighbor scheme and (b) 2D x-y nearest-neighbor scheme. Dotted lines represent the 2D uniform griding of the data points in x and y and several boundary points are shown in circles with their heights noted inside. Circles outlined by green indicate the points being chosen possibly as the neighbors by either algorithm. Circles outlined by gred indicate the points not being chosen.

In this particular example as shown in Fig. 5.6, we estimate the local normal for the data point at the center and more importantly to compare the effects of 3D nearest neighbor and 2D nearest neighbor in x-y axes. Note the number of points to choose is five. Due to the existence of the point at the top with a large height difference of three pixels, there exists a sharp rise locally, so we should at least expect a tilted plane which is not in the x-y plane. However, the nearest neighbor approach (c.f. 5.6(a)) would ignore this large uprise point and choose either one of the two circles in the third row, because either of them is physically closer in 3D to the center circle, which leads to a bias to the plateau estimation and distort the local estimation. On the other hand, the local estimation using the nearest neighbors in x-y plane takes advantages of uniform griding of our boundary points and chooses the uprise data point no matter what the jump is. Clearly, the latter choice yields an improved normal estimation.

After we choose to use the 2D nearest-neighbor scheme, it is natural to choose five neighbors. That is we choose all the nearest neighbors in the x-y plane and the point itself. Including four points in the corners of the 3×3 grid may also be good, however, we choose five since we want to preserve the normal estimation as locally as possible. Larger neighbor numbers lead to additional smoothing but we prefer a level of noise to missing sharp steps in the topology.

5.2.3 Distribution of Local Normals

We now apply the tailored local normal estimation method to our boundary points, computing the local estimation for all boundary points on the fracture surface. Results are visualized in Fig. 5.7.

Fig. 5.7(a) plots the 3D geometry of the fracture in `paraview`[2] colored by height in terms of the pixels. The red color shows the top of the fracture surface and the blue shows the lowest part of the fracture surface. Fig. 5.7(b) shows the x component of the local normal estimations on the fracture surface, with red representing estimated normals facing in the positive x direction and blue representing the estimated local normals facing in the negative x direction. Cross referencing with Fig. 5.7(a), we can see the orange regions in Fig. 5.7(b) indeed correspond to the region facing in x direction in Fig. 5.7(a). A similar result can be found in Fig. 5.7(c). Fig. 5.7(d) shows the z component of the local normal estimation, with a range from 0 to 1 because there are no overhangs that would have the normal pointing down. The z component local normal field is overwhelmingly red indicating that most of the surface has normals along the z-axis.

Though Fig. 5.7 shows only one camera view of the fracture surface, the dominance of the local estimations close to positive z axis is true for all perspectives. To illustrate this point as well as studying the distribution of the each component of the

[2] `http://www.paraview.org/`

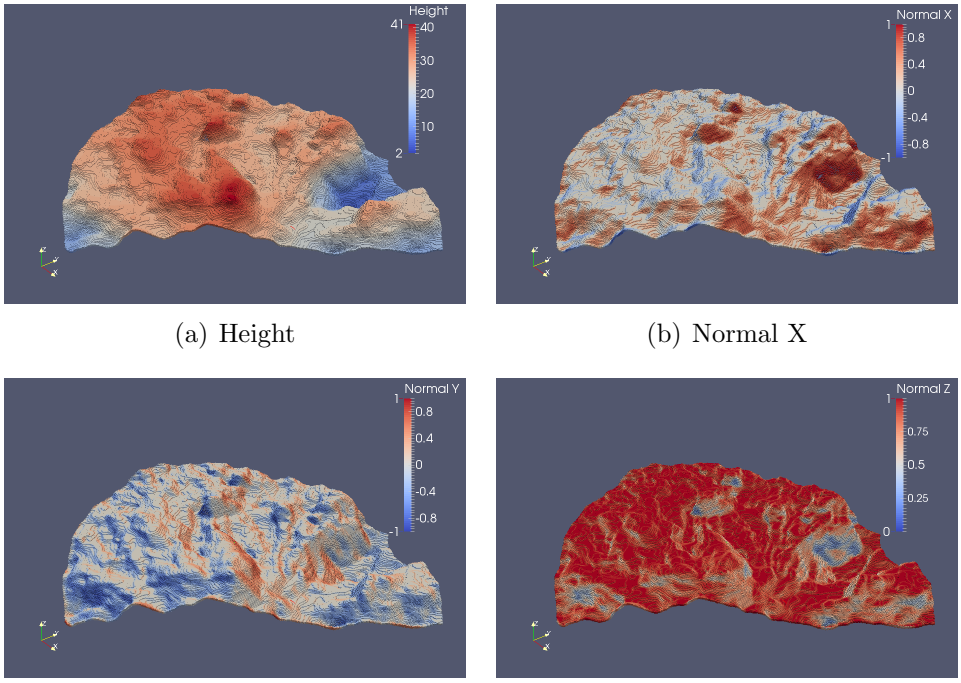

(a) Height (b) Normal X

(c) Normal Y (d) Normal Z

Figure 5.7: 3D visualization of fracture surface in `paraview`. (a) plots the 3D surface as obtained from the merged tomography data set. The color scheme is based on the height above the bottom of the fracture surface in pixels. (b), (c) and (d) plot the x, y and z components of the local normal unit vectors, respectively.

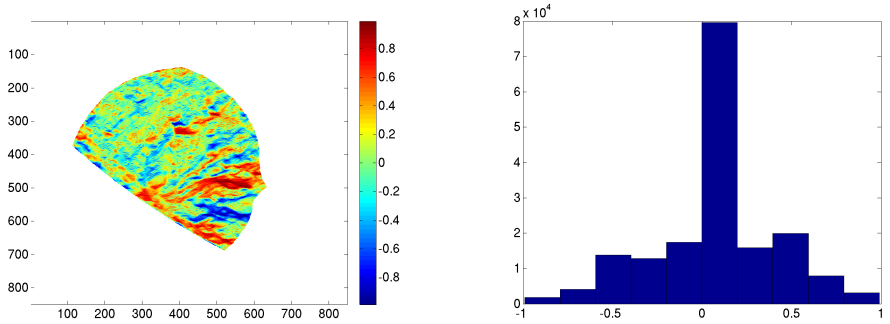

(a) Projection of Normal X

(b) Histogram of Normal X

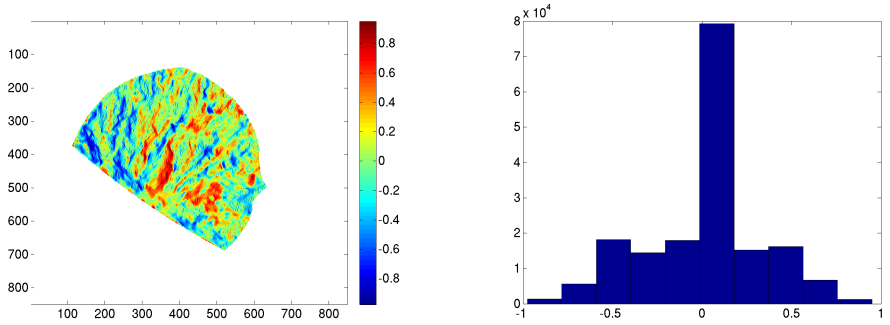

(c) Projection of Normal Y

(d) Histogram of Normal y

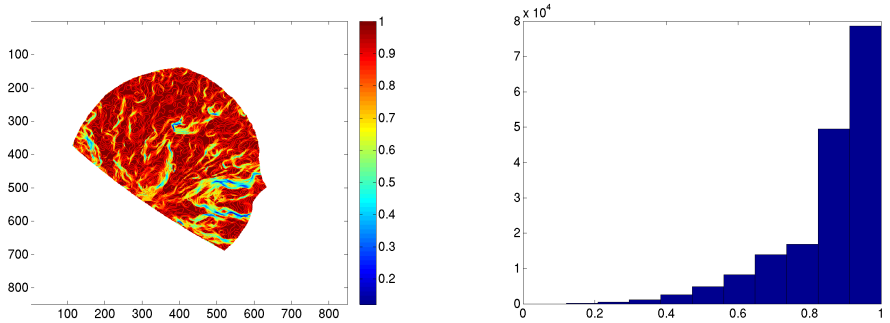

(e) Projection of Normal Z

(f) Histogram of Normal Z

Figure 5.8: Plots for components of local normal estimations. Left column shows the projection of each component of the local normal estimations in 2D. Right column shows the histogram of each component of the local normal estimation.

local normal estimation, we project each component to the $x - y$ plane as shown in Fig. 5.8.

Fig. 5.8(e) shows the dominance of large z components, which is also indicated by the histogram in Fig. 5.8(f). Almost 75% of the voxels have a local normal z component larger than 0.6. This dominance is partially suggested by the distribution

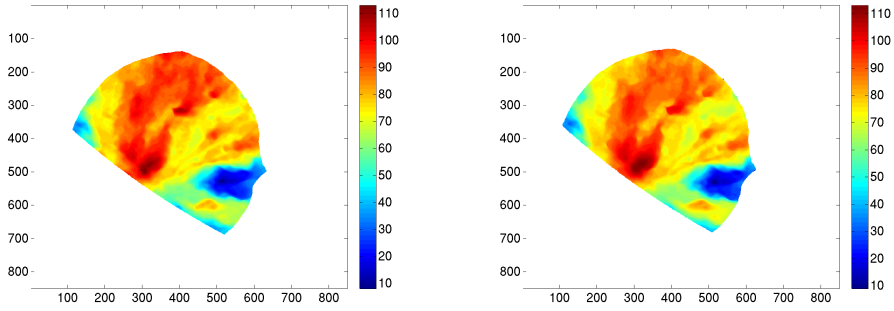

(a) Heights variation in $S1$

(b) Heights variation in $S2$

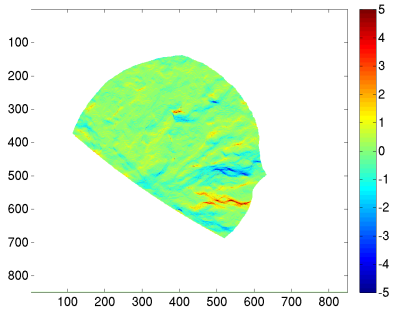

(c) Height gradient in x direction

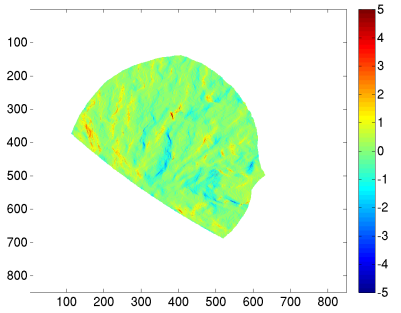

(d) Height gradient in y direction

Figure 5.9: Plots of height variations of the fracture surface. (a) and (b) show the height variations in the pin $S1$ and $S2$ respectively. Coloring is done by the estimated height of the fracture surface where red represents the top while blue represents the bottom. (c) and (d) plot the gradient components in x and y directions respectively, where the gradient is defined as difference in height from the nearest neighbor in either x or y, and the color saturates at 5 and -5.

of the other two components. As shown in Fig. 5.8(a) and 5.8(c), the estimated local x and y components of the normals are mostly close to zero as indicated by the green color and high peaks at zero in the histograms. This dominance in z components suggests most of the normals are facing towards the vertical direction, i.e. the fracture surface is not extremely rough. To illustrate this, we go back to the reconstructed tomography volumes for $S1$ and $S2$ and we focus on the height variation of the fracture surface, because the local normal estimations is actually based on the height field locally.

Fig. 5.9(a) and 5.9(b) show the height variations of the pins $S1$ and $S2$ respectively, and the color scheme is based on the height of the fracture surface above the bottom of the fracture surface. The two figures show almost identical morphologies with very few differences. This indicates accurate reconstructions of the independent

tomography volumes. Though the color scheme indicates large height variations, the local variation is not drastic and some large color patches reflect uniform height plateaus.

A closer look at this issue is gained by plotting the gradient image, which takes the height difference of neighboring pixels. The reason to study local height difference is because such height differences decisively control the local normal estimation. If the drastic local height difference is rare, we would expect such dominance in z component, even the normal estimation algorithm favors local changes. Fig. 5.9(c) and 5.9(d) plots such gradient images with difference in the x and y directions respectively and colored by the height difference in the range from -5 to 5. In both plots, the height differences are mostly zero, as indicated by the majority area of green color. This justifies that the local normals are mostly close to the z axis.

5.3 Distribution of Crystallographic Directions Normal to the Fracture Surface

We are now ready to calculate the crystallographic directions normal to the fracture surface for each element or voxel since we have computed the local normal field. The local normals, $\mathbf{v}_s$, are determined in the sample reference frame. To determine the crystallographic directions that point along these normals, we simply transform to the local crystal frame

$$\mathbf{v}_c = \mathbf{R}\mathbf{v}_s$$

where $\mathbf{v_c}$ represents the local normal vector in the crystal frame. Though it is generally difficult to quantify and visualize a 3D vector like $\mathbf{v}_c$, we can borrow the idea from materials science which uses the *pole figure* or *inverse pole figure* to characterize distribution of a 3D vector. However, while the distribution of $\mathbf{v}_c$ is close to an inverse pole figure plot, it is not exactly the same. Thus, in this section we will first discuss the definition of inverse pole figure and the modification so that we can plot the distribution of the crystallographic directions normal to the fracture surface in a similar fashion. We then present the distribution of the crystallographic normals and discuss the implications.

5.3.1 Modified Inverse Pole Figure

As in Section 3.4.3, we used inverse pole figure to quantify the orientation distribution along a particular sample direction. However, for our problem here, we are not interested the distribution in a particular direction in sample frame. Instead, we are interested in the local normal direction in the sample frame for each voxel on the fracture surface. We compute the distribution of such directions in the crystal frame. This close similarity to the inverse pole figure allows us to utilize the inverse pole

figure to generate the plots for our purpose, but we need to modify the procedure for computing the input data for such plots.

For a typical inverse pole figure, the direction of interest in the sample frame is given first and converted to the directions in the crystal frame. In theory, one could project stereographically all those unit directions in the crystal frame, which are on a hemisphere, to a plane on the north pole with a projection origin at the south pole. However, due to computational considerations, it is wise to compute the orientation distribution first by smoothing and then do the stereographic projection. For a cubic sample, the symmetry operators leads to 24 equivalent regions on the projection plane, so the usual practice is to pick a particular quasi-triangular slice which contains three corners, with {001} being on the left, {110} being on the right and {111} being on the top.

A typical implementation of inverse pole figure can be found in `mtex`. Nevertheless, as mentioned previously, the sample directions of interest are not limited to one particular direction for our problem, so such implementation in `mtex` is modified for our need. This is because when `mtex` makes the inverse pole figure plot for a particular pole, it requires a list of orientations in the Euler angle representation as the input. For our problem, since the crystallographic directions normal to the fracture surface $\mathbf{v}_c$ are calculated, we need to convert them to corresponding orientations to fit the `mtex`'s input format.

To compute the corresponding orientation R, given $\mathbf{v}_c$ and $\mathbf{v}_s$, it is important to note that there are infinite number of orientations that transform $\mathbf{v}_s$ to $\mathbf{v}_c$. That is because, from the axis-angle representation, we can choose infinite number of axes, which forms a plane bisects $\mathbf{v}_s$ and $\mathbf{v}_c$. Since we only need one orientation here, we pick the axis to be the cross product of $\mathbf{v}_s$ and $\mathbf{v}_c$ and the angle to be the angle between them.

Particularly, we choose the (001) direction for the crystallographic normals to convert to and make the inverse pole figure along the (001) direction. So the later plots indicate the inverse pole figure plots along (001) direction. They are actually along the local normals on fracture surface.

5.3.2 Preferred Crystallographic Directions Normal to the Fracture Surface

With `mtex`, the distribution of the crystallographic normals for the voxels on the fracture surface can be plotted in terms of the modified inverse pole figures. And the plotting of the modified inverse pole figure adopts the same convention as the ordinary inverse pole figure. The color scheme is scaled with respect to the distribution of multiples of a random distribution (MRD). By definition, MRD is the distribution of a totally randomly oriented sample. And when plotting the inverse pole figure, the actual intensity of the sample of interest is scaled by dividing by the intensity of the MRD distribution. So the region with high intensity indicates a distribution density

much different from random distribution, i.e. a preferred crystallographic direction normal to the fracture surface.

In this section, we will discuss the distributions of the crystallographic normals for three categories: all voxels, the intra-granular voxels and the inter-granular voxels on the fracture surface.

Distribution for All Voxels

First we plot the distributions of the normals to the fracture surface for all voxels on the fracture surface as shown in Fig. 5.10(a) and 5.10(b). The distributions differ mainly in the $\{111\}$ population where $S1$ displays an intensity of 1 while $S2$ displays an intensity of 1.16. However, the intensities of $\{001\}$ do not differ too much, with $S1$ being 1.16 while $S2$ with 1.1, though the latter is not immediately apparent in the figure due to the broadened color scale.

Distribution for Intra-granular Voxels

Second we take a look at the distribution of the crystallographic normals for the intra-granular voxels. Fig. 5.10(c) and 5.10(d) plots the distributions for the pin $S1$ and $S2$ respectively. These figures are almost the same in that they share the same minimal intensity 0.79 as shown in the left corner and their maximal intensities, shown on the top of the slice, are almost the same, being 1.29, 1.33 respectively. There is a preferred normal in the $\{111\}$ direction. This agreement of the distributions of the crystallographic normal directions for intra-granular voxels is expected because, for the intra-granular voxels across the fracture surface, the misorientation angle is by definition less than 2°, and the normal estimations are the same.

Distribution for Inter-granular Voxels

It is also interesting to study the distribution of the crystallographic directions normal to the fracture surface for inter-granular voxels. Fig. 5.10(e) and 5.10(f) shows the distributions for the pin $S1$ and $S2$ respectively. Both of them show a drastic difference from the intra-granular case since they reflect a dominant peak on $\{001\}$. However, the inter-granular voxels in $S2$ do display another peak in $\{111\}$ with intensity 1.1 while for the other pin $S1$, the intensity is 1.0. This discrepancy may come from the statistical fluctuation and these two distributions are similar, qualitatively speaking .

5.3.3 Discussion

In this section, we discuss the implications of the distribution of the preferred crystallographic directions normal to the fracture surface seen in Fig. 5.10.

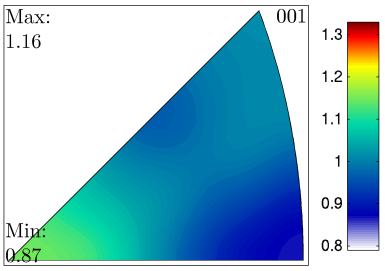

(a) Modified inverse pole figure for all voxels in $S1$

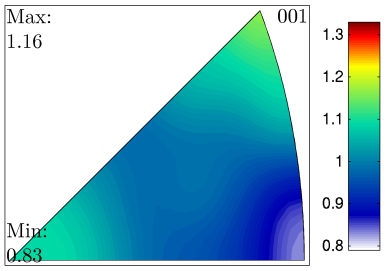

(b) Modified inverse pole figure for all voxels in $S2$

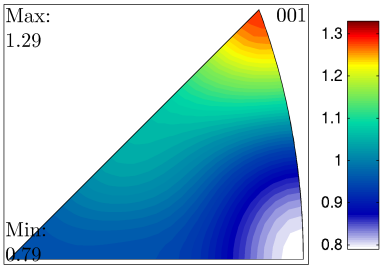

(c) Modified inverse pole figure for intra-granular voxels in $S1$

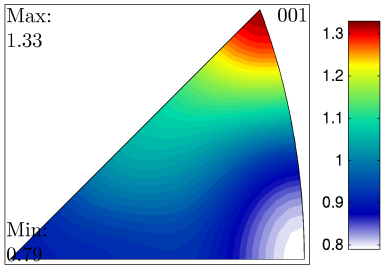

(d) Modified inverse pole figure for intra-granular voxels in $S2$

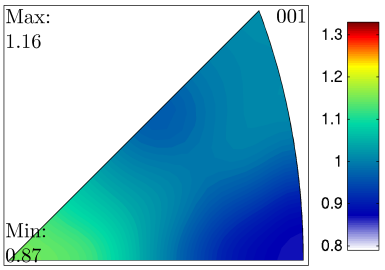

(e) Modified inverse pole figure for inter-granular voxels in $S1$

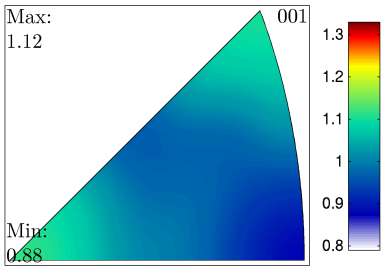

(f) Modified inverse pole figure for inter-granular voxels in $S2$

Figure 5.10: Modified inverse pole figures for the distribution of the crystallographic directions normal to the fracture surface from $S1$ and $S2$ respectively in (a) and (b) all voxels. (c) and (d) intra-granular voxels. (e) and (f) inter-granular voxels. The color schemes for all subfigures are scaled between the maximal intensity 1.33 in red and the minimal intensity 0.79 in white. In each subfigure, the three corners represent different crystallographic directions. The upper corner represents the {111}, the left corner represents the {001} and the right corner represents the {110}.

Volumetric Texture

Based on Fig. 5.10, it may be tempting to draw the conclusion that the {111} crystallographic directions normal to the fracture surface is more likely to lead to intra-granular fracture for our sample, while {001} grain boundary tends to result in inter-granular fracture. However, more needs to be considered to rule out any potential influencing factors. For example, as we discussed in Section 5.2.3, the majority of the estimated local normals are close to the positive z axis. It is necessary to consider the influence of the volumetric texture from the sample.

As mentioned in Section 3.4.3, our sample displays texture, that is a preferred {111} crystal direction near the sample z-direction. Given the fact that local normal estimation on the fracture surface is dominated by the (001) sample direction, it is easy to see that the distribution of the normals of the intra-granular voxels is biased towards {111}. In fact, the maximal intensity of the volumetric normals at {111} is 1.74 while it is only 1.31 for the intra-granular voxels. So it is possible that the actual intensity of the {111} normals for the intra-granular voxels is less than 1, but it gets increased due to the dominance of the {111} texture along the same z-direction in the volume.

On the other hand, the distribution for the inter-granualar voxels is not influenced by the volumetric texture at all because the peak dominates at {001} instead of {111}. So it is safe to claim that the inter-granular fracture tends to follow the {001}.

Deformation Mode

As mentioned in Section 1.2, the Rene88DT is susceptible to {111} slip. The physics behind this is that Rene88DT is a face-center-cubic (FCC) structure and slips often occur along the most closely packed plane. In FCC, the most closely packed plane is the {111}. So it is understandable that under cyclic loading, deformation usually occurs inside a particular grain that the closely packed crystal planes, due to their strong bonding within the plane, slips like a deck of cards. Such plastic deformation is irreversible leading to permanent dislocation accumulate and finally results in crack initiation.

As for the inter-granular voxels, the story is a little bit different, since by definition inter-granular fracture follows along grain boundaries. As mentioned by Luo et al.[34] and Li et al.[31], the actual choice of crack propagating along 111 or 100 depends on various factors like crack-tip intensity factor range[34, 84] as well as temperature and crack propagation rate[34]. This possibly explains the double peaks in Fig. 5.10(f).

5.4 Distribution of Crystallographic Directions Normal to the Fracture Surface on Facets

In the previous section, we study the distribution of the crystallographic directions normal to the fracture surface on the whole fracture surface. However, since our technique is quite recent, no comparable experimental results are found to compare directly with our results. As mentioned in Section 1.2, the current state-of-the-art techniques only allow for measurements of relatively large areas, known as the facets on the fracture surface, which contains a partial information of the whole picture. For example, Miao[35] studies crystallographic normals of 20 facets of a fractured Rene88DT sample by using the standard SEM-based techniques. Though his paper definitely indicates all crystallographic directions normal to the fracture surface of the 20 facets are close to the $\{111\}$ crystal directions, this relatively small data set incurs suspicion regarding statistical significance.

Since our data set contains a full distribution of crystal orientations, it also includes the distribution regarding facets. So in this section, we will present the way to extract the distribution of the crystallographic directions normal to the fracture surface on facets and compare our result with the result from the independent SEM-based techniques. Specifically, we will directly compare with Miao[35]'s result.

5.4.1 Procedure

To extract the distribution of the normals of facets, we need to find a way to determine the facet. A facet on the fracture surface corresponds to a planar surface region so ideally the local normal on that facet is the same at every location. Practically, the local normals of a facet may vary due to the error in the tomography reconstruction (c.f Section 3.4.1). So we define a facet by setting a subjective angle threshold of 2° on the local normals. That is neighboring voxels whose local normals differ by a larger than 2° angle are considered as in different facets. Under this definition, voxels are grouped into different facets.

Assuming Miao[35] collects information for 20 big facets, we sort the facets by the number of voxels each facet contains and pick the biggest 20 facets. Miao[35] also constrained the angle between the facet normal and the loading direction within $[35^\circ, 65^\circ]$. Though no explanation is given on this point, it is quite possibly because he used EBSD, which introduces constraints on the measurement, as Prof. Anthony Rollett pointed out.

Finally, all voxels' crystallographic directions normal to the fracture surface on the 20 largest facets are computed by transforming the local normal estimation with the orientation information.

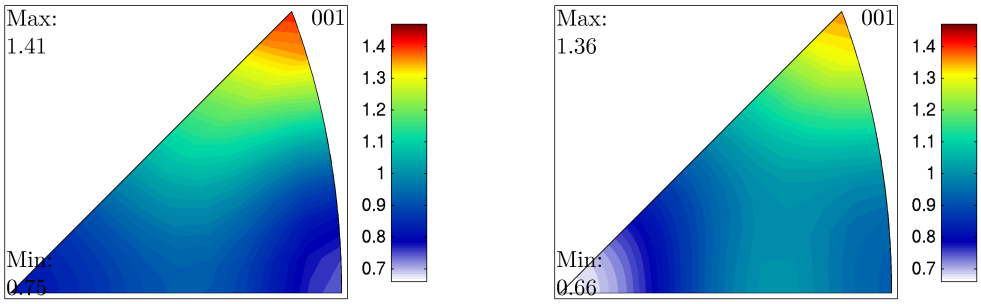

(a) Facets Orientation Distribution for $S1$ (b) Facets Orientation Distribution for $S2$

Figure 5.11: Distribution of crystallographic directions normal to the fracture surface on the 20 largest facets for (a) $S1$ (b) $S2$. Both subfigures are plotted in terms of the modified inverse pole figure. The left corner represents $\{001\}$, the right corner represents $\{110\}$ while the upper corner represents $\{111\}$. And color is scaled between 1.41 (red) and 0.66 (white).

5.4.2 Results

After applying the $[35°, 65°]$ angle constraint, we further filter out small facets (facets less than 10 voxels are ignored) and a total of 208 facets are left as our candidates, which contains 4212 voxels in total. The largest 20 facets are chosen, which has 1106 voxels and the crystallographic directions normal to the fracture surface for these orientations are computed for the pins $S1$ and $S2$.

Fig. 5.11 shows the distributions of the crystallographic directions normal to the fracture surface on the facets for the pins $S1$ and $S2$ respectively. Both of them clearly show a peak around $\{111\}$ which coincides with Miao[35]'s report. This is a reassuring result and it strongly demonstrates the powerfulness of our new method. Besides this, our technique provides much more detailed and more statistically significant information.

Chapter 6

Initiation Site Prediction and Verification by FFT Plasticity Model

In Chapter 5 we discussed the preferred crystallographic directions normal to the fracture surface, which investigates the distribution of crystallographic properties on the fracture surface mainly in the fracture growth and propagation stages in the fracture surface's lifetime. In this chapter, we turn our attention to study of another important stage of the fracture's lifetime, which is the *fracture initiation*. Particularly, we are interested to study the location of the initiation site of our fracture surface and compare it with the predicted initiation site by a fracture simulation model.

This chapter is structured as follows. We start with brief introduction to the study of initiation sites of fracture surfaces in Section 6.1. We review literature on the fracture initialization mechanisms and motivate our interest in a computational model. In Section 6.2, we present a particular plasticity deformation model known as the Fast Fourier Transform based Viscoplastic (VPFFT) model, which can simulate plastic strain and stress fields under the cyclic loading condition. Then in Section 6.3 we utilize the VPFFT model for strain rate simulation on our fracture surface data set and correlate the predicted high strain location with the experimentally determined initiation site. The purpose of this exercise is to 1) see if the model can correctly locate an initiation site and 2) to demonstrate the direct comparisons that can be made between HEDM data sets and computational models of materials evolution.

6.1 Introduction

6.1.1 Fracture Mechanisms

The study of the fracture mechanisms is an interesting and important field because it uncovers the principles of fracture initiation, growth and propagation under ex-

ternally applied loads under a variety of environmental conditions. It provides more detailed understanding about material's mechanical properties and gives invaluable insights into increasing resistance to reversible and irreversible deformation. Such understanding has the potential to help make materials that are more robust that elongated service life. On the other hand, the study of fracture mechanisms is also challenging, because of its difficult nature. The understanding requires not only theoretical models but also abundant related experimental data as well as other factors, like material's mechanical nature, loading history and experimental ambient conditions.

From an engineering perspective, the lifetime under fatigue and fracture conditions can roughly be categorized into three stages[85]: crack initiation, stable crack propagation and unstable crack propagation. In this chapter we focus on the first stage by locating the presumed crack initiation site and testing the ability of a computational model to reproduce high strain behavior at that site. There are three candidate mechanisms for explaining crack initiation

- Void nucleation
- Second phase particles
- Plastic deformation

Note that these mechanisms do not have clear boundaries between one another. In reality, some material undergoing crack initiation may experience a sequence of complicated processes which may be attributed to multiple mechanisms. For example, a void may form from second phase particles or plastic deformation or the existence of the voids or second phase particles may result in plastic deformation or other ways around. However, we will try to clarify each of the above mechanisms as individually as possible. We will also briefly discuss mechanisms of the crack propagation.

Firstly, void nucleation is the first stage of a process that is followed by void growth and coalescence in ductile fracture of metals[86]. As mentioned earlier, voids may possibly come from hard second phase particles[87] or non-metallic inclusions, as well as from plastic deformation[88]. In the case of particle induced voiding, voids usually initiate at the interface between the particle and matrix[89, 90]. Besides the second phase particles and plastic deformation, cavities may nucleate at grain boundaries[91]. For example, Hull and Rimmer report an inter-granular fracture resulting from the growth of voids along grain boundaries for a polycrystalline copper wire at the temperature range 400° to 500° and a theory based on diffusion controlled void growth is suggested.[92]

Secondly, as for the second phase particles, it influences the fracture initiation through the deformation[93]. Because a hard second phase particle does not deform much as compared with the matrix material, then the matrix material close to the second phase particle deforms more than the other material. This leads to a higher strain state which initiates the fracture. Furthermore, the size of the second phase

particles plays a vital role in the fracture initiation. If the size of the particle is comparable to the size of the dislocation or the slip band spacing, the dislocation effect is much pronounced in the fracture initiation[88], while if the size of the particle is much larger than the size of dislocation of the slip band spacing, the plastic strain and stress effect takes over. However, Flom and Arsenault[94] investigate the role of particle size on the fracture process by studying SiC particles in the SiC/Al composites and find the particle size does not influence the crack initiation toughness (material's ability to resist fracture) while it influence crack growth fracture toughness. On the other hand, a second phase particle can also play a role in forming the voids, as long as it satisfies certain conditions, as Argon and Safoglu suggested[95].

Thirdly, for plastic deformation, different modes can lead to the initiation of the fracture, especially, local slip and twinning. For example, Mughrabi et al.[96] model the crack initiation in a high-cycle fatigue under a dislocation mechanism to study the cyclic slip mode. They find that fracture initiates at the regions of the cyclic strain localization in persistent slip bands. Usually, the fracture initiation sites correspond to regions with high strain rate and stress. Ritchie et al.[97, 98] propose a critical fracture stress and fracture strain models which sets a threshold of the fracture strain for fracture initiation. Norris et al.[99] propose a computer simulation model for fracture initiation and propagation based on a plastic strain model where fracture initiates when the mean stress exceeds a critical value over a critical length (this simulation model serves as a predecessor of the VPFFT model as we will present as follows).

6.1.2 Motivation

In the previous section, we reviewed some literature with respect to the current state-of-art fracture mechanisms especially for those on fracture initiation. Our aligned and merged data set serves as a unique observation that can be used to test the hypotheses of previous theories and proposed mechanisms. Our fracture surface data set not only contains precise location of the fracture surface but also the orientation field information and local normal estimation on the fracture surface. However, considering that some of the above hypotheses are built for different materials with different material properties from our sample, we limit our focus to several small topics. In this chapter, we test against a general hypothesis, which correlates the initiation site with high stress/strain locations, i.e. the high stress/strain location under plastic deformation induces the initiation site (for Rene88DT sample).

The choice of such hypothesis is motivated by two fundamental reasons. First, many simulation schemes have been invented to model plastic deformation, based on models built on theoretical hypotheses and experimental observations, so it is crucial to validate such models with independent, concrete and informative experimental results, like our fracture surface data set. Secondly, this approach allows comparison between plastic deformation models which predict the location of initiation and

the experimentally determined initiation site location. Such a comparison provides another indirect measure o the reliability of our registration scheme.

6.2 Deformation Simulation in VPFFT Model

The modeling of crystal plasticity has been developing and improving over decades. Current commercially available packages combine crystal plasticity with the finite element method (FEM). Though FEM is widely applicable to general problems, it suffers the problem of high dimensionality in case of samples with complex microstructures, which makes it computationally expensive[100]. A recently developed VPFFT algorithm solves this problem by utilizing a well-optimized and inexpensive fast Fourier transformation (FFT), while preserving the accuracy and resolution of the FEM approach. In this section, we will briefly describe the VPFFT model and computational steps. For more detail information, please refer to [75, 101].

6.2.1 Brief Introduction to VPFFT Model

The VPFFT modeling was pioneered by Lebensohn[101]. This simulation calculates the local viscoplastic anisotropic response on each point on a 3D Fourier grid, where the microstructure information is recorded. The system of differential equations on the local viscoplasticity is solved by the Green's function approach and computed in the Fourier space by using the FFT. The well-optimized and computationally efficient FFT allows fast computation of local information as well as updating texture and microstructure. The numerical performance of VPFFT is better than finite element method of the same problem size.

6.2.2 Simulation settings

In this chapter, the same simulation parameters are used for all the simulations on our fracture surface data set. A volumetric Fourier grid of size $512 \times 512 \times 24$ is used, with the dimension in x and y holding the measured HEDM orientation data from each of the 24 layers. The in-plane data are placed on a square grid as described in Section 4.2.4 of Chapter 4. In the input volume, a two-phase set is supplied due to the VPFFT's requirements. The first phase is the real data of Rene88DT from the aligned data set while the second phase is a buffer phase which fills the empty space left by the real data. A stress is applied in the vertical direction and a total two loading cycles are simulated because we are interested in locating stress hot sports associated with crack initiation in the low-cycle fatigue limit instead of the high-cycle fatigue which induces crack growth and propagation.

6.3 Initiation Site Predictions and Comparison

In this section, we present the two distinctive ways to determine the location of the initiation site for our fracture surface. One is experimental (Section 6.3.1) while the other is based on the prediction of the VPFFT model (Section 6.3.2). These results are followed by a comparison and discussion.

6.3.1 Experimental Determination of Initiation Site

The location of the initiation site determined experimentally serves as an independent evidence for later comparison with initiation site predicted by simulation as well as for the validation of the VPFFT model. In this section, we present a method to experimentally determine the location of the initiation site as follows.

The method is known as the plastic replica method and it was performed by scientists at GE Global Research. The basic idea is to record the crack pattern as the crack develops and pinpoint the initiation site by backtracking recorded crack patterns as a function of time. This method assumes that the critical crack starts on the surface of the sample. Experimentally, this recording step is applied by interrupting the course of cyclic loading. The cyclic loading is usually scheduled to stop after fixed number of cycles, cellulose acetate dissolved in acetone is applied on to the surface of the sample and then a plastic film is cured and recovered. The trace of the crack detains more acetate than the other regions, which clearly records the pattern of the crack. Fig. 6.1 schematically demonstrates this method at four different scheduled cyclic loading stops. In each figure, the fracture (in black) develops with respect to the previous stage in the bulk sample (in pink) and a film of the plastic replica (in green) is extracted with the trace of the crack (in black) recorded. The beauty of this method is that it not only can track the propagation of the crack but also allows us to backtrack the origin of the crack. In this case, the fracture that dominates in the final stage (c.f. Fig. 6.1(d)) is indisputably originated from the initiation site at the initiation stage (c.f. Fig 6.1(a)).

However, the plastic replica method has its own limitations. It can only work for a small sample, because it can only track the fracture on the surface of the sample. Imaging a much larger sample is used for the plastic replica method, and it is quite possible that the initiation site is located at the center region of the sample not necessarily on the side of the sample, thus this method does not provide any useful information until the fracture propagates to the surface of the sample. Thus it is too early to conclude the fracture surface initiates at a point on the surface of the sample. In fact, this method provides information only on the approximate region of the initiation site.

To complement the plastic replica method to pinpoint the location of the initiation site, SEM studies of the fracture surface can be carried out. Fig. 6.2(a) shows the original SEM for the fracture surface. The river-like vein patterns, which are

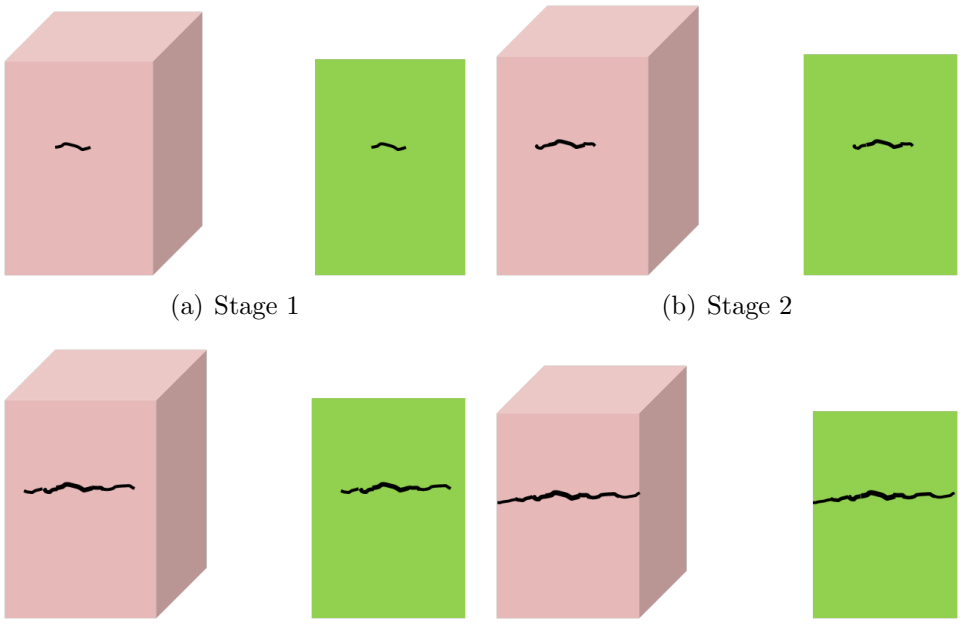

(a) Stage 1 (b) Stage 2

(c) Stage 3 (d) Stage 4

Figure 6.1: Schematic diagram of the plastic replica method to determine the initiation site experimentally. Fig. (a) - (d), the crack pattern (represented in the black line) develops on the side of the bulk material (represented as the pink rectangle cuboid), and a plastic replica is recovered (represented by the green rectangle. The idea is to backtrack the recorded crack traces on the plastic replica.

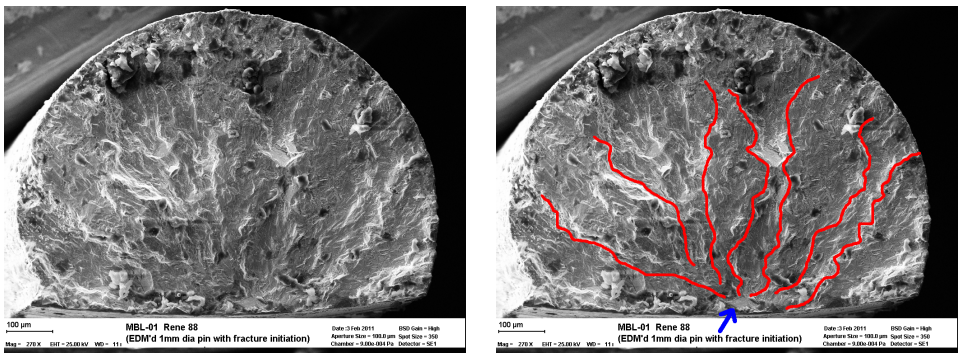

(a) Original SEM (b) River-like Pattern

Figure 6.2: SEM image of the fracture surface: (a) original SEM, (b) SEM image with the river-like patterns marked in red lines and convergence of such pattern to a location (marked by blue arrow), which is probably the initiation site.

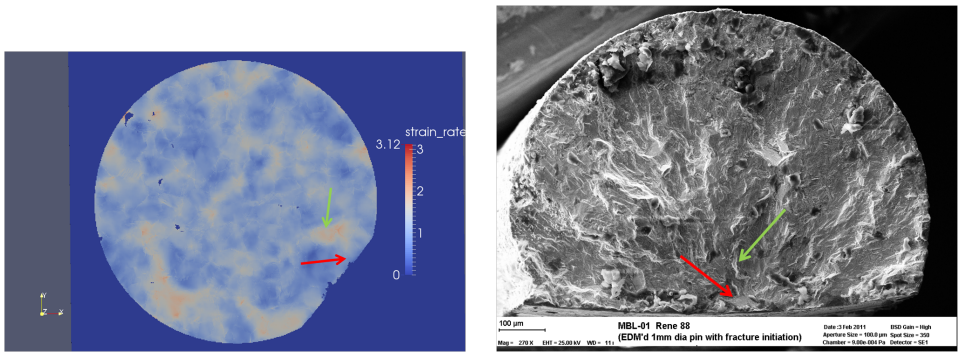

(a) Simulation from VPFFT (b) SEM Image

Figure 6.3: Figures for the simulation of a data set restricted to a cylindrical shape. (a) shows the simulated strain rate field from VPFFT model, where high strain rates are localized in several regions which are generally near the boundary. (b) indicates the particular region with high simulated strain rate on the SEM image shown previously. In both figures, the experimentally determined fracture initiation site is indicated by the red arrow, while the candidate region from the VPFFT simulation is indicated by the green arrow.

delineated in Fig 6.2(b), indicate the traces of the fracture propagation directions locally. Clearly, these river-patterns follow the fan-type flow lines and backtracking these patterns reveals that they converges to a location close to the surface which is probably the initiation site, indicated by the blue arrow in Fig. 6.2(b).

6.3.2 VPFFT Model Predicted Initiation Site and Comparison

As mentioned in 6.1.2, we want to correlate localized high strain/stress locations in the VPFFT model with the experimentally determined initiation site. In this section we simulate the stress and strain rate under the VPFFT model. The virtual sample is trimmed to form a cylindrical subvolume so that the strain calculation is not influenced by corners, notches or overhangs.

Fig. 6.3(a) shows the simulated strain rate for the cylindrical subvolume. The simulation reveals several high strain rate regions most of which are localized. They are candidate locations for the initiation site according to our hypotheses that initiation should occur at a high stress/strain region. Among the "hot spots" seen, one region, indicated by the green arrow, is close to the location of experimentally determined initiation site, which is indicated by the red arrow, in both subfigures of Fig. 6.3. The direct distance between the experimentally and simulation determined initiation sites is roughly $64\mu m$. This discrepancy of $64\mu m$ can be attributed to several possibilities. The first possibility is that it is simply a result of the rough

extrapolation of the "river-like" lines in the SEM image. The second possibility is that VPFFT model makes some simplifying assumptions or neglects some unknown mechanisms so that the candidate initiation site is a little bit off from the experimentally determined position, which is quite understandable due to the difficult nature of the deformation simulation since it depends on many factors. This comparison is motivated to validate the VPFFT model, and from this comparison we would claim that qualitative agreement but not quantitative agreement is achieved. Further modification and fine tuning of the model using this and additional data sets may achieve improved agreement. However, this further step is out of the scope of this thesis.

As a side note, we consider the other high strain rate regions in the VPFFT simulation as shown in Fig. 6.3(a) and explain why they are not considered as the initiation site or at least major initiation site. One reason is that these regions, though shown as high strain rate in the simulation, may be just the artifacts due to the boundary effect because they tend to be located close to the boundary of the trimmed simulation cell. Note for the real sample, more material exists beyond the boundary here, and the boundary is artificially set for the purpose of removing the notches. The other possibility is that they could be initiation sites in reality but ones that never become the dominate one. Observations of so-called *multiple initiation* are made both for Rene88DT[102, 103] and other Nickel-based superalloy[31, 104]. For multiple initiation, it is possible to nucleate multiple initiation sites around the same time under cyclic loading and to develop a small crack for each of them. The important question is which one dominates and emerges over all the other small cracks to form the final fracture surface. Thus the VPFFT model may be correct in the sense that it predicts a multiple initiations site scenario which can happen in real materials.

Chapter 7

Summary and Recommendations for Future Work

7.1 Summary

The key objective of this thesis is to present a new technique to characterize the crystallographic directions normal to the fracture surface. In contrast to the current state-of-the-art SEM-based techniques, this technique is demonstrated to be an improvement in spatial and orientation resolution as well as requiring reduced experimental efforts.

As a part of this work, we have shown that it is possible to reconstruct near-field HEDM data sets of samples in heavily fatigued states and we have developed registration algorithms for merging both independent tomography data sets and coupling this merge with matched HEDM data sets. New automated analysis algorithms have been developed to characterize the fracture surface and the geometry of crystal orientations relative to the surface.

In this thesis, a Rene88DT sample was received from GE Global Research in the form of $1mm$ diameter pieces extracted from the two sides of a fractured sample was measured with high energy x-ray tomography and near-field HEDM. Volumetric data of tomography and HEDM were obtained by reconstruction using inverse Radon transformation and forward modelling simulation, respectively, to obtain spatial resolutions on the order of micrometers. A novel 3D boundary points volumetric registration scheme was developed and performed to align on separate volumes and to merge all reconstructed information into a single volume. Several qualitative and quantitative methods to check the goodness of registration were applied to the registered volume and they indicated good matching of the two samples.

To extract the distribution of the crystallographic normals to the fracture surface, the local normals were estimated based on Principle Component Analysis and this field information was transformed from the sample frame to the crystal frame by the orientation matrix. The distribution of such crystallographic normals was further

studied in plots similar to the inverse pole figure plot. This analysis indicated that the intra-granular fracture (fracture path passing inside the grain) tends to follow the {111} crystal plane, while the inter-granular fracture (fracture path follows a grain boundary) tends to follow {001} grain boundaries. The dominance of the intra-granular fracture at {111} crystal plane could be attributed to the normal slip plane for the face-center-cubic structure, which was {111} due to the close packing of atoms in that plane. However, the tendency of {001} boundary, though the preference was not strong, might be attributed to many possible factors.

In addition to the crystallographic directions normal to the fracture surface, efforts were made to study the fracture initiation mechanism by correlating the experimentally determined location to the simulation determined location of the initiation site. The actual initiation site was estimated experimentally from the SEM images and matched against the river-like vein patterns. A deformation simulation was performed on the aligned volume. A high strain rate region in the simulation was pin-pointed, which qualitatively matched the experimentally determined location of the initiation site. This indicated good agreement of deformation model to reality and this data set might be used to fine tuning existing deformation model in the future.

The completeness of surface characterization here dwarfs that of typical recent work. EBSD studies have been limited to small fractions of the fracture surface area due to geometric and other experimental limitations. The most comparable study is that by Ludwig et al[105] using synchrotron x-ray based Diffraction Contrast Tomography. Even in that work, a smaller number of crystal orientations were measured only in a pristine sample state, rather than in the as-fatigued state studied here.

7.2 Recommendations for Future Work

In spite of all the achievements listed above, some issues exist in this current methodology. We will present here some recommendations for future work by first presenting three known issues and we also present an update on the experimental setup, which can potentially solve all these issues.

7.2.1 Unresolved Issues

Three important issues that should be clarified in future work are i) the ratio of inter- to intra-granular fracture, ii) the determination of the location of the initiation site, and iii) the distribution of crystallographic directions involved in inter-granular fracture. Uncertainties involved in each of these issues in the current data set could be reduced significantly by performing in-situ loading measurements as we will discuss each of these in detail as follows.

Ratio of Inter- to Intra-Granualar Fracture

In Section 5.1.2, we showed that inter-granular fracture dominates the distribution of fracture types. The concern with this statement is that any mis-registration of the data sets will lead to a higher incidence of apparent inter-granular fractures. Our expectation going into this work was that most of the fracture surface would involve intra-granular events. Our analysis indicates $\sim$ 20% intra-granularity. Thus it is natural to question the origination of such dominance of the inter-granularity and whether it is physical or an artifact. We expect to make a minor improvement in the registration by including a relative tilt between the two pieces, but this should produce displacements of less than a grain size, so we do not expect a dramatic change in this characterization. It would be more reliable if we could obtain the orientation information before fracture and it would be much better to track the crack growth as it happens in order to correlate inter-granular fracture with some factor and understand its origination.

Determination of Location of Initiation Site

In Section 6.3.1, the location of the initiation site is experimentally estimated, however, this is a rough estimation. This causes uncertainty when correlate strain hot spots in the simulation with the estimated location. Thus, again, it would be a better test of the VPFFT model if one could detect the initiation site experimentally.

Crystallographic normals for Inter-Granular Fracture

In Section 5.3.2, the distribution of crystallographic normals to the fracture surface with respect to inter- and intra-granular fractures are presented and it was found that the distribution of intra-granular crystallographic planes could be attributed to the $\{111\}$ slip plane in the FCC material. However, the understanding of the inter-granular fractures is lack because it may depend on very local properties as the crack develops. Thus we need a new method to keep track of the time evolution of the whole fracture process.

7.2.2 Combined Near Field and Far Field HEDM to the Rescue

The above three known issues call for a new technique to track important aspects of the whole life of the fracture process. With the ability to map the starting point of the sample to solve the ratio of inter- and intra-granular fracture problem, with the ability to track the initiation process to solve the determination of the location of the initiation site problem and with the ability to track the crack propagation to resolve the crystal orientations for inter-granular fracture problem. Fortunately, all

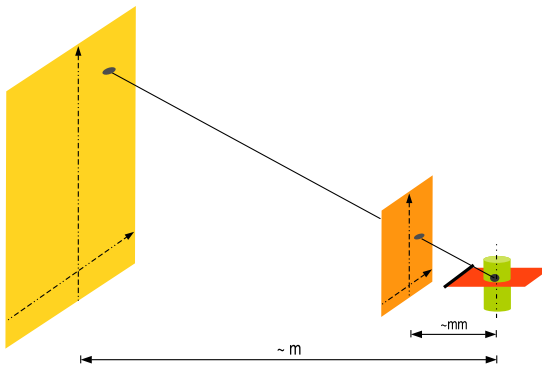

Figure 7.1: Schematic plot of experimental setup for *far field* HEDM measurement. The setup is very similar to near field HEDM (c.f. Figure 2.1), however, the only difference is the extra far field detect which is placed around $10m$ downstream.

these requirements to track the crack process can be achieved by combing near field HEDM with far field HEDM as an in-situ loading apparatus.

The far field HEDM is the variant of the near field HEDM, which can be used to track the crack process. Figure 7.1 shows the schematic diagram for the combination of the far field and near field HEDM. In addition to the near field detector millimeters away from the rotation axis, a far field detector (in yellow) is placed way downstream, which is around meters away. This far field detector is much larger in size than the near field detector to cover comparable field of view and affords large pixel size. Essentially, due to the large distance between the far field detector and the rotation axis, the diffraction patterns reduce to 2θ rings since the location difference of the grains are negligible in the sample region.

With the incorporation of far field HEDM, the crack process can be easily tracked. The deformations induced by cyclic loading introduce the peak shift and peak broadening on the far field detector and this event is easily picked by human eyes or some artificial intelligent algorithm. Then a volumetric measurement of near field HEDM measurement, together with far field HEDM as well as x-ray tomography measurement can be performed. In this sense, the far field HEDM serves as a notification of the critical events in the crack process.

Furthermore, the far field HEDM allows the local strain tensor to be incorporated in the forward modelling simulation, thus be reconstructed as well. Such valuable information is crucial for correlating local strain and stress to the overall fracture process thus enriches our understanding of the fracture mechanism in the micro-scale.

Thus, the updated experimental procedure is to first perform the near field HEDM and x-ray tomography measurements on the un-fractured sample, and then in-situ cyclic loading is performed and monitored by the far field HEDM until some critical event happens, then the near field HEDM and x-ray tomography measurements followed by new round of cyclic loading until new critical event.

Developing the capability to perform these measurements is the subject of a large effort by our group in collaboration with scientists at the Air Force Research Laboratory, Lawrence Livermore National Laboratory, and the APS. A loading device that is consistent both HEDM data collection modes has been built, integrated analysis software is being developed, and early tests have been performed[106]. The work in this thesis is a proof-of-principle that such measurements will be able to track fatigue all the way from pristine initial states through to failure and that such measurements should provide an opportunity for greatly improved understanding through the development of tested computational models.

Appendix A

A New Data Structure for .mic File

A.1 Motivation

The previous implementation for .mic file is based on a tree structure, which is designed for adaptive griding. The drawback for this implementation is that the access time is logarithmic. This problem deteriorates when a great number of points must be sampled, for example when we try to convert a triangular grid to a square grid (c.f. Section 4.2.4). Thus we develop a new data structure to record the triangular grid and we want the access time of orientation query given (x, y) to be constant.

A.2 Implementation

To facilitate constant access time, we must provide some mechanism for random accessing. However, the triangular grid in our problem directly prevents us from random accessing as the square grid does. My way to go around this problem is to introduce a new coordinate system.

The new coordinate system used is essentially a triangular coordinate system, where the i-axis coincides with the original x-axis while the j-axis is 60° up from the x-axis. For the normal hexagonal sample space, we define the center to be center of the new coordinate system, i.e., $i = 0$ and $j = 0$. Then each grid point in this hexagonal system is uniquely determined by a pair of i and j coordinates in terms of integers. Obviously, this conversion between the original x-y coordinates and the new i-j coordinates is unique and computed in constant time.

After the new coordinate system is set up, we need to design a data structure to allow for random accessing. In this problem, we are forced to use an array to support random accessing and the position in this data structure of any (i, j) coordinate must be computable. The ordering in our problem is to scan the all the voxels of the hexagonal sample space layer by layer, from left to right within a layer and from top layer to bottom layer. Then given any coordinate (i, j), its location in the array is

essentially the number of voxels above that point plus the number of voxels to its left in the same layer. Care must be taken to consider whether the triangle is pointing up or down.

A.3 Mathematical Derivation

In this section, we derive the index in the array, given triangle which is specified as (i, j, b) in the hexagonal sample space of generation n where b represents whether the triangle points up ($b = 0$) or down ($b = 1$). Let us first consider the case $j \geq 0$ for simplicity; later we will cover the $j < 0$ case by symmetry.

We first consider the number of grid points in each row (denoted as $f(m)$ for the m-th row). For the m-th row ($m \geq 0$), possible i values in this rows range from -2^n to $2^n - 1 - m$, so there are $2^{n+1} - m$ grid points in total. Thus $f(m) = 2^{n+1} - m$, for $m \geq 0$.

Now consider the number of voxels above the j-th row, which we denote as $g(j)$. By definition, there is no row above 2^n-th row, so $g(j) = 0$ for $j = 2^n$. For $0 \leq j \leq 2^n - 1$, note there are only one row of voxels in 2^n-th row, while all other rows have two rows of voxels pointing up and down, thus

$$g(j) = f(2^n) + 2 \cdot \sum_{k=j+1}^{2^n-1} f(j) = \cdots = 2^n + (3 \cdot 2^n - j)(2^n - 1 - j)$$

One last part is to consider the index of the element within the j-th row (denoted as $h(i, j, b)$). In this case we need to distinguish the triangle's pointing direction. If the triangle is pointing up ($b = 0$), since we know i of this row ranges from -2^n to $2^n - 1 - j$, so the index is $i + 2^n$. If the triangle is pointing down $b = 1$, we need to add extra number of triangles pointing up which is $2^{n+1} - j$. So we have:

$$h(i, j, b) = i + 2^n + b(2^{n+1} - j)$$

Depending whether $b = 0$ or $b = 1$, $h(i, j, b)$ equals $i + 2^n$ or $3 \cdot 2^n + i - j$.

Put everything together, the index of a voxel specified by (i, j, b) is the addition of $g(j)$ and $h(i, j, b)$, which is given by

$$x(i, j, b) = \begin{cases} i + 2^n + b(2^{n+1} - j) & \text{if } j = 2^n \\ 2^n + (3 \cdot 2^n - j)(2^n - 1 - j) + i + 2^n + b(2^{n+1} - j) & \text{if } 0 \leq j \leq 2^n - 1 \end{cases}$$

For $j < 0$, we consider a mirror image of a voxel (i, j, b) about the origin $(0, 0)$, which is now in the upper half ($j > 0$) and we can compute the index using the above equation and then subtract it from the total number of voxels $6 \cdot 4^n$. However, one thing to be careful here is that the mirror image of (i, j, b) is $(-i - 1, -j, !b)$. Even the mirror grid point of (i, j) is $(-i, -j)$, we need to compensate a shift, because the

mirror triangle changes its pointing direction which is reflected in ! sign representing the *logic not* operator for boolean.

Finally, we have the index for any voxel specified by (i, j, b) as follows

$$x(i,j,b) = \begin{cases} i + 2^n + b(2^{n+1} - j) & \text{if } j = 2^n \\ 2^n + (3 \cdot 2^n - j)(2^n - 1 - j) + i + 2^n + b(2^{n+1} - j) & \text{if } 0 \leq j \leq 2^n - 1 \\ 6 \cdot 4^n - x(-i - 1, -j, !b) & \text{if } j < 0 \end{cases} \tag{A.1}$$

Bibliography

[1] Subra Suresh. *Fatigue of materials*. Cambridge university press, 1998.

[2] So Suresh and RO Ritchie. Propagation of short fatigue cracks. *International Materials Reviews*, 29(1):445–475, 1984.

[3] R.A. Flinn and P.K. Trojan. *Engineering Materials And Their Applications*. Houghton Mifflin, 1975.

[4] R.W. Cahn and P. Haasen. *Physical Metallurgy*. North-Holland Physics, 1996.

[5] C Crussard, R Borione, J Plateau, Y Morillon, and F Maratray. A study of impact tests and the mechanism of brittle fracture. *J. Iron Steel Inst*, 183:146–77, 1956.

[6] SP Lynch, BC Muddle, and Timotius Pasang. Mechanisms of brittle intergranular fracture in al-li alloys and comparison with other alloys. *Philosophical Magazine A*, 82(17-18):3361–3373, 2002.

[7] PJE Forsyth and DA Ryder. Some results of the examination of aluminium alloy specimen fracture surfaces. *Metallurgia*, 63(377):117, 1961.

[8] JE Bozek, JD Hochhalter, MG Veilleux, M Liu, G Heber, SD Sintay, AD Rollett, DJ Littlewood, AM Maniatty, H Weiland, et al. A geometric approach to modeling microstructurally small fatigue crack formation: I. probabilistic simulation of constituent particle cracking in aa 7075-t651. *Modelling and Simulation in Materials Science and Engineering*, 16(6):065007, 2008.

[9] Ashley D Spear, Amanda R Priest, Michael G Veilleux, Anthony R Ingraffea, and Jacob D Hochhalter. Surrogate modeling of high-fidelity fracture simulations for real-time residual strength predictions. *AIAA journal*, 49(12):2770–2782, 2011.

[10] CARL A Zapffe and GEORGE A Moore. A micrographic study of the cleavage of hydrogenized ferrite. *Trans. AIME*, 154:335–359, 1943.

[11] SP Lynch. Ductile and brittle crack growth: fractography, mechanisms and criteria. In *Materials forum*, volume 11, pages 268–283. Institute of Metals and Materials Australasia, 1988.

[12] Richard P Gangloff. Hydrogen assisted cracking of high strength alloys. Technical report, DTIC Document, 2003.

[13] R Liu, N Narita, C Altstetter, H Birnbaum, and EN Pugh. Studies of the orientations of fracture surfaces produced in austenitic stainless steels by stress-corrosion cracking and hydrogen embrittlement. *Metallurgical Transactions A*, 11(9):1563–1574, 1980.

[14] Seung Hwan C Park, Yutaka S Sato, and Hiroyuki Kokawa. Effect of micro-texture on fracture location in friction stir weld of mg alloy az61 during tensile test. *Scripta Materialia*, 49(2):161–166, 2003.

[15] RK Nalla, JH Kinney, and RO Ritchie. Effect of orientation on the in vitro fracture toughness of dentin: the role of toughening mechanisms. *Biomaterials*, 24(22):3955–3968, 2003.

[16] AW Bowen. The influence of crystallographic orientation on the fracture toughness of strongly textured ti-6al-4v. *Acta Metallurgica*, 26(9):1423–1433, 1978.

[17] Aỳ W Bowen. The influence of crystallographic orientation on fatigue crack growth in strongly textured ti-6a1-4v. *Acta Metallurgica*, 23(11):1401–1409, 1975.

[18] V Sinha, MJ Mills, J Cv Williams, and JE Spowart. Observations on the faceted initiation site in the dwell-fatigue tested ti-6242 alloy: crystallographic orientation and size effects. *Metallurgical and Materials Transactions A*, 37(5):1507–1518, 2006.

[19] V Sinha, MJ Mills, and JC Williams. Crystallography of fracture facets in a near-alpha titanium alloy. *Metallurgical and Materials Transactions A*, 37(6):2015–2026, 2006.

[20] Kazuo Sato, Tetsuo Yoshioka, Taeko Ando, Mitsuhiro Shikida, and Tatsuo Kawabata. Tensile testing of silicon film having different crystallographic orientations carried out on a silicon chip. *Sensors and Actuators A: Physical*, 70(1):148–152, 1998.

[21] Valerie Randle, Paul Davies, and Owen Williams. Crystallographic analysis of surfaces after brittle fracture in ferritic steels. In *ICF10, Honolulu (USA) 2001*, 2013.

[22] A Boyde and HF Ross. Photogrammetry and the scanning electron microscope. *The Photogrammetric Record*, 8(46):408–408, 1975.

[23] G Piazzesi. Photogrammetry with the scanning electron microscope. *Journal of Physics E: Scientific Instruments*, 6(4):392, 1973.

[24] A Boyde. Quantitative photogrammetric analysis and qualitative stereoscopic analysis of sem images. *Journal of Microscopy*, 98(3):452–471, 1973.

[25] P Mohseni, JK Solberg, M Karlsen, OM Akselsen, and E Østby. Application of combined ebsd and 3d-sem technique on crystallographic facet analysis of steel at low temperature. *Journal of microscopy*, 2013.

[26] PA Davies and V Randle. Combined application of electron backscatter diffraction and stereo-photogrammetry in fractography studies. *Journal of microscopy*, 204(1):29–38, 2001.

[27] David P Field. Recent advances in the application of orientation imaging. *Ultramicroscopy*, 67(1):1–9, 1997.

[28] S Mahalingam and PEJ Flewitt. The influence of grain size on brittle crack propagation. In *Journal of Physics: Conference Series*, volume 371, page 012087. IOP Publishing, 2012.

[29] Roger C Reed, Kenneth A Green, Pierre Caron, Timothy P Gabb, Michael G Fahrmann, Eric S Huron, and Shiela A Woodard. Fatigue crack initiation in nickel-based superalloy rené 88 dt at 593 c.

[30] M Gell and GR Leverant. The characteristics of stage i fatigue fracture in a highstrength nickel alloy. *Acta Metallurgica*, 16(4):553–561, 1968.

[31] K Li, NE Ashbaugh, and AH Rosenberger. Crystallographic initiation of nickel-base superalloy in100 at rt and 538 c under low cycle fatigue conditions. *Superalloys, Champion, Pennsylvania*, pages 251–8, 2004.

[32] JE King. Crystallographic fatigue crack growth in nimonic ap1. *Fatigue & Fracture of Engineering Materials & Structures*, 4(4):311–320, 1981.

[33] K Sadananda and P Shahinian. Analysis of crystallographic high temperature fatigue crack growth in a nickel base alloy. *Metallurgical Transactions A*, 12(2):343–351, 1981.

[34] J Luo and P Bowen. Small and long fatigue crack growth behaviour of a pm ni-based superalloy, udimet 720. *International journal of fatigue*, 26(2):113–124, 2004.

[35] Jiashi Miao. *Very high cycle fatigue behavior of nickel-based superalloy Rene 88 DT*. PhD thesis, The University of Michigan, 2010.

[36] RM Suter, D Hennessy, C Xiao, and U Lienert. Forward modeling method for microstructure reconstruction using x-ray diffraction microscopy: Single-crystal verification. *Review of scientific instruments*, 77(12):123905–123905, 2006.

[37] U Lienert, SF Li, CM Hefferan, J Lind, RM Suter, JV Bernier, NR Barton, MC Brandes, MJ Mills, MP Miller, et al. High-energy diffraction microscopy at the advanced photon source. *JOM*, 63(7):70–77, 2011.

[38] CM Hefferan, SF Li, J Lind, U Lienert, AD Rollett, P Wynblatt, and RM Suter. Statistics of high purity nickel microstructure from high energy x-ray diffraction microscopy. *Computers, Materials, & Continua*, 14(3):209–220, 2010.

[39] CM Hefferan, SF Li, J Lind, and RM Suter. Tests of microstructure reconstruction by forward modeling of high energy x-ray diffraction microscopy data. *Powder Diffraction*, 25(2):132–137, 2010.

[40] Christopher M Hefferan, Jonathan Lind, Shiu Fai Li, Ulrich Lienert, Anthony D Rollett, and Robert M Suter. Observation of recovery and recrystallization in high-purity aluminum measured with forward modeling analysis of high-energy diffraction microscopy. *Acta Materialia*, 60(10):4311–4318, 2012.

[41] SF Li, D Hennessy, C Xiao, U Lienert, and B Tieman. Probing microstructure dynamics with x-ray diffraction microscopy. *Journal of Engineering Materials and Technology*, 130:021007–1, 2008.

[42] SF Li, J Lind, CM Hefferan, R Pokharel, U Lienert, AD Rollett, and RM Suter. Three-dimensional plastic response in polycrystalline copper via near-field high-energy x-ray diffraction microscopy. *Journal of Applied Crystallography*, 45(6):0–0, 2012.

[43] SF Li and RM Suter. Adaptive reconstruction method for three-dimensional orientation imaging. *Journal of Applied Crystallography*, 46(2):512–524, 2013.

[44] Henning Friis Poulsen. *Three-dimensional X-ray diffraction microscopy: mapping polycrystals and their dynamics*, volume 205. Springer, 2004.

[45] HF Poulsen. 3dxrd microscopy–a comparison with neutron diffraction. *Applied Physics A*, 74(1):s1673–s1675, 2002.

[46] HF Poulsen, SF Nielsen, EM Lauridsen, Søren Schmidt, RM Suter, U Lienert, L Margulies, T Lorentzen, and D Juul Jensen. Three-dimensional maps of grain boundaries and the stress state of individual grains in polycrystals and powders. *Journal of applied crystallography*, 34(6):751–756, 2001.

[47] Wolfgang Ludwig, Andrew King, and Greg Johnson. Diffraction contrast tomography-a synchrotron radiation technique for mapping polycrystalline microstructures in 3d. In *Materials Science Forum*, volume 571, pages 207–212. Trans Tech Publ, 2008.

[48] Wolfgang Ludwig, Søren Schmidt, Erik Mejdal Lauridsen, and Henning Friis Poulsen. X-ray diffraction contrast tomography: a novel technique for three-dimensional grain mapping of polycrystals. i. direct beam case. *Journal of Applied Crystallography*, 41(2):302–309, 2008.

[49] Sakurai. *Modern Quantum Mechanics*. Pearson Education, 2006.

[50] R.M. Suter. Elementary scattering for condensed matter physics (unpublished).

[51] Charles Kittel and Paul McEuen. *Introduction to solid state physics*, volume 7. Wiley New York, 1996.

[52] K. Tanaka, S. Kodama, and T. Goto. *X-ray diffraction studies on the deformation and fracture of solids*. Current Japanese materials research. Elsevier Applied Science, 1993.

[53] B.E. Warren. *X-ray diffraction*. Addison-Wesley, 1969.

[54] BE Warren and EP Warekois. Stacking faults in cold worked alpha-brass. *acta metallurgica*, 3(5):473–479, 1955.

[55] RPI Adler and CNJ Wagner. X-ray diffraction study of the effects of solutes on the occurrence of stacking faults in silver-base alloys. *Journal of Applied Physics*, 33(12):3451–3458, 1962.

[56] L Velterop, R Delhez, Th H de Keijser, EJ Mittemeijer, and D Reefman. X-ray diffraction analysis of stacking and twin faults in fcc metals: a revision and allowance for texture and non-uniform fault probabilities. *Journal of applied crystallography*, 33(2):296–306, 2000.

[57] RPI Adler, HM Otte, and CNJ Wagner. Determination of dislocation density and stacking fault probability from x-ray powder pattern peak profiles. *Metallurgical Transactions*, 1(9):2375–2382, 1970.

[58] Yonghua Rong, Gang He, Zhenghong Guo, Shipu Chen, and TY Hsu. X-ray peak-shift determination of deformation fault probability in fe-mn-si alloys. *Cailiao Kexue Yu Jishu(Journal of Materials Science & Technology)(China)(USA)*, 18:459–461, 2002.

[59] T Ungár, S Ott, PG Sanders, A Borbély, and JR Weertman. Dislocations, grain size and planar faults in nanostructured copper determined by high resolution x-ray diffraction and a new procedure of peak profile analysis. *Acta materialia*, 46(10):3693–3699, 1998.

[60] T Ungár, J Gubicza, G Ribárik, and A Borbély. Crystallite size distribution and dislocation structure determined by diffraction profile analysis: principles and practical application to cubic and hexagonal crystals. *Journal of Applied Crystallography*, 34(3):298–310, 2001.

[61] VM Kaganer, R Köhler, MROR Schmidbauer, R Opitz, and B Jenichen. X-ray diffraction peaks due to misfit dislocations in heteroepitaxial structures. *Physical Review B*, 55(3):1793, 1997.

[62] L Löffler and W Mader. Anisotropic x-ray diffraction peak broadening and twinning in diaspore-derived corundum. *Journal of the European Ceramic Society*, 25(5):639–648, 2005.

[63] Fumio Watari, J Van Landuyt, P Delavignette, S Amelinckx, and N Igata. X-ray peak broadening as a result of twin formation in some oxides derived by dehydration. *physica status solidi (a)*, 73(1):215–224, 1982.

[64] T Ungar, H Mughrabi, D Rönnpagel, and M Wilkens. X-ray line-broadening study of the dislocation cell structure in deformed [001]-orientated copper single crystals. *Acta Metallurgica*, 32(3):333–342, 1984.

[65] B Heying, XH Wu, S Keller, Y Li, D Kapolnek, BP Keller, Sp P DenBaars, and JS Speck. Role of threading dislocation structure on the x-ray diffraction peak widths in epitaxial gan films. *Applied physics letters*, 68(5):643–645, 1996.

[66] G Catalan, B Noheda, J McAneney, LJ Sinnamon, and JM Gregg. Strain gradients in epitaxial ferroelectrics. *Physical Review B*, 72(2):020102, 2005.

[67] Yumiko Nakamura, Keisuke Oguro, Itsuki Uehara, and Etsuo Akiba. X-ray diffraction peak broadening and lattice strain in lani¡ sub¿ 5¡/sub¿-based alloys. *Journal of alloys and compounds*, 298(1):138–145, 2000.

[68] Paolo Scardi and Matteo Leoni. Fourier modelling of the anisotropic line broadening of x-ray diffraction profiles due to line and plane lattice defects. *Journal of applied crystallography*, 32(4):671–682, 1999.

[69] S Enzo, G Fagherazzi, A Benedetti, and S Polizzi. A profile-fitting procedure for analysis of broadened x-ray diffraction peaks. i. methodology. *Journal of Applied Crystallography*, 21(5):536–542, 1988.

[70] CE Kril and R Birringer. Estimating grain-size distributions in nanocrystalline materials from x-ray diffraction profile analysis. *Philosophical Magazine A*, 77(3):621–640, 1998.

[71] A Benedetti, G Fagherazzi, S Enzo, and M Battagliarin. A profile-fitting procedure for analysis of broadened x-ray diffraction peaks. ii. application and discussion of the methodology. *Journal of Applied Crystallography*, 21(5):543–549, 1988.

[72] Jeno Gubicza, NH Nam, Levente Balogh, RJ Hellmig, VV Stolyarov, Yuri Estrin, and Tamas Ungár. Microstructure of severely deformed metals determined by x-ray peak profile analysis. *Journal of alloys and compounds*, 378(1):248–252, 2004.

[73] Daniel Hennessy. *Three Dimensional X-Ray Diffraction Microscope Studies of Bulk Materials Microstructure*. PhD thesis, Carnegie Mellon University, 2006.

[74] Christopher M Hefferan. *Measurement of Annealing Phenomena in High Purity Metals with Near-field High Energy X-ray Diffraction Microscopy*. PhD thesis, Carnegie Mellon University, 2012.

[75] Reeju Pokharel. *Spatially resolved in-situ study of plastic deformation in polycrystalline Cu using high-energy X-rays and full-field simulations*. PhD thesis, Carnegie Mellon University, 2013.

[76] Jonathan F. Lind. *In-situ High-Energy Diffraction Microscopy Study of Zirconium Under Uni-axial Tensile Deformation*. PhD thesis, Carnegie Mellon University, 2013.

[77] Shiu Fai Frankie Li. *Imaging of Orientation and Geometry in Microstructures: Development and Applications of High Energy X-ray Diffraction Microscopy*. PhD thesis, Carnegie Mellon University, 2011.

[78] ST Wlodek, M Kelly, and DA Alden. The structure of rene 88dt. *Superalloys*, 1996:129–136, 1996.

[79] Tresa M Pollock and Sammy Tin. Nickel-based superalloys for advanced turbine engines: chemistry, microstructure and properties. *Journal of propulsion and power*, 22(2):361–374, 2006.

[80] José Baruchel, Jean-Yves Buffiere, and Eric Maire. X-ray tomography in material science. 2000.

[81] John H Kinney and Monte C Nichols. X-ray tomographic microscopy (xtm) using synchrotron radiation. *Annual Review of Materials Science*, 22(1):121–152, 1992.

[82] R Becker and S Panchanadeeswaran. Crystal rotations represented as rodrigues vectors. *Textures and Microstructures*, 10:167–194, 1989.

[83] Christopher M Bishop and Nasser M Nasrabadi. *Pattern recognition and machine learning*, volume 1. springer New York, 2006.

[84] Arne Hillerborg, Mats Modéer, and P-E Petersson. Analysis of crack formation and crack growth in concrete by means of fracture mechanics and finite elements. *Cement and concrete research*, 6(6):773–781, 1976.

[85] N Benachour, A Hadjoui, M Benachour, and M Benguediab. Stress ratio and notch effect on fatigue crack initiation and propagation in 2024 al-alloy. *World Academy of Science, Engineering and Technology*, 55:566–569, 2011.

[86] Heinz GF Wilsdorf. Void initiation, growth, and coalescence in ductile fracture of metals. *Journal of Electronic Materials*, 4(5):791–809, 1975.

[87] Jeffrey Koplik and A Needleman. Void growth and coalescence in porous plastic solids. *International Journal of Solids and Structures*, 24(8):835–853, 1988.

[88] SH Goods and LM Brown. Overview no. 1: The nucleation of cavities by plastic deformation. *Acta Metallurgica*, 27(1):1–15, 1979.

[89] JJ Lewandowski, C Liu, and WH Hunt. Effects of matrix microstructure and particle distribution on fracture of an aluminum metal matrix composite. *Materials Science and Engineering: A*, 107:241–255, 1989.

[90] Y Brechet, JD Embury, S Tao, and L Luo. Damage initiation in metal matrix composites. *Acta metallurgica et materialia*, 39(8):1781–1786, 1991.

[91] BR Kirby and CJ Beevers. Cavity formation at grain boundary-subboundary intersections in pure α-iron and an iron 0.14 wt% phosphorus alloy. *Journal of Materials Science*, 12(9):1917–1919, 1977.

[92] D Hull and DE Rimmer. The growth of grain-boundary voids under stress. *Philosophical Magazine*, 4(42):673–687, 1959.

[93] IG Palmer and GC Smith. Oxide dispersion strengthening. *Gordon and Breach, New York*, pages 253–290, 1968.

[94] Y Flom and RJ Arsenault. Effect of particle size on fracture toughness of sic/al composite material. *Acta metallurgica*, 37(9):2413–2423, 1989.

[95] AS Argon, J Im, and R Safoglu. Cavity formation from inclusions in ductile fracture. *Metallurgical Transactions A*, 6(4):825–837, 1975.

[96] Hael Mughrabi, Renhui Wang, Klaus Differt, and Uwe Essmann. Fatigue crack initiation by cyclic slip irreversibilities in high-cycle fatigue. In *Fatigue Mechanisms: Advances in Quantitative Measurement of Physical Damage; a Conference... Dearborn, Mich., 10-11 May 1982*, volume 811, page 1. ASTM International, 1983.

[97] Robert O Ritchie, John Frederick Knott, and JR Rice. On the relationship between critical tensile stress and fracture toughness in mild steel. *Journal of the Mechanics and Physics of Solids*, 21(6):395–410, 1973.

[98] RO Ritchie, WL Server, and RA Wullaert. Critical fracture stress and fracture strain models for the prediction of lower and upper shelf toughness in nuclear pressure vessel steels. *Metallurgical Transactions A*, 10(10):1557–1570, 1979.

[99] DM Norris Jr, JE Reaugh, B Moran, and DF Quinones. Plastic-strain, mean-stress criterion for ductile fracture. Technical report, California Univ., Livermore (USA). Lawrence Livermore Lab., 1977.

[100] Bin Wen and Nicholas Zabaras. An image-based method for modeling the elasto-plastic behavior of polycrystalline microstructures based on the fast fourier transform. Technical report, DTIC Document, 2012.

[101] R A Lebensohn. N-site modeling of a 3d viscoplastic polycrystal using fast fourier transform. *Acta Materialia*, 49(14):2723–2737, 2001.

[102] Anish Kumar, Christopher J Torbet, J Wayne Jones, and Tresa M Pollock. Nonlinear ultrasonics for in situ damage detection during high frequency fatigue. *Journal of Applied Physics*, 106(2):024904–024904, 2009.

[103] Jiashi Miao, Tresa M Pollock, and J Wayne Jones. Microstructural extremes and the transition from fatigue crack initiation to small crack growth in a polycrystalline nickel-base superalloy. *Acta Materialia*, 60(6):2840–2854, 2012.

[104] TP Gabb, J Gayda, and RV Miner. Orientation and temperature dependence of some mechanical properties of the single-crystal nickel-base superalloy rené n4: Part ii. low cycle fatigue behavior. *Metallurgical Transactions A*, 17(3):497–505, 1986.

[105] Wolfgang Ludwig, P Reischig, Andrew King, Michael Herbig, EM Lauridsen, G Johnson, TJ Marrow, and Jean-Yves Buffiere. Three-dimensional grain mapping by x-ray diffraction contrast tomography and the use of friedel pairs in diffraction data analysis. *Review of Scientific Instruments*, 80(3):033905–033905, 2009.

[106] J.C. Schuren, P.A. Shade, J.V. Bernier, S.F. Li, B. Blank, J. Lind, P. Kenesei, U. Lienert, R.M. Suter, T.J. Turner, D.M. Dimiduk, J. Almer, "Bright Light Illuminates Elusive Strains in Creeping Titanium", submitted to Science.